10-MICROMETERS DETECTOR

W. Chiou, et al

AIL

Prepared for:

Office of Naval Research
Advanced Research Projects Agency

February 1973

AD 759077

FINAL REPORT
10-MICROMETERS DETECTOR

ARPA Order No. 1806

Contract No. N00014-70-C-0161
(Modification P00005)

Program Code No. 2E90K21
Investigators: W. Chiou,
M. Aita, and F. Pace
(516) 595-4844

Contractor:
AIL, a division of CUTLER-HAMMER
Deer Park, New York 11729

D D C
RECEIVED
APR 30 1973
D

Scientific Officer:
Director, Physics Programs
Physical Science Division
Office of Naval Research

Effective Date of Contract: 1 December 1969
Contract Expiration Date: 31 December 1972
Amount of Contract: $276,724

Sponsored by Advanced Research
Projects Agency, ARPA Order No. 1806

Date: February 1973

DISTRIBUTION STATEMENT A
Approved for public release;
Distribution Unlimited

144

FINAL REPORT
10-MICROMETERS DETECTOR

ARPA Order No. 1806

Contract No. N00014-70-C-0161
(Modification P00005)

Program Code No. 2E90K21
Investigators: W. Chiou,
M. Aita, and F. Pace
(516) 595-4844

Contractor:
AIL, a division of CUTLER-HAMMER
Deer Park, New York 11729

Scientific Officer:
Director, Physics Programs
Physical Science Division
Office of Naval Research

Effective Date of Contract: 1 December 1969
Contract Expiration Date: 31 December 1972
Amount of Contract: $276,724

Sponsored by Advanced Research
Projects Agency, ARPA Order No. 1806

Date: February 1973

Details of illustrations in
this document may be better
studied on microfiche

DDC
RECEIVED
APR 30 1973

i

TABLE OF CONTENTS

LIST OF ILLUSTRATIONS

I. INTRODUCTION

This document is the final report prepared under Contract N00014-70-C-0161, Modification P00005. The purpose of the program performed under this contract is to continue the research on 10.6-μm image upconversion detectors and to determine the feasibility of developing a 10.6-μm range-gated upconversion imaging laser radar receiver with 150 by 150 resolution elements. To meet the program objectives, the following areas were studied:

- Experimental determination of the effect of a diverging pump on image resolution for the image space configuration upconverter system and comparison of the results with analytical prediction

- Analytical determination of the effect of birefringence and a truncated pump beam on image resolution

- Development of techniques to handle power dissipation inside the nonlinear crystal

- Investigation of techniques for improvement of optical efficiency

An experimental model image upconverter capable of real time direct viewing has been assembled and tested. The optical arrangement of the model was arranged to be operated in either the image space configuration (Type I) or in the Fourier space configuration (Type III). The experimental model can also be operated either CW or pulse gated. Imaging

characteristics such as resolution, field of view, and the upconversion efficiency of the experimental model were measured for different types of operating modes and optical configurations.

Analytical studies of the imaging characteristics of the parametric image upconverter were also carried out in the program. Effects of crystal birefringency and pump beam intensity distribution on the imaging properties were considered. A number of useful relationships for system design was obtained. The experimental results and the analytical results were carefully compared and the excellent agreement obtained made it possible to choose and design the optimum image upconverter system for a particular application.

Some of the material properties of Ag_3AsS_3 such as absorption coefficient at 1.06 μm and the temperature distribution in the crystal under laser beam irradiation were also studied experimentally and analytically.

An objective of this final report is to compile and summarize information which is useful for the understanding and design of a parametric image upconversion system. A descriptive summary of the important characteristics of the parametric image upconverter is presented in the next section for those who are interested in a synopsis of the results of this investigation.

In Section III, system design considerations, design formulas, and procedures for two types of upconverter systems are presented. Quantitative comparisons of the imaging characteristics of different types of optical systems are also contained in this section and should be sufficient for the performance evaluation of the upconverter system.

Conclusions and recommendations for future work are presented in the last section.

II. SUMMARY OF IMPORTANT CHARACTERISTICS OF PARAMETRIC IMAGE UPCONVERTERS

The principal physical process responsible for parametric image upconversion is the second-order nonlinear susceptibility of a single crystal nonlinear material such as proustite. The incoming object waves and the intense pump waves interact with each other in the nonlinear material and generate the sum-frequency image waves. In order to obtain efficient interaction, the object waves and the pump waves must satisfy the phase-match condition in the material. Among several phase-match techniques useful for optical parametric upconversion, the simplest technique suitable for imaging application is birefringent phase-matching in a single crystal bulk material since the spatial information of incoming object waves can easily be preserved with this technique. To obtain birefringent phase-match in a bulk material, the object waves, the pump waves, and the upconverted image waves must be properly polarized and the nonlinear single crystal must be properly oriented with respect to the system optical axis. The phase-match requirement and the birefringent phase-match technique, as will be discussed later, give rise to the imaging characteristics particular to the parametric image upconverter and restricts the parametric image upconverter to certain limited applications.

The phase-match requirement and the crystal dispersion imposes two basic constraints on the upconversion process, namely:

- Usable spectral bandwidth of the object radiation
- Allowable angular separation between the object waves and the pump waves

The spectral acceptance bandwidth of parametric upconverter depends on the material dispersion. It is inversely proportional to the interaction length and is usually narrow unless the material dispersion at IR wavelength and sum-frequency wavelength is identical. Spectral acceptance bandwidth of a 1-cm long proustite pumped by a 1.06-μm beam for upconverting at 10.6 μm is about 6 cm^{-1}. This narrow spectral acceptance bandwidth of the upconverter using proustite virtually eliminates using the proustite image upconverter as a passive thermal image detector in the 8 to 14 μm spectrum. The application of the proustite image upconverter system is presently limited to the detection of objects either radiating sharp spectral lines or illuminated by a laser beam.

Spectral bandwidth may be increased slightly by using a converging or diverging pump beam since different pump angular spectrum will phase-match with a different IR wavelength. A multicolor thermal image upconversion might be possible with this technique of bandwidth widening.

Because of narrow spectral acceptance bandwidth of presently available proustite upconverters, only the image upconversion of monochromatic objects is considered in this report.

The acceptance angle, defined as the maximum incidence angle allowed for IR object waves with respect to the phase-match direction, is inversely proportional to the square root of interaction length. The proportionality constant depends on material refraction indices and three wavelengths involved. For upconversion of 10.6 μm with a 1.06-μm pumped 1-cm long crystal, the acceptance angle was about 9 degrees when noncritically phase-matched. The acceptance angle can be widened slightly by orienting the nonlinear crystal to phase-match at two different angles.

To restrict the angle of incidence of IR object waves at the crystal surface within the acceptance angle limit, input wave to the nonlinear amterial must have an f-number greater than the inverse of the acceptance angle expressed in radians. This means an f-number greater than 6.5 for a 1-cm long proustite.

Two types of basic optical configurations suitable for parametric image upconversion are shown in the next section. In the image space configuration (Type I) system, a distant object (at IR wavelength) is imaged in the nonlinear crystal by the objective telescope. The upconversion process takes place in the real image space. An upconverted

virtual image is relayed to the image recording surface by the relay lens. The upconversion process in the Fourier space configuration (Type III) takes place in the angular-frequency space. A real IR image of the distant object is formed by the objective telescope in the front focal plane of the first Fourier transform lens in front of the nonlinear crystal. The object's spatial Fourier components are upconverted in the nonlinear material and the inverse Fourier is transformed by the second Fourier transform lens. An upconverted real image of the object is then formed in the back focal plane of the second Fourier transform lens. In the Type I system, IR object rays originating from a point interact with a localized portion of the pump beam. In the Type III system, IR object rays from a point interact with the whole pump beam.

The acceptance angle constraint on the object waves introduces limitations on both the field of view (FOV) and the resolving power of the parametric image upconverter system since the constraint affects the spatial frequency response of the image upconverter.

For the Fourier space configuration (Type III) system, the acceptance angle constraint restricts the size of IR image field in the front focal plane of the first Fourier lens and consequently the system FOV. The maximum size of the IR image field formed by the objective telescope is equal to the product of the acceptance angle and the focal length of the first Fourier transform lens. The system FOV is then equal

to a quotient of the IR image field size and the effective focal length of objective telescope. The intensity distribution of upconverted image field of a uniform intensity IR object field is independent of the pump beam intensity distribution but is determined by the phase-match condition and follows a (sin X/X) function where X is a normalized transverse distance from the optical axis.

For the image space configuration (Type I) system, the phase-match constraint introduces thickness aberration and thus limits the image resolution. Linear resolvable upconverted image line width in the crystal due to thickness aberration is proportional to the square root of interaction length. The proportionality constant depends on refractive indices and the wavelengths. For a 1-cm long proustite upconverting a $10.6\text{-}\mu$m object by the $1.06 \ \mu$m pump beam, it is about $100 \ \mu$m. Since the upconversion transverse magnification of Type I system is unity, the linear resolvable line width of an IR object focused on the crystal is equal to the upconverted image resolution width. This means that the Type I system would be diffraction-limited if the f-number of the IR objective telescope is larger than 7.7. When the f-number of the IR objective telescope is matched to the upconversion acceptance angle, that is, the incidence angles of IR object rays are restricted to the acceptance angle limit, the IR angular resolution is independent of the interaction length and is 1.3 times larger than the diffraction resolution of the telescope aperture.

The effects on the imaging characteristics by nonplanar pump waves, introduced either by truncation of the plane wave pump by a finite size crystal aperture or by a nonuniform transverse intensity distribution of the pump beam, are theoretically and experimentally investigated. The finite interaction aperture due to nonplanar pump wave affects differently the imaging properties of two types of upconverter system.

For the Fourier space configuration (Type III) system, the diffraction by the nonplanar interaction aperture limits the system resolving power if other apertures are large compared to the interaction aperture.

The resolving power of a plane wave pumped infinite aperture in a Type I system is unlimited. The IR Rayleigh angular resolution at the nonlinear crystal is limited by the diffraction angle of the interaction aperture. If the interaction aperture is, for example, a uniform amplitude truncated plane wave, the IR resolution angle is identical to the diffraction limit $1.22 \, \lambda_i/a$ where a is the diameter of a uniform pump beam. When the crystal diameter is large compared to the pump beam size and the pump beam intensity distribution is a Gaussian, the IR resolution angle becomes $2\lambda_i/\pi a$ where a is the pump beam diameter ($1/e^2$ diameter). It must be noted that the resolving power of the Type III system is very sensitive to the pump beam characteristics. Use of a pump laser radiating in the lowest transverse mode is, therefore, required for a high resolution Type III system.

The interaction aperture characterized by the intensity distribution and size of the pump beam influences the intensity distribution and size of the upconverted image field of a Type I system. If the object field intensity distribution is uniform, the upconverted image field reproduces exactly the intensity distribution of the pump beam. This can easily be visualized if one realizes that, in a Type I system, the object rays originated from a point interacts with localized pump field. The resolving power of Type I system is independent of the interacting aperture characteristics. This implies that the resolution of the Type I system is insensitive to pump beam angular divergence and a multimode pump beam can be used without degrading the resolving power as long as the angular divergence in the pump beam angular divergence is within the pump acceptance angle limit. Use of a multitransverse mode pump beam does not degrade the resolution of a Type I system. It must, however, be avoided if possible, because hot spots in the multimode pump beam might damage the nonlinear material and voids in the multimode pump beam create blind spots in the image field. The FOV of the Type I system is independent of the interaction length and is equal to the quotient of the effective interaction aperture and the effective focal length of the IR objective telescope.

Conversion efficiency (defined as a ratio of upconverted image radiant power density and IR object radiant power density) of parametric image upconverter, is not a constant over the upconverted image field but

is a function of transverse position. For a Type I system, the conversion efficiency is linearly proportional to the local pump power density. For a Type III system, it is proportional to the peak pump power density and has a $(\sin X/X)^2$ functional dependence over the upconverted image field where X is a normalized transverse position of the image field. The dependence of upconversion efficiency of the image upconverter on the nonlinear susceptibility of the material, the interaction length, the wavelengths, and the material refractive indices is identical to that of single resolution element upconverter. To maximize conversion efficiency for a given material, large pump power density and longer interaction length are required. Unlike the single resolution element upconverter that is judged by the conversion efficiency alone, the figure of merit of the multielements image upconverter should be expressed as a product of peak conversion efficiency and the number of resolution elements. The figure of merit is linearly proportional to the peak pump power and the interaction length but is independent of the interaction aperture area.

For a 1-cm long proustite upconverting 10.6 μm radiation by interacting with a 1.06-μm pump, the normalized peak conversion efficiency is about 5×10^{-7} per W/cm^2 of pump beam density excluding other optical losses. Because of low conversion efficiency per unit pump-power density, together with its low damage threshold, the 10.6-μm proustite image upconverter system will find its useful application in range-gated pulsed-lidar imaging operation. In this particular mode of operation,

the proustite can be irradiated by a peak pump density of $1-MW/cm^2$ without causing material damage. The maximum peak upconversion efficiency of unity is, therefore, theoretically expected from this proustite system. In practice, because of optical loss and other factors yet unexplained, maximum peak efficiency of about 10 percent is practically realizable with $1 \ MW/cm^2$ pump-power density. Peak conversion efficiency (including all optical losses) greater than 10 percent is difficult with the proustite because of the material damage. Techniques for increasing proustite damage threshold, such as antireflection coatings, forced air convection cooling, and immulsion in index matched liquid coolant were found to be ineffective under repetitive pulsed pump laser irradiation.

A slight deviation from the phase-match condition due to material temperature rise was observed under high level CW laser irradiation ($30 \sim 50 \ W/cm^2$). This detuning effect can easily be corrected by initial angular offset. Angular detuning under pulsed laser irradiation was not studied experimentally. Analytical consideration of heat transfer in the material is included in the appendixes.

III. SYSTEM DESIGN CONSIDERATIONS

System design of the parametric image upconverter is considered in this section. Two basic optical configurations are considered and a specific design example of 10.6-μm image upconversion is presented. Design formulas are given without proof in this section since their derivation is given in the appendixes. The basic conditions imposed on the upconverter are:

- Nonlinear material is placed in the near field of a TEM_{00} mode pump beam
- Fine structure patterns in the upconverted image due to the crystal birefringence are negligible
- Noncritical phase-match direction coincides with the system optical axis
- Diffraction due to optical components other than the interaction aperture is neglected

The first condition is introduced since it gives the best resolution for the Type III system.

The second condition is usually satisfied for 10.6-μm upconverters using proustite because the fine structure pattern due to birefringence is masked by other dominant effects such as lens resolution and image recorder resolution.

The third condition is a natural and the most simple choice of the reference axes.

The fourth condition is imposed to isolate the image upconversion characteristics from the properties of other optical components. Inclusion of imaging properties of other optical components can be easily carried out by the standard method. It is therefore not considered in this report.

A.   UPCONVERTED IMAGE FIELD SIZE AND SYSTEM FIELD OF VIEW

The size of the upconverted image field and the system field of view are governed by different factors for the two optical configurations. The phase-match condition, consequently the IR acceptance angle constraint, determines the system FOV of the Type III (Fourier space configuration) system. The interaction aperture, determined by the pump beam size or the nonlinear material cross section, is responsible for limiting the size of the upconverted image field.

For the Type I (image space configuration) system (Figure 3-1), the size of the IR object field on the crystal is equal to the crystal transverse dimension if the pump beam size is considerably larger than the crystal. If the crystal is larger than the pump beam size, the IR object field size is equal to the pump beam size, taking the $1/e^2$ intensity radius as the boundary. The system FOV is obtained by dividing the field size with the

A. IMAGE SPACE CONFIGURATION

$$\frac{1}{S_1} + \frac{1}{S_2} = \frac{1}{f_2}$$
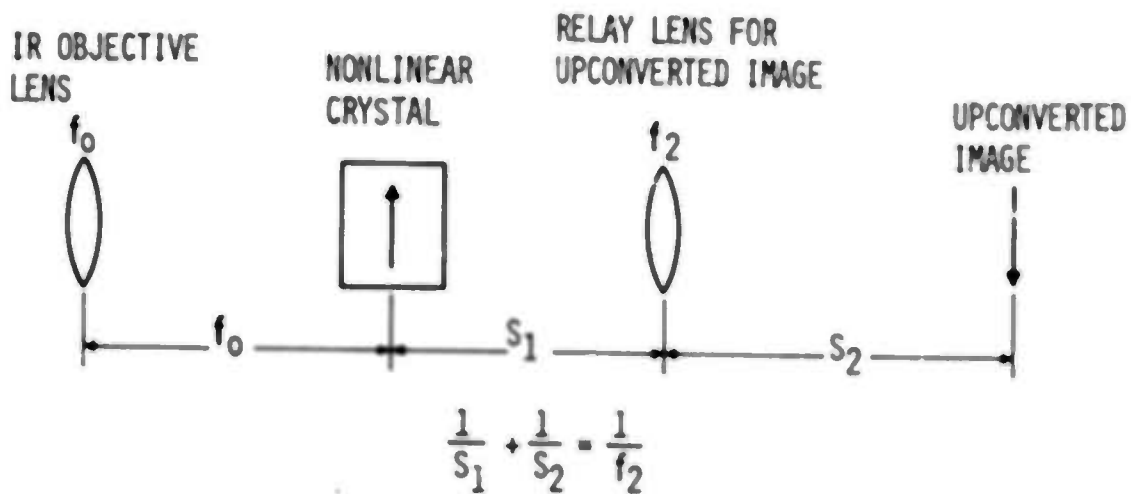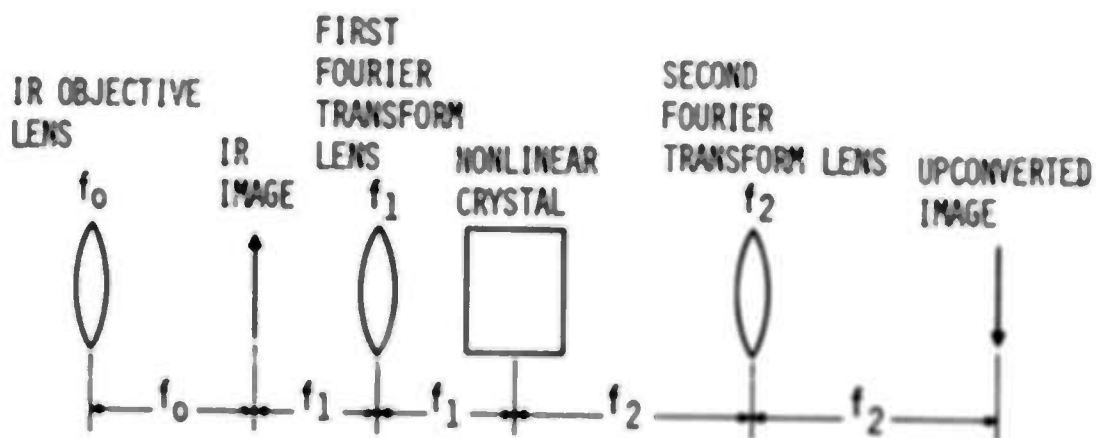
B. FOURIER SPACE CONFIGURATION

FIGURE 3-1. OPTICAL SYSTEMS OF PARAMETRIC IMAGE UP-CONVERTER

effective focal length of the objective telescope. The design formulas are

$$a_{i1} = \begin{cases} b & \text{if } b << w_p \\ \\ w_p & \text{if } b \geq w_p \end{cases} \qquad (3\text{-}1)$$

$$\theta_o = 2a_{i1}/f_o \qquad (3\text{-}2)$$

where

a_{i1} = radius of IR object field on the crystal

b = radius of the nonlinear crystal

w_p = pump beam radius ($1/e^2$ intensity radius)

f_o = effective focal length of the objective telescope

The upconverted image field radius relayed by the relay lens onto the image recording surface is then

$$a_{s1} = |M_s|_1 a_{i1}$$

where M_{s1} is the transverse magnification of the relay lens ($M_s = S_2/S_1$). For Type III (Fourier space configuration) system, the IR object field radius is given by

$$a_{i3} = f_1 \theta_{ia}/2 = f_1 \left(\frac{2\lambda_p \lambda_1 n_1 n_s}{\lambda_s n_p \ell} \right)^{1/2} \qquad (3\text{-}3)$$

where

f_1 = focal length of 1st Fourier transfer lens

θ_a = acceptance angle of the upconverter process

The system FOV is again

$$\theta_o = 2a_{i3}/f_o \tag{3-4}$$

The acceptance angle is determined by the phase-match condition and is given by

$$\theta_{ia} = 2 \left(\frac{2 \lambda_p \lambda_i n_i n_s}{\lambda_s n_p \ell} \right)^{1/2} \tag{3-5}$$

where n's are indices of refraction, λ's are wavelengths, and ℓ is the interaction length. The radius of upconverted image field over the image detecting surface is

$$a_{s3} = f_2 \left(\frac{2 \lambda_p \lambda_s n_i n_s}{\lambda_i n_p \ell} \right)^{1/2} \tag{3-6}$$

Combining equations 3-3 and 3-6 the system transverse magnification becomes

$$|M_t|_3 = \frac{\lambda_s f_2}{\lambda_i f_1} \tag{3-7}$$

B. RESOLUTION

The factor limiting the resolving power of Type I system is thickness aberration introduced by the phase-match constraint. The resolvable IR object line width on the nonlinear crystal is independent of the pump-power distribution and the interaction aperture and is given by

$$r_1 = \left(\frac{n_p \lambda_s \lambda_i \ell}{\pi n_s n_i \lambda_p} \right)^{1/2} \tag{3-8}$$

The system IR angular resolution is then

$$\gamma_1 = r_1 / f_0 = \left(\frac{n_p \lambda_s \lambda_i \ell}{\pi n_s n_i \lambda_p f_0^2} \right)^{1/2} \tag{3-9}$$

For the Type III system, the resolution is limited by diffraction of the interaction aperture. If the TEM_{00} pump beam size is considerably larger than the crystal diameter ($w_p \leq b$), the resolvable IR object line width and the angular resolution are expressed by

$$r_3 = \lambda_i f_1 / \pi w_p \tag{3-10}$$

$$\gamma_3 = \lambda_i f_1 / \pi w_p f_0 \tag{3-11}$$

if the TEM_{oo} pump beam size is considerably larger than the crystal diameter ($b << w_p$) and if pump beam intensity over the crystal is fairly uniform, the IR object resolvable line width and the angular resolution are expressed by

$$r_3 = 0.61 \ \lambda_i f_1/b \tag{3-12}$$

$$\gamma_3 = 0.61 \ \lambda_i f_1/b \ f_o \tag{3-13}$$

The number of resolution elements obtainable for an imaging system is equal to the square of a quotient of the system FOV and the angular resolution.

For the Type I system, it is given by combining equations 3-9 and 3-2.

$$N_I = \frac{4A_{i1} \, n_s \, n_i \, \lambda_p}{n_p \, \lambda_s \, \lambda_i \, \ell} \tag{3-14}$$

where

$$A_{i1} = \begin{cases} A_c = \pi b^2 \ \text{(crystal cross sectional area) if } b << w_p \\ \\ A_p = \pi w_p^2 \ \text{(pump beam area) is } b \geq w_p \end{cases} \tag{3-15}$$

For Type III system it is obtained from equations 3-11, 3-13, and 3-3

$$N_{III} = \frac{8A_{i3}}{n_p \lambda_p} \frac{n_s n_i \lambda_p}{\lambda_i \ell} \tag{3-16}$$

where

$$A_{i3} = \begin{cases} 0.86 \, A_c & \text{if } b < w_p \\ \\ A_p & \text{if } b \geq w_p \end{cases} \tag{3-17}$$

Comparison of equations 3-14 and 3-16 indicates that the resolving power, expressed in the number of obtainable resolution elements of Type III system, is better by a factor of two than that of the Type I system if the identical pump beam is used for upconversion.

C.   CONVERSION EFFICIENCY

Conversion efficiency of the parametric image upconverter requires a different definition from that of the single resolution element upconverter. For the single resolution element upconverter, it is expressed by the ratio of total upconverted power to total IR input power. The image upconverter contains many resolution elements and a nonuniform intensity distribution within the upconverted image field. Conversion efficiency of the image upconverter must, therefore, be defined for a pair of single resolution conjugate elements. Since the intensity distribution (envelope) of the upconverted image field takes a certain known functional form, only the conversion efficiency at the center of the upconverted image field is required to be considered.

There are two possible ways of defining the conversion efficiency. The first definition is to express it as a ratio of upconverted power to IR input power contained in a pair of on-axis conjugate resolution elements. This definition is analogous to that of the single resolution element upconverter. The second definition is to express it as a ratio of peak power density of a resolvable on-axis upconverted image to peak power density of the conjugate on-axis IR object. The latter definition is adopted in this report since it is better suited to the imaging application.

The on-axis conversion efficiency of two basic optical configurations is identical and is given by:

$$\eta = \frac{W_s}{W_{ir}} = \frac{512 \, \pi^5 \, t \, d_{eff}^2 \, \ell^2}{10^{-7} \, C \, n_i \, n_s \, n_p \, \lambda_s^2} \, \frac{P_p}{A_p} \qquad (3\text{-}18)$$
$$(b \geq w_p)$$

where

W_s = peak power density in W/cm^2 of on-axis upconverted image of the conjugate IR object spot of minimum resolvable size

W_{ir} = peak power density, in W/cm^2 of on-axis IR object

$t = (=t_i^2 t_s^2 t_p^2)$ resultant optical surface transmission of the nonlinear material

d_{eff} = effective SHG coefficient along the phase-match direction in cgs unit

ℓ = interaction length in cm

P_p = pump beam power in watts

$n_{\ell} = (\ell = i,\ p,\ s)$ index of refraction along the phase-match direction of nonlinear material at wavelength denoted by the subscript

λ_s = sum-frequency wavelength in cm

A_p = pump beam cross-sectional area in cm^2

C = speed of light in cm/s

Equation 3-18 is valid for the case where the crystal diameter is larger or at least equal to the pump beam diameter. When the pump beam is considerably larger than the crystal diameter, the conversion efficiency is expressed in the same functional form as that of equation 3-14 but with a different proportionality constant. A practical upconverter system will satisfy the condition $w_p \leq b$, since this condition is required for efficient use of the available pump power and for better resolution. It must be noted that equation 3-14 is identical to the conversion efficiency expression of the phase-matched parametric upconversion of three plane waves. This is no surprise if one realizes that the condition along the optical axis of the image upconverter is almost the same as that of the phase-matched plane-wave interaction.

The on-axis photon conversion efficiency is, from equation 3-14, expressed by

$$\eta_p = \eta \lambda_s/\lambda_i = \frac{512\ \pi^5\ t\ d_{eff}^2\ \ell^2\ P_p}{10^{-7}\ C\ n_i\ n_p\ n_s\ \lambda_s\ \lambda_i\ A_p} \tag{3-19}$$

The relative intensity distribution of upconverted image field with a uniform IR object field emittance is considered next.

For the Type I system, the upconverted image field envelope is the same as that of pump beam intensity distribution if the crystal is larger or at least equal to the pump beam size. The size of the upconverted beam is identical to the pump beam size. This relation between the pump beam and the upconverted image field intensity envelope holds for non TEM_{00} mode pump beam. Hot spots and voids in a multimode pump beam will, therefore, be reproduced in the upconverted image field and appear as blemishes.

The upconverter image field intensity envelope of Type III system is, contrary to Type I system, independent of the pump beam intensity distribution. It is determined by the phase-match condition and is expressed by

$$\frac{W_s(\rho_s)}{W_s(\rho_s = 0)} = \text{sinc}^2\left(\frac{\pi \, \ell \, n_p \, \lambda_i \, \rho_s^2}{2 \, n_s \, n_i \, \lambda_p \, \lambda_s \, f_2^2} \right) \tag{3-20}$$

where

ρ_s = radial distance in the upconverted image field from the optical axis

$W_s(\rho_s)$ = power density of upconverted image field at ρ_s

f_2 = focal length of second Fourier transform lens (Figure 3-1B)

Equation 3-6, which describes the size of the upconverted image field, is obtained from equation 3-20 by taking the first root of the sinc function as the limiting size and solving for the radial distance ρ_s.

The conversion efficiency achievable with proustite is about a factor of less than the theoretical calculation expressed by equation 3-14. Reasons for the discrepancies between experimental measurements and analytical predictions are not known with certainty. Possible reasons are crystal absorption and scattering. Some discussion on absorption and scattering in proustite is presented in Appendix D.

D.   SYSTEM SIGNAL-TO-NOISE RATIO

To achieve any advantage from upconversion, detection or recording of the upconverted image with a reasonable quantum efficiency in a signal-shot-noise limited mode is desirable. Presently available image detectors suitable for the image upconverter application are either S-20 or S-1 photocathode image intensifiers. An S-20 photocathode is better than an S-1 response cathode, but its use requires a Ruby laser pump. To achieve a signal-shot-noise limited operation, the image intensifier tube must be either gated or cooled or both to reduce dark noise.

The narrow spectral acceptance of the upconverter is an advantage when the upconverter system is used as a laser receiver, since it lessens the background noise. Parametric upconversion does not (to a first order approximation) generate internal noise. Noise at the sum-frequency originates from the background thermal radiation within the IR acceptance spectral bandwidth.

Other sources of noise, which must be added to the background noise are the pump leakage noise due to imperfect pump suppression and the image detector dark current noise.

The signal-to-noise ratio, which depends on the radial distance from the optic axis, of the image upconverter system using an image intensifier tube for direct viewing is then expressed by:

$$
(SNR)_\rho = \left[\frac{\eta_d\, \eta(\rho)\, \tau f}{h\, \nu_s} \right]^{1/2} \frac{\alpha_i W_i t_{so} t_{io} \tau_i}{\left\{ (\alpha_i W_i t_{io} \tau_i + w_b \tau_g) t_{so} + \tau_g \left(W_p(\rho) t_{po} + W_t \right) / \eta(\rho) \right\}^{1/2}}
$$

(3-21)

where

η_d = quantum efficiency of the image intensifier photocathode

$\eta(\rho)$ = conversion efficiency given by equation 3-14 multiplied by a radial distance dependent function

W_i = on-axis radiant emittance of IR object

t_{so} = transmittance at λ_s of output optical components

t_{io} = transmittance at λ_i of input optical components

W_b = thermal background radiant emittance at the input surface of the nonlinear material

α_i = collection efficiency of IR telescope

$W_p(\rho)$ = pump beam power density (depends on radial distance)

t_{po} = transmittance at λ_p of output optical components

W_t = noise equivalent irradiance of the photocathode of image intensifier tube

τ = observation time (integration time)

f = pulse repetition rate

τ_i = pulse width of active IR illuminator

τ_g = width of receiver gate

It is assumed in equation 3-21 that the width of the receiver gate is equal to the pump-pulse width and the pump-pulse width is longer than the IR illuminator pulse width. If the pump pulse is shorter than the IR pulse width, τ_i in equation 3-21 should be replaced by τ_g. For a system operating in CW mode, the conditions $\tau_i = \tau_g$ and $f\tau_g = 1$ hold.

To illustrate the relative magnitude of noises, a proustite upconverter pumped by a TEM_{oo} mode Nd:YAG laser beam is considered below. It was assumed that the image detector is a cooled S-1 photocathode image intensifier tube. Noise equivalent input energy W_t of typical

cooled S-1 tube is approximately 10^{-11} W/cm^2 at 0.967 μm. The thermal background emittance w_b of the upconverter system is generated within the nonlinear crystal if it is not cooled. If the input IR optical components and the crystal were cooled, the thermal background would originate in the background scene.

$$W_b = \begin{cases} \dfrac{\pi C^2 h\, \Delta\nu_i\, \epsilon_c}{\lambda^5\, (e^{h\nu_i/kT_c}-1)} & \text{for room temperature nonlinear crystal (a)} \\[4mm] \alpha t_{io}\, \dfrac{\pi C^2 h\, \Delta\nu_i}{(e^{h\nu_i/kT_b}-1)} & \text{for cooled IR optics and crystal (b)} \end{cases} \qquad (3-22)$$

where

T_c = crystal temperature

T_b = background temperature

ϵ_c = crystal emissivity (≈ 0.05 for proustite at 10 μm)

For a room temperature proustite with $\Delta\nu_i/C = 0.05$ cm^{-1}, $w_b \approx 4 \times 10^{-6}$ W/cm^2. For $t_{so} = 0.25$, the quantity representing background noise $w_b t_{so}$ is about 10^{-6} W/cm^2.

The quantity representing pump leakage noise in equation 3-21 becomes independent of absolute pump power density, since

$$t_{op} W_p(\rho)/\eta_{(\rho)} = 2W_{po} t_{op}\, e^{-2\rho^2/w_p^2} \Big/ K W_{po}\, g(\rho) = 2t_{op} e^{-2\rho^2/w_p^2} \Big/ K g(\rho)$$

where

$$g(\rho) = e^{-2\rho^2/w_p^2} \quad \text{for Type I}$$

$$g(\rho) = \text{sinc}^2\left(\frac{\pi \ell n_p \lambda_i \rho^2}{2 n_s n_i \lambda_p \lambda_s f_2^2}\right) \quad \text{for Type III}$$

Furthermore $g(\rho)$ for Type III system can be expressed approximately by $e^{-\rho^2/w_p^2}$ by proper choice of f_2 since a sinc function can be approximated by Gaussian function up to the first zero of a sinc function. If this is done, pump leakage noise contribution will be independent of the radial distance and becomes

$$W_p(\rho) t_{op}/\eta(\rho) = 2 t_{op}/K \tag{3-23}$$

where K is expressed, from equation 3-14

$$K = \frac{512 \, \pi^5 \, t_c \, d_{eff}^2 \, \ell^2}{10^{-7} C \, n_i n_s n_p \lambda_s^2} \quad (\approx 5 \times 10^{-7} \text{ for a 1-cm proustite})$$

The quantity representing photocathode dark noise is

$$W_t/\eta(\rho) = 2W_t/W_{po} \, K \, e^{-2\rho^2/w_p^2} \tag{3-24}$$

The conditions that the background noise will dominate the pump leakage noise and the tube dark noise are then

$$t_{op} < t_{so} W_b K/2 \ (= 2.5 \times 10^{-13} \text{ for 1-cm proustite and } t_{so} = 0.25)$$

and   (3-25)

$$W_{po} \, e^{-2\rho^2/w_p^2} > 2 W_t/K t_{so} W_b \ (= 40 \text{ W/cm}^2 \text{ for proustite and} \\ \text{cooled S-1 cathode} \\ \text{with } t_s = 0.25)$$

The above results indicate that, for the system considered, a minimum of 126-dB pump rejection and a minimum of 40 W/cm^2 pump-power density at $1/e^2$ radius are required for background or signal-shot-noise limited operation. When t_{op} = 125 dB and W_p = 40 W/cm^2, the background noise, pump leakage noise, and the tube dark noise are approximately equal.

The above condition for the pump suppression can be satisfied by use of two interference filters and a polarization filter. The transmission at λ_s through these filters would, however, not exceed 0.3 in practice. The choice of t_{so} = 0.25 is, therefore, appropriate for the system design.

Insufficient pump suppression in front of the image intensifier affects the system performance differently for two different types of optical configuration. For the Type I system, the pump beam is expanded by the image relay lens and appears larger than the original size in the image plane. Since the power density of an expanded pump beam is less than the original pump beam, required pump suppression for this system is less than above calculation. The leaked pump wave increases background noise over entire image field for Type I system. The pump beam is focused on a point in the image plane by the second Fourier transform lens for the Type III system. Insufficient pump suppression would, therefore, create a blind spot in the image field where the leaked pump beam is focused. Required pump suppression for this system is more stringent than Type I system if one wishes to eliminate a blind spot within the FOV.

Since the background noise dominant conditions can be satisfied for a pulse-gated upconverter system, the image upconverter is either background noise limited or signal-shot-noise limited. For this case the on-axis signal-to-noise ratio becomes

$$(SNR)_o \left(\frac{1}{R_{po} f \tau} \right)^{1/2} = \left(\frac{\eta_d \, K t_{so}}{h \nu_s \, 2} \right)^{1/2} \frac{\alpha_i \, W_i \, t_{io}}{(\alpha_i \, t_{io} \, W_i + W_b)^{1/2}} \tag{3-26}$$

where $R_{po} (= W_{po} \tau_g)$ is the on-axis pump energy density per pulse in joule/cm^2.

It is assumed in equation 3-26 that the illuminator pulse width is equal or longer than the pump-pulse width.

E. A SYSTEM DESIGN EXAMPLE FOR 10.6-μm IMAGE UPCONVERTER USING PROUSTITE

A design of a pulse-gated active image upconverter using a Nd:YAG laser pumped proustite is considered. The following assumptions are made:

- A cooled S-1 image intensifier tube is used for image viewing

- Pump leakage and image tube dark noise are small compared to the thermal background noise

- Proustite can be safely irradiated with peak power density of 0.5 MW/cm^2 with repetitively pulsed pump beam

- Image degradation by the optical components is negligible

- All lenses are AR coated so that reflection losses from lenses are negligibly small

- Phase-match change due to crystal temperature rise is corrected if there is any

- Pump beam is in TEM$_{oo}$ mode

- Gate open duration is equal to or shorter than the illuminator pulse width ($\tau_i = \tau_g$)

- The crystal diameter is larger or at least equal to the pump beam diameter

- Proustite is at room temperature

Parameter values used in the following design calculation are listed as follows:

$$n_p = 2.817$$

$$n_i = 2.68$$

$$n_s = 2.804$$

$$\lambda_s = 0.967 \; \mu m$$

$$\lambda_p = 1.064 \; \mu m$$

$$\lambda_i = 10.6 \; \mu m$$

$$d_{eff} = 64 \times 10^{-9} \; esu$$

$$t_c = 0.475$$

$$t_{io} = 1$$

$$t_{so} = 0.25$$

$$W_b = 4 \times 10^{-6} \; W/cm^2$$

$$a = \frac{1}{4F_o^2} = \frac{1}{4 \times 7^2} = \frac{1}{4 \times 49} = \frac{1}{196} = 5.1 \times 10^{-3}$$

$$W_b = 4 \times 10^{-6} \; W/cm^2$$

$$\eta_d = 3 \times 10^{-3}$$

$$W_t = 10^{-11} \; W/cm^2 \; at \; 0.967 \; \mu m$$

$$K = 5 \times 10^{-7}$$

The required pump beam size and peak pump power are calculated first from equations 3-14, 3-20, and assumed peak pump on-axis power density of 0.5 MW/cm^2.

Using parameter values given previously, one obtains

$$w_{pI} = 5.53 \times 10^{-3} (N\ell)^{1/2}$$

$$w_{pIII} = 3.91 \times 10^{-3} (N\ell)^{1/2}$$

where subscripts I and III denote Type I and Type III systems, respectively. For $N = 150 \times 150$ and $\ell = 1$ cm

$$w_{pI} = 0.829 \text{ cm}$$

and

$$w_{pIII} = 0.587 \text{ cm}$$

The peak pump power required to give 0.5 MW/cm^2 on-axis peak power density is then 0.54 MW for the Type I system and 0.27 MW for the Type III system.

The theoretical on-axis peak conversion efficiency is, from equation 3-14, equal to 0.125 for 0.5 MW/cm^2 on-axis pump power density. Practically achievable conversion efficiency is about one-half of the theoretical estimate, therefore, practical on-axis conversion efficiency with 0.5 MW/cm^2 pump density is about 6 percent.

Figure 3-2 is a plot of equation 3-26 for a pulse-gated 10.6-μm proustite system with parameter values given. For direct viewing, the integration time τ is approximately equal to 0.2 s, the integration time of human eyes. To avoid flicker, the pulse repetition rate should be at least 16 PPS. Pump pulse-width of 1/2 microsecond to 1 microsecond should be used for range-gated operation since the range gate of 75 to 150 m is desirable for practical radar application. The quantity $R_p f \tau$ for the system considered ranges from 0.8 to 1.6. The on-axis minimum discernible object power density is about 10^{-5} W/cm^2 for unity contrast objects.

The off-axis minimum discernible object power density is obtained by multiplying the on-axis value by a factor equal to inverse of amplitude distribution function of the upconverted image field. For a Type I system, the image field amplitude follows a Gaussian distribution and therefore the minimum discernible object power density at the edge of the image field is e^2 times of on-axis value, that is, 6.4×10^{-5} W/cm^2. For a Type III system, the amplitude distribution of image field is expressed by a (sin X/X) function. Minimum discernible object power density at the transverse position corresponding to the root of sin X/X function becomes, of course, infinity.
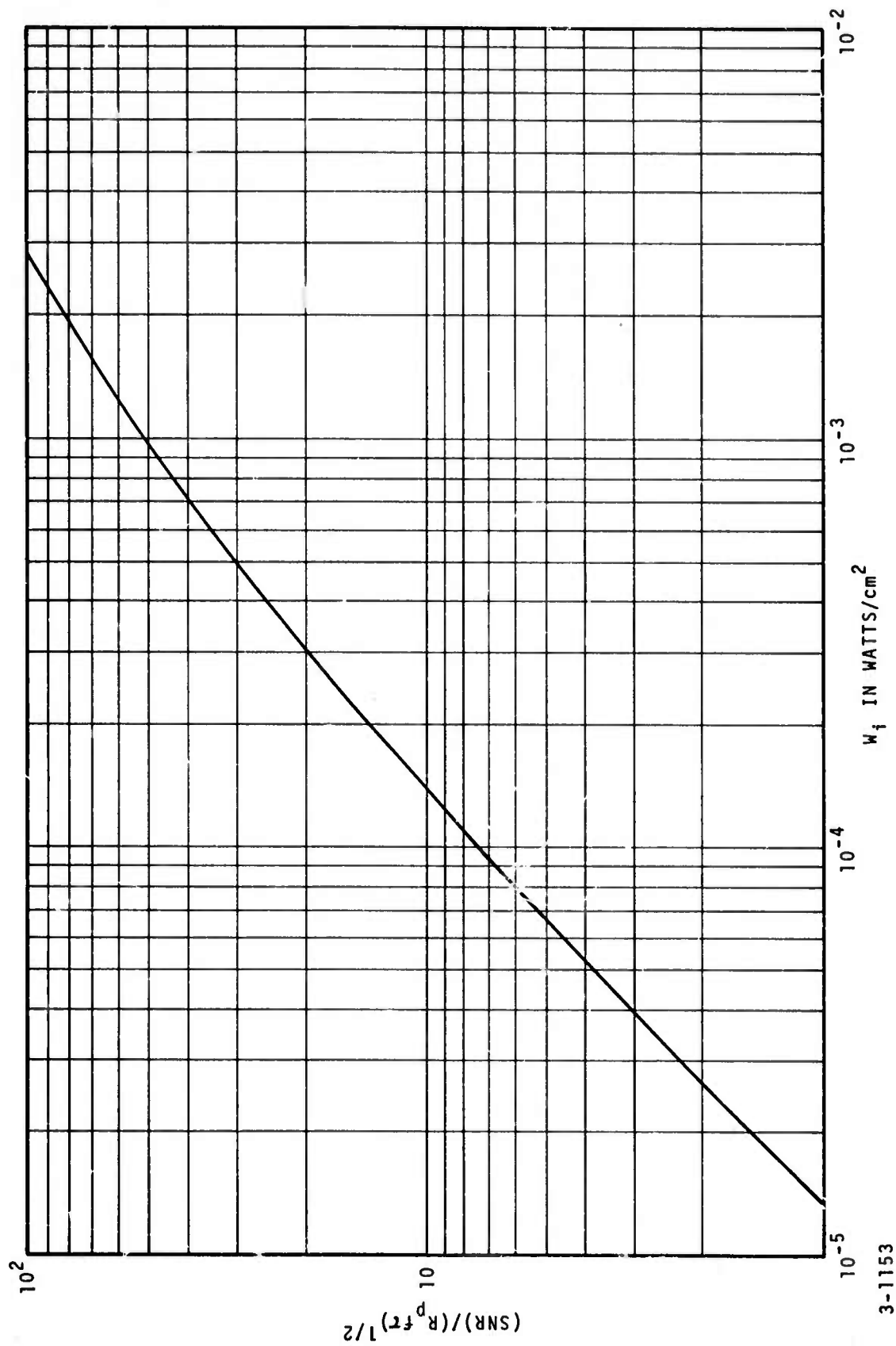
FIGURE 3-2. PLOT FOR A PULSE-GATED 10.6-μM PROUSTITE SYSTEM

3-1153

3-23

The power density scattered back from a laser illuminated target is

$$W_i = \frac{P_t \, r_t}{\frac{\pi}{4} \, \theta_t^2 \, R^2} \qquad (3\text{-}27)$$

where

P_t = laser illuminator peak power

r_t = target reflectivity

θ_t = illuminating beam divergence

R = range

Ideally the illuminator beam divergence is matched to the receiver field of view. The required illuminator power per unit range can be calculated from equations 3-26 and 3-27 for a given signal-to-noise ratio. For $\theta_t = 0.1$ rad, $r_t = 0.1$, and $W_i = 2.72 \times 10^{-5}$. W/cm^2, the minimum illuminator peak power per 1 km range is 2.1×10^4 W/km^2. The illuminator energy per pulse required for a 5-km range is then 0.5 J, which can be generated by a reasonable CO_2 laser.

Performance characteristics and optical parameters of the receiver system considered are summarized in Table 3-1.

TABLE 3-1. CHARACTERISTICS OF PROUSTITE 10.6-μM RANGE-GATED RADAR IMAGE UPCONVERTER SYSTEM

Optical System	I	III
Nonlinear material	1-cm long proustite	1-cm long proustite
FOV	5 degrees to $1/e^2$	5 degrees null to null
Number of resolution elements	150×150	150×150
Frame rate	16 ft/s	16 ft/s
Image detector	Cooled S-1 intensifier	Cooled S-1 intensifier
Object wavelength	10.6 μm	10.6 μm
Upconverted wavelength	0.967 μm	0.967 μm
Pump wavelength	1.06 μm	1.06 μm
On-axis pump power density	0.5 MW/cm^2	0.5 MW/cm^2
On-axis conversion efficiency	0.125	0.125
Required minimum pump beam diameter	1.7 cm	1.2 cm
Peak pump power	0.54 MW	0.27 MW
Gate width	1 μs	1 μs
Pump energy per pulse	0.54 J	0.27 J
On-axis minimum discernible object power density	10^{-5} W/cm^2	10^{-5} W/cm^2
Objective lens effective F-number	7	7
System optical efficiency at sum frequency	0.25	0.25
Range	5 km	5 km
CO_2 illuminator laser energy per pulse	0.5 J	0.5 J
Target reflectance	0.1	0.1

IV. CONCLUSIONS AND RECOMMENDATIONS

Experimental and analytical studies carried out in this program have demonstrated that the proustite image upconverter pumped by a 1.06 μm pump beam is capable of reproducing an image of 10.6 μm illuminated objects with resolution exceeding 150×150 elements. It has also demonstrated that a range-gated radar image upconversion with a reasonable range can be constructed with presently available components.

The imaging characteristics and parameters restricting resolution and efficiency are identified. A set of design formulas useful for the system design is obtained. The appropriate applications of image upconverter techniques at present are:

- Range-gated radar image system
- IR holography
- Laser diagnostic technique
- Laser weapon aim-point monitoring

In order to advance the state of the art of image upconversion technique development, the following technical areas are recommended:

- Development of new nonlinear material with improved characteristics

- Development of high quantum efficiency low noise image tube with a narrow spectral response at λ_s

- Development of a high efficiency band-pass filter with sufficiently large out-of-band rejection

- Improvement of pump laser characteristics and laser construction.

APPENDIX A

REAL TIME IMAGE UPCONVERSION EXPERIMENTS WITH THE DIRECT VIEWING LABORATORY MODEL

An experimental model upconverter capable of real time direct viewing of upconverted images has been set up during this period.

The imaging characteristics of the upconverter were measured first with the proustite crystal pumped by a CW TEM_{oo} mode beam. The resolving power of this model arranged in the Fourier space configuration was measured to assess how close it came to achieving diffraction limited operation. The model was then set up in the image space configuration to measure the extent of thickness aberration.

The measured angular resolution of approximately 1 milliradian for the Fourier space configuration was within a factor of two of the Rayleigh resolution of a uniformly illuminated object lens aperture. The number of resolution elements contained in a 10-degree field of view, which is also experimentally checked, is consequently better than the resolution objective for the program of 150 by 150 elements. Upconverted images of a 10.6-μm illuminated USAF 1951 resolution chart containing groups smaller than 1 lp/mm were obtained. Because the resolution chart does not fill the field of view, the actual number of resolvable elements contained in the recorded images which fills a 7.5-degree angle is 114 by 114.

The resolving power of the model arranged in the image space configuration was also measured. The experimental results prove (as expected) that the resolvable image linewidth is limited by the thickness aberration. The measured image resolution linewidth of 60 μm agrees with the physical optics prediction of 68 μm, but is approximately three to four times narrower than the geometric optics calculation. The main reason for failure of the geometric optics theory to accurately predict the extent of aberration is probably due to the inability of the geometric optics to account for the intensity variation of the upconverted image rays. Upconverted images of the resolution chart with 62 by 62 resolution elements were obtained with the experimental model in the image space configuration. Measured angular resolution is slightly worse than the diffraction limited angular resolution of the object lens.

The effect of diverging pump beam on the resolving power of the upconverter system in the image space configuration was investigated. The fact that resolution of the image space configuration system using a multi-mode pump beam does not degrade from that of a TEM_{oo} mode pumped system was verified experimentally. However, a nonuniform intensity corresponding to the multimode pattern is superimposed on the upconverted image.

Image upconversion experiments with the image space configured model, using pulsed pump beam and a gated image tube, were also carried out. Some preliminary results of the experiments are also presented.

1. EXPERIMENTAL ARRANGEMENT

The experimental model upconverter system is shown schematically in Figure A-1. The system was arranged so that the optical configuration and the pump beam parameters could be readily changed with minimum physical alteration of the setup. A 2.5-cm diameter, and 0.6 cm thick proustite crystal was used. The upconverter was aligned for Type II noncritical phase matching. The proustite was oriented such that its crystallographic X axis lies in the plane of paper and is parallel to the front surface. Its optic axis lies in a plane perpendicular to the paper and makes an angle of 20 degrees with the normal (along the C axis) to the polished front and back surfaces. A continuously pumped Nd:YAG laser radiating electric fields, polarized parallel to the plane of paper, was used as a pump source. The laser is fitted with an acousto-optic Q-switch allowing pulsed as well as CW operation. The beam parameters of the 1.06-μm pump beam emanating out of the beam expander are shown in Table A-1 for various modes of operation.

TABLE A-1. 1.06 μm PUMP BEAM PARAMETERS AFTER BEAM EXPANSION

MODE	AVERAGE POWER	BEAM CROSS SECTION	BEAM DIAMETER	BEAM DIVERGENCE
CW TEM$_{00}$	5.0 watts	Gaussian	1.1 cm	0.16 mrad
CW Multi-mode	7.5 watts		1.1 cm	1.0 mrad
Q-Switched TEM$_{00}$ 1000 PPS	0.5 watt	Gaussian	1.1 cm	0.16 mrad
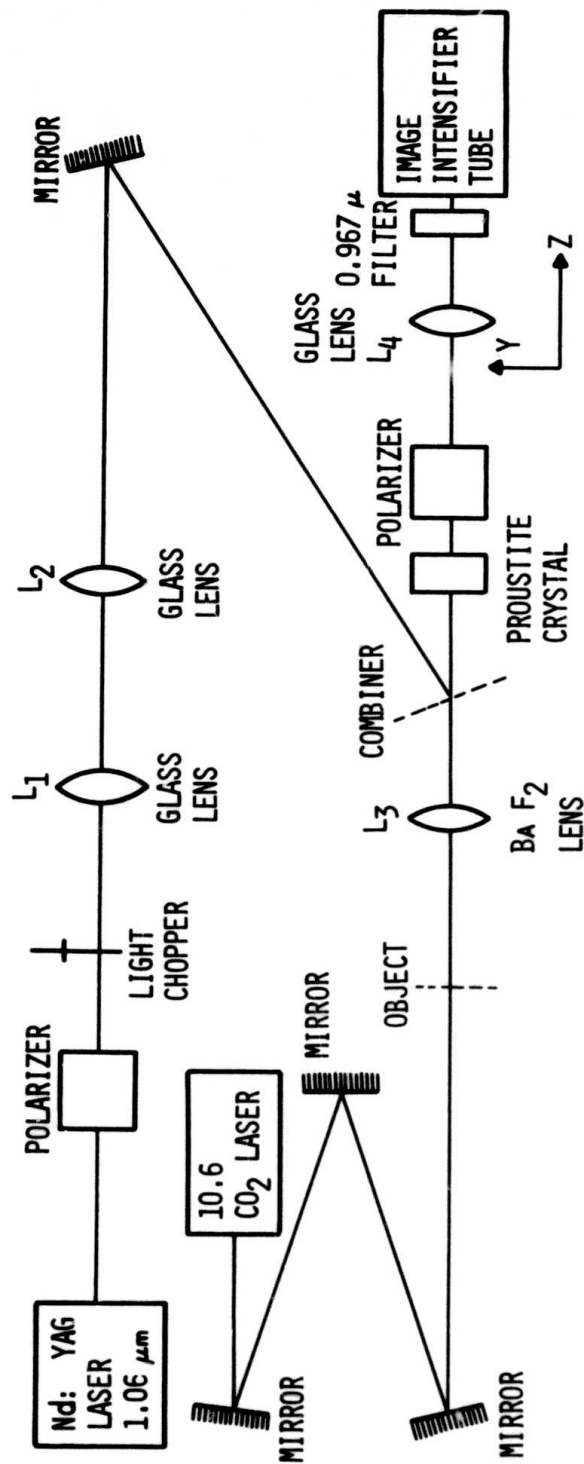
FIGURE A-1. SCHEMATIC DIAGRAM, EXPERIMENTAL MODE
IMAGE UPCONVERTER SYSTEM

2-4804
V73-670

A polarizer external to the Nd:YAG laser removes field components polarized along the y direction. The chopper reduces the average power of the pump beam by serving as an attenuator when required. Glass lenses L_1 and L_2 collimate and expand the pump beam.

A multimode CO_2 laser radiating with an electric field polarized perpendicular to the plane of the paper was used to back illuminate the transparent 1951 USAF resolution chart. The CO_2 beam diameter at the resolution chart is sufficiently large to illuminate the entire resolution chart by adjusting the 10.6-μm path length by means of mirrors as shown in Figure A1-. The position of BaF_2 lens L_3, relative to the proustite crystal and the object, is determined by the configuration of the system (image space or Fourier space).

The pump wave and the object wave are combined by a dichroic mirror. An improved dichroic mirror was obtained during this reporting period. This mirror reflects more than 99 percent of the YAG beam and has a transmission loss at 10.6 μm of about 13 percent. As shown in Figure A-1, the angle of incidence of the YAG beam on the dichroic mirror is about 20°. This eliminates potential vignetting of 10.6-μm object waves by the mirror holder.

A Glan air polarization filter and narrowband interference filters are used for suppression of 1.06-μm pump wave. Transmission through these filters at 0.967 μm is about 10 percent. Lens L_4 is used to form

upconverted real images on the photo surface of the image intensifier tube. The image intensifier tube is an ITT Model 4740 three-stage gated tube with an S-1 photocathode. Its pertinent characteristics are listed in Table A-2. The image intensifier tube can be cooled to -30°C with dry ice to reduce tube thermal noise.

TABLE A-2. CHARACTERISTICS OF ITT MODEL F4740 IMAGE TUBE

Useful Cathode Diameter	23 mm
Radiant Sensitivity at 0.967 μm	1.3 mA/W
Center Resolution	28 lp/mm
Peripheral Resolution	25 lp/mm at 7.0-mm radius
Paraxial Magnification	0.84
Distortion	18 percent at 10-mm radius
Luminous Gain	6000 fL/fc
Conversion Efficiency at 1.06 μm	$1,000,000 \dfrac{L(P-20)}{W(1.06)}$
Radiant Power Gain Peak Wavelength	1040 W/W
Radiant Power Gain 1.06μ	208 W/W
Equivalent Background Energy Input at Peak Wavelength	2×10^{-9} W/cm^2
Equivalent Background Energy Input at 1.06μ	8×10^{-9} W/cm^2

To check the resolving power of the 0.967 μm image detector used in the system, consisting of lens L_4, the interference filter, the image intensifier tube, and the camera, the resolution chart is illuminated with visible light and imaged on the photosurface of the image intensifier tube. Figure A-2 shows a typical image recorded on the film. The smallest

2-4805
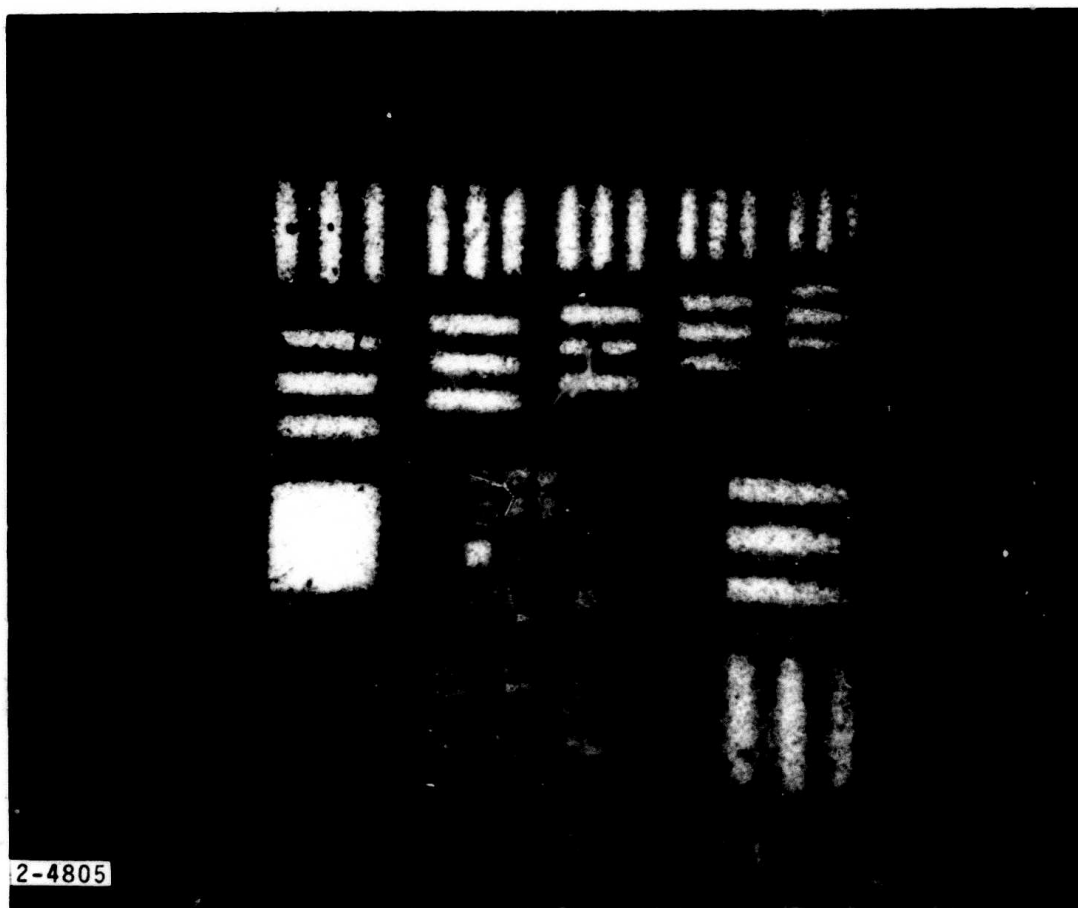
RESOLUTION LIMITS OF THE 0.967-μm IMAGE
DETECTOR OF THE EXPERIMENTAL MODEL IS 37 μm
AS SEEN IN THE ILLUSTRATION

FIGURE A-2. IMAGE OF THE RESOLUTION CHART ILLUMINATED
BY VISIBLE LIGHT

resolvable linewidth on the output phosphor of the image tube is 37 μm.
A modified polaroid scope camera was used to record the upconverted images
produced by the image tube.

2. IMAGE UPCONVERSION IN FOURIER SPACE

The limiting resolving power of the experimental model was
measured by operating the model in Fourier Space configuration and pump-
ing the nonlinear material with a TEM_{00} mode beam. Diffraction limited
image upconversion is possible for this configuration if the pump is a plane
wave. Thickness aberrations are negligible for this configuration.

A 1951 USAF resolution chart was placed in the front focal plane
of lens L_3. The distance between BaF_2 lens L_3 and the proustite crystal is
120 mm which is equal to the focal length of lens L_3. Lens L_4 is placed so
that the proustite crystal and the photocathode of the image intensifier tube
coincide with the front and back focal planes of lens L_4, respectively. The
focal length of lens L_4 is 580 mm.

The pump beam diameter at the proustite front face is 1.1 cm and its
beam divergence is 0.16 mrad. The pump beam is in TEM_{00} transverse mode.
Pictures reproduced from some of the upconverted images and recorded
by the polaroid camera are shown in Figure A-3. The smallest element that
can be visually resolved in these figures is the group 2/1. Figure A-3A has
better resolution along the x direction, but Figure A-3B has better resolution
along the y direction. (See Figure A-1 for the coordinate system.) Inspection
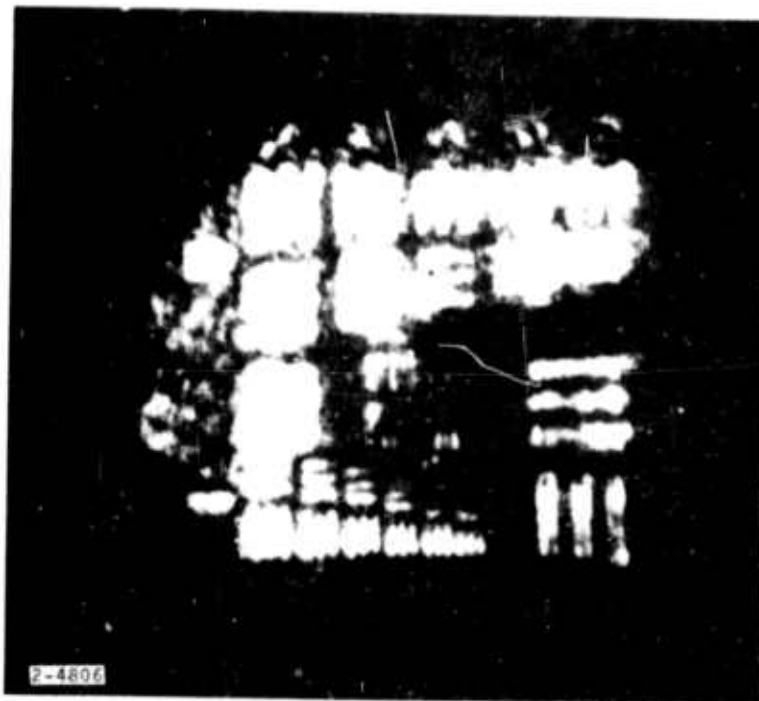
A. BETTER RESOLUTION ALONG X-DIRECTION

B. BETTER RESOLUTION ALONG Y-DIRECTION

FIGURE A-3.   UPCONVERTED IMAGE OF 1951 USAF TEST CHART
PRODUCED BY FOURIER SPACE UPCONVERTER

of upconverted images on the output phosphor surface of the image intensifier tube indicates that group 1/6 is resolved along both the x and the y directions. The system angular resolution is calculated by the formula

$$\gamma = h_{ir}/f_3 \qquad (A-1)$$

where

h_{ir} = resolvable linewidth of the test chart

f_3 = effective focal length of lens L_3

The measured angular resolution corresponding to the 1/6 and 2/1 resolution groups is:

Group 1/6 $\quad h_{ir} = 1/7.13 \text{ mm} = 1.17 \times 10^{-3} \text{ rad}$

Group 2/1 $\quad h_{ir} = 1/8 \text{ mm} = 1.04 \times 10^{-3} \text{ rad}$

Measured angular resolution of 1.17 mrad is 2.5 times larger than the Rayleigh resolution angle of 3-cm diameter lens L_3.

Resolution degradation from the Rayleigh resolution angle of the object lens is mainly due to nonuniform transverse intensity distribution of the pump beam. It will be shown later that a Gaussian profile of the pump beam would introduce an additional Gaussian attenuation factor on the angular spectrum of the upconverted image field. It is, therefore, expected that the resolving power of the experimental model is limited by the Gaussian window diffraction rather than the object lens diffraction.

The system field of view was measured by translating the object along the x and y directions until the edge of the test chart disappeared. The measured system FOV of 0.183 rad (10.5^O) agrees with the previous result. Figure A-3A shows that the FOV covers more than the area occupied by the resolution chart. The number of resolvable elements contained in the FOV is found to be 156 by 156, if one takes group 1/6 as the minimum resolvable element. The image shown in Figure A-3A contains approximately 114 by 114 resolution elements.

The measured transverse magnification of 0.99 agrees within 10 percent of the estimated value of 1.08, which is calculated by the expression

$$\left| M \right| = \left| M_{uc} \ M_c \ M_T \right| \tag{A-2}$$

where

$$M_{uc} \left(= \frac{\lambda_s}{\lambda_{ir}} \ \frac{f_4}{f_3} = 0.44 \right) : \text{ upconversion magnification}$$

$M_c \ (= 2.94): \text{ camera magnification}$

$M_T \ (= 0.81): \text{ image tube magnification}$

3. IMAGE UPCONVERSION IN IMAGE SPACE

Image upconversion experiments were carried out with the experimental model arranged in the image space configuration. Lens L_3 of Figure A-1 was positioned such that a real 10.6-u m image of object is focused

onto the crystal. The photosurface of the image intensifier and the proustite crystal coincide with the conjugate planes of lens L_4.

It will be shown analytically in Appendix C that the resolvable image linewidth of the image space configuration upconverter pumped with a plane wave is limited by thickness aberration. It is the purpose of this experiment to measure the aberrations and to determine the limiting resolution of the image space configured upconverter. The Nd:YAG laser was operated in the TEM_{00} mode to minimize the effect of diverging pump beam.

Figure 4 shows reproduced pictures of upconverted images recorded by the camera. The magnification of image forming lenses L_3 and L_4 are, respectively, 0.304 and 2.76. The smallest resolvable group (1/3) has a linewidth of 2.52 lp/mm. The corresponding image width, calculated by dividing the resolvable target width by the magnification factor of lens L_3, is 60.3 μm.

An experimentally measured resolvable image linewidth of 60 μm is approximately a factor of 3 narrower than the resolvable image width predicted by the geometric optics calculation. As will be explained later, the physical optics calculation predicts that the minimum resolvable image width for the given parameter values is 68 μm. The experimental result agrees better with the physical optics prediction than with the geometric optics calculation.

In the geometric optics model, the analysis is based on the assumption that each infinitesimal slab of material is capable of forming an independent upconverted image. The concept of thickness aberrations is, therefore, introduced by considering the upconverted image as a congregation of images formed by infinitesimal slabs of upconverter material. It has been previously shown (by the Fourier optics treatment) that the aberration is physically introduced by imperfect phase matching of angular spectra of the interacting electric fields. The angular spectrum with higher spatial frequency suffers higher attenuation due to the phase mismatch. The degree of phase mismatch is proportional to the material thickness. In the physical optics model the upconverted image is formed by linear superposition of the upconverted rays (angular spectra) emanating from the exit surface of the material. It is expected that the aberrations calculated by these two models should be different from each other. The experimental results should agree better with the Fourier optics predictions rather than the geometric optics because the model is in better agreement with the actual physical process.

The number of resolution elements contained in the image shown in Figure A-4 is approximately 62 by 62 which is approximately a factor of two less than that obtained by the Fourier space configuration system. Measured system magnification is approximately 10 percent greater than the theoretical estimate.

The system angular resolution can be calculated by dividing the measured resolvable image width by the distance between the crystal and
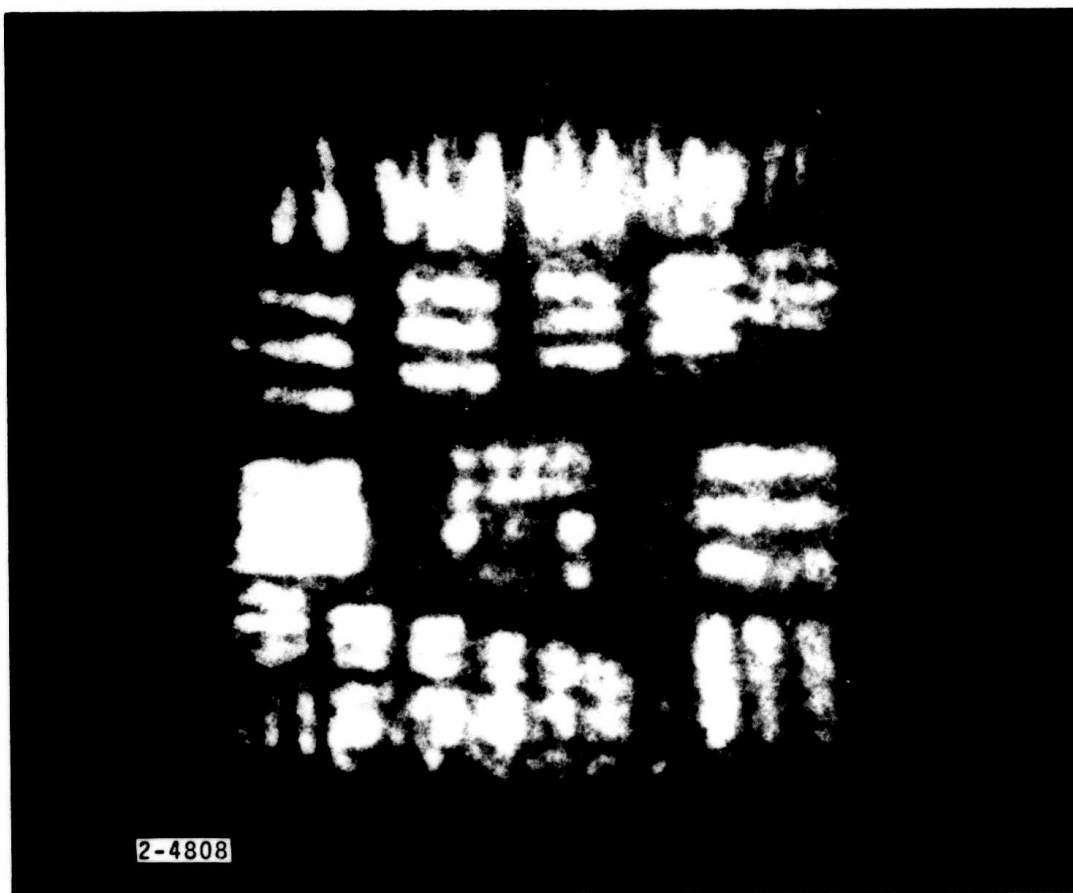
FIGURE A-4. UPCONVERTED IMAGE OF 1951 USAF TEST CHART PRODUCED BY IMAGE SPACE UPCONVERTER WITH SINGLE MODE PUMP

A-14

lens L_3. Measured system angular resolution of 0.4 mrad is very close to the Rayleigh resolution angle of 0.42 mrad of lens L_3. The experimental model is, therefore, nearly diffraction limited.

It must be noted that the Gaussian distribution of the pump beam does not degrade the resolution as expected from the physical optics analysis. It can easily be shown that the Gaussian amplitude factor of the angular spectrum of the upconverted image fields becomes unity for all angular frequencies in the image space configuration where the apparent IR object location coincides with the nonlinear material.

The primary effect of Gaussian profile of the pump beam appears as intensity reduction of upconverted images toward the edge of FOV. The size of the 10.6-μ m image of the object formed at the crystal would, therefore, be considerably smaller than the pump beam size if one wants to avoid intensity reduction at the outer edge of FOV. In the experiment, the size of the 10.6-μm image of the resolution chart at the crystal was 3.6 mm by 3.6 mm (considerably smaller than the pump beam diameter). Loss of brightness and resolution at the edge can even be seen in Figure A-4, which was taken with some precaution to minimize the Gaussian window effect. If the pump beam is expanded to 1-inch diameter and usable pump power is increased by four times that of the present system, the number of resolution elements could be increased to a minimum of 130 by 130, since the resolvable image width remains the same.

It was proved experimentally that the resolvable image width was unchanged while the magnification of lens L_3 did change.

4. IMAGE SPACE UPCONVERSION WITH A MULTIMODE PUMP BEAM

The purpose of this experiment is to prove that a multimode pump beam can be used in the image space configuration system without sacrificing the resolving power from the single mode pumped image space system. It is widely recognized that the image resolution degrades with an increase of pump beam divergence. This has been demonstrated experimentally for the Fourier space configuration upconverter and for the optical system in which an apparent IR object is located at finite distance from the nonlinear crystal.

The reduction of image resolution due to the pump beam divergence (or equivalently the pump beam profile) has been analyzed by the ray tracing technique and the physical optics approach. It has been shown that the amplitude of the angular spectrum of the upconverted image of an on axis point object contains an attenuation factor that depends on the pump beam intensity distribution and the object position. This attenuation factor becomes independent of the pump beam profile when the apparent IR object plane coincides with the equivalent pump beam plane. The resolving power then becomes insensitive to the pump beam profile and will be limited by the thickness aberration. It must be understood, however, that the intensity distribution of the upconverted image depends strongly on the pump

beam intensity distribution. In order to prevent undesirable image intensity variation across the FOV in the image space configuration system, a randomly phased multimode pump beam is preferred over a beam in a single (or a few) higher order modes which may have holes in the beam.

Figure A-5 shows reproduced pictures of an upconverted image of the resolution chart. The image shown in Figure A-5A was obtained with a TEM_{oo} mode pumped image space system. Figure A-5B shows an image obtained with the same system pumped with a multimode beam. The two images remain essentially the same, indicating no degradation of resolution due to the pump beam divergence. It was observed, however, that the image obtained from the multimode pump beam was less bright than that produced by the TEM_{oo} pumped beam. Quantitative comparison of image brightness for these two cases was not carried out.

It appears that dependence of upconversion efficiency upon the pump beam divergence requires further analytical and experimental investigation to design an efficient image upconversion system.

5.   IMAGE UPCONVERSION WITH A PULSED PUMP LASER AND A SYNCHRONOUSLY GATED IMAGE TUBE

An experimental model pulse-gated image upconversion system was assembled, and some preliminary experiments were carried out. The optical layout of the model is identical to the image space configuration (Figure A-1). A block diagram of electronics circuits used for the synchronous pump pulse generation and gating of the image tube is shown in Figure A-6.
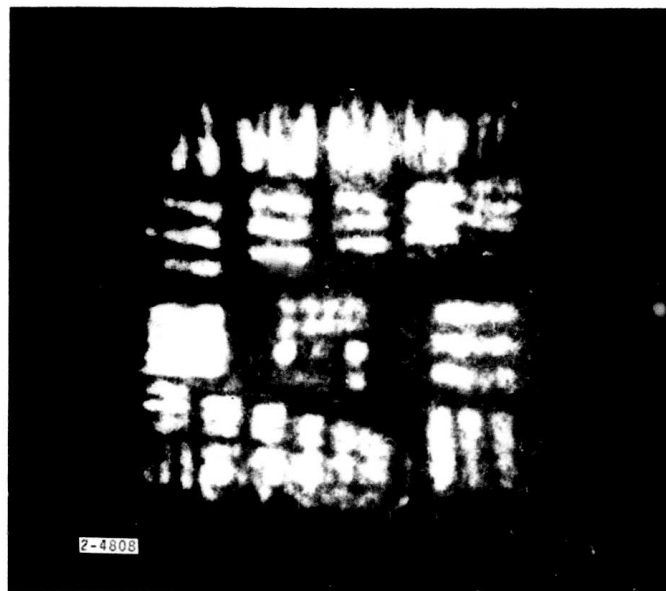
A. TEM$_{00}$ MODE PUMP
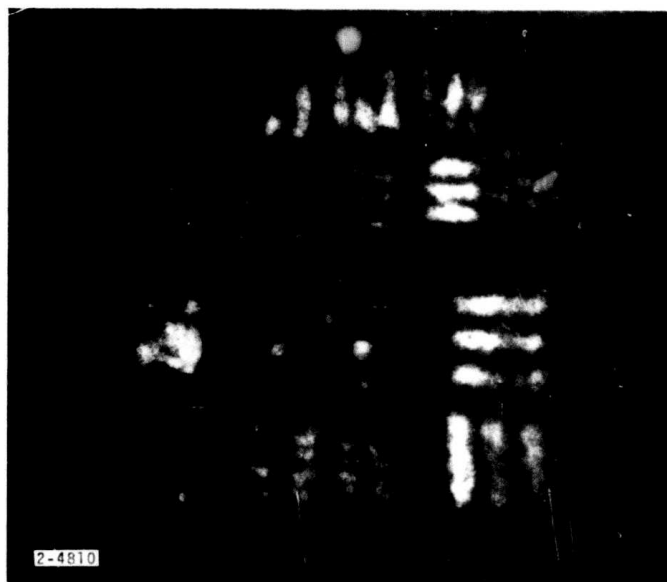
B. MULTIMODE PUMP

FIGURE A-5. UPCONVERTED IMAGE OF 1951 USAF TEST CHART PRODUCED BY IMAGE SPACE UPCONVERTER

Nd: YAG LASER

ACOUSTO-OPTICAL
Q SWITCH CELL

RF DRIVE

TRIGGER PULSE
AND LOW VOLTAGE
GATE PULSE
GENERATOR

Q SWITCH
DRIVER

HIGH VOLTAGE
GATE PULSE
GENERATOR

TO IMAGE INTENSIFIER
GATE GRID
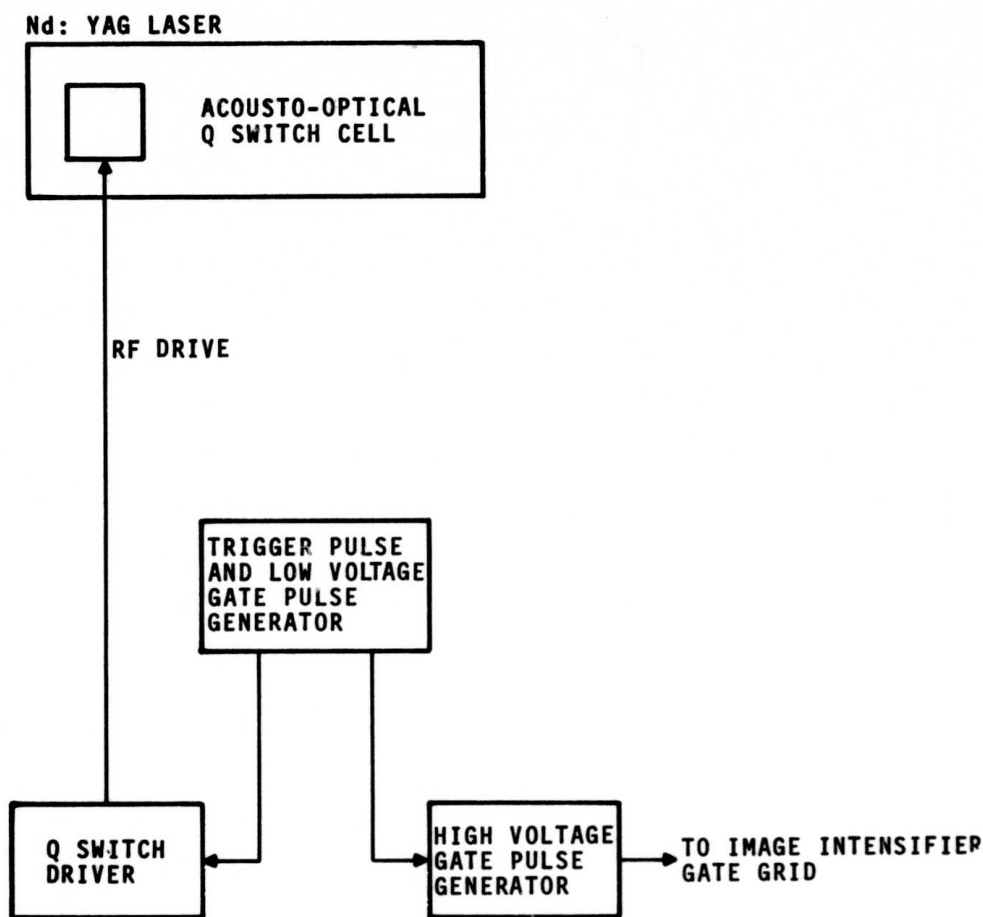
2-4811

FIGURE A-6. BLOCK DIAGRAM OF SYNCHRONOUS GATE
ELECTRONICS

The Nd:YAG laser operating in single transverse mode was Q-switched by an acousto-optical Q switch. The pulse repetition rate is controlled by the trigger pulse generator and can be varied from 1 to 5 kHz. Pump pulses with 200-ns duration and approximately 5-kW peak power were expanded to 1-cm diameter. No damage to the crystal was observed. The high voltage gate pulse generator has a 40-ns rise time and an 80-ns fall time. Pulse width and the pulse position of the gate pulses can be adjusted for the optimum image signal-to-noise ratio.

The images obtained with the synchronously gated image tube are shown in Figure A-7A. The image shown in Figure A-7B is obtained by the same system, but the image tube was not gated. The improvement in the image signal-to-noise ratio attained by gating the image is quite remarkable. Optimization of the experimental system for range-gated operation was not attempted to obtain Figure A-7A.
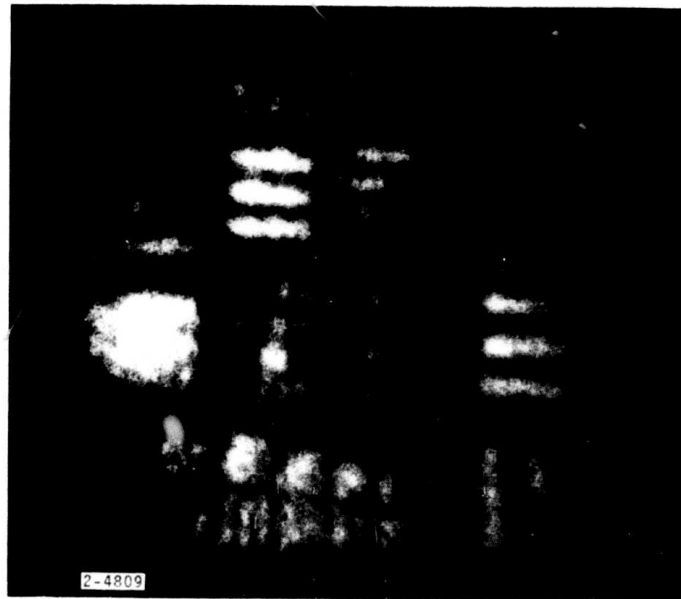
A. SYNCHRONOUSLY GATED IMAGE TUBE

B. UNGATED IMAGE TUBE

FIGURE A-7.   UPCONVERTED IMAGE WITH A PUMP BEAM

A-21

APPENDIX B
UPCONVERSION EFFICIENCY MEASUREMENTS

Conversion efficiency of the upconversion process has been measured and compared to a theoretical calculation based on the plane wave theory by several authors[1,2,3]. Measured efficiency, the conversion efficiency formula used for checking their results, and parameter values such as SHG d coefficients are inconsistent among investigators. In this section, an attempt will be made to clarify some of the confusion by considering:

- Proustite SHG d coefficients
- Experimental measurement of upconversion efficiency under controlled experimental conditions

1. PROUSTITE SHG d COEFFICIENTS

The only reported measurement of SHG d_{31} coefficients of proustite was performed by K. H. Hulme et al by comparing SHG of 1.152 μm with proustite to SHG with $LiNbO_3$ along the crystallographic X-axis[4]. The ratio $|d_{22}|/|d_{31}|$ of proustite was determined by Hulme et al by the frequency summing technique[4]. Their measurement did not determine the absolute signs of the coefficients. Their measured results are

$$\left| d_{31}^{P} \right| = 2.6 \left| d_{31}^{LN} \right|$$

$$\left| d_{22}^{P} / d_{31}^{P} \right| = 1.6 \pm 0.1$$

(B-1)

The inconsistency in proustite d_{31} is resulted from the spread in $LiNbO_3$ d_{31} coefficient reported in the literature as shown below.

G. Boyd[5]

$$d_{31}^{(LN)} = (10.6 \pm 1.0) \, d_{36}^{(KDP)}$$

R. Miller and Savage[6]

$$d_{31}^{(LN)} = (11.9 \pm 1.7) \, d_{36}^{(KDP)}$$

Bjorkholm[7,8]

$$d_{31}^{(LN)} = (10.9 \pm 1.7) \, d_{36}^{(KDP)}$$

Byer and Harris[9]

$$d_{31}^{(LN)} = 11.0 \, d_{14}^{(KDP)} = 10.6 \, d_{36}^{(KDP)}$$

Careful review of the above reported measurements indicates that Bjorkholm's measurement seems more accurate than others.

Using Jerphagnon and Kurtz[10] and Francois[11] measurement on d_{36} of KDP crystal,

$$d_{36}^{(KDP)} = 1.67 \times 10^{-9} \, esu$$

and Bjorkholm's $d_{31}^{(LN)}$ one finds

$$\left| d_{31}^{(P)} \right| = 28.4 \, d_{36}^{(KD)} = 42.6 \times 10^{-9} \text{ esu}$$

$$\left| d_{22}^{(P)} \right| = 45.5 \, d_{36}^{(KDP)} = 68.2 \times 10^{-9} \text{ esu}$$

(B-2)

Hulme[4] et al gave estimated d coefficients from their measurement as

$$\left| d_{22}^{(P)} \right| = 50 \, d_{36}^{(KDP)} = 75 \times 10^{-9} \text{ esu}$$

$$\left| d_{31}^{(P)} \right| = 30 \, d_{36}^{(KDP)} = 45 \times 10^{-9} \text{ esu}$$

(B-3)

The reason for this modification from experimental results was not given by Hulme.

Boggett[12] et al reported the effective d coefficient of Type I phase matched proustite by measuring doubled 10.6 μm output power. Their results for $\theta_m = 22.5^\circ$.

$$d_{eff} = 60 \, d_{36}^{(KDP)}$$

is higher than the calculated value based on Hulme's estimated d coefficients $d_{22}^{(P)} = 50 \, d_{36}^{(KDP)}$ and $d_{31}^{(P)} = 30 \, d_{36}^{(KDP)}$. If one solves the equation

$$d_{eff} = d_{22} \cos \theta_m + d_{31} \sin \theta_m$$

which applies to Type I phase matching, assuming $d_{32}/d_{31} = 1.6$ for proustite, one finds $d_{31}^{(P)} = 32.2\, d_{36}^{(KDP)}$ from the Boggett measurement. Boggett's result is very close to the Hulme's estimated d_{31} value.

The values $d_{22} = 68.2 \times 10^{-9}$ esu and $d_{31} = 42.6 \times 10^{-9}$ esu will be used for following system performance calculation, although Hulme's estimated d coefficients are widely adapted by other workers.

The choice is dictated by the conversion efficiency measurements performed at AIL. The result of the most recent conversion efficiency measurement is presented in paragraph 2.

2. CONVERSION EFFICIENCY MEASUREMENTS

The main purpose of the experiment is to assess the achievable conversion efficiency of a practical image upconverter as compared to the theoretical estimate. The experimental conditions for efficiency measurements must be carefully controlled in order that the experimental results can be meaningfully compared to the theory.

CW conversion efficiency of the experimental model was measured with TEM_{oo} mode signal beam and TEM_{oo} mode pump beam. The upconverted signal was detected by a low noise S1 photomultiplier with accurately calibrated quantum efficiency. Optical efficiency of optical components such as interference filter, optical windows, and the beam combining dichroic mirror were carefully calibrated. The pump beam was chopped with a duty factor of one quarter to prevent excessive crystal surface oxidation.

The input/output linearity was checked so that an efficiency measurement was taken within the dynamic range of the system. Figure B-1 shows the plot of input CO_2 power versus the upconverted signal induced photoelectron at the photocathode. The observed power upconversion efficiency is calculated by

$$\eta_u = \frac{N_s \, hC}{\eta_p d \, P_{ir} \, \lambda_s} \qquad (B-4)$$

where

N_s = photoelectron flux

η_p = quantum efficiency of the photomultiplier

h = Planck's Constant

C = velocity of light

λ_s = wavelength of upconverted signal

P_{ir} = IR input power

d = duty factor of light chopper

Using the following values:

$d = 0.25$

$\frac{hC}{\lambda_s} = 2.05 \times 10^{-19}$ Joules for $\lambda_s = 0.967 \, \mu m$

$\eta_p = 9 \times 10^{-4}$

$N_s = 4 \times 10^5$ Hz

$P_{ir} = 0.09$ W

2-4820
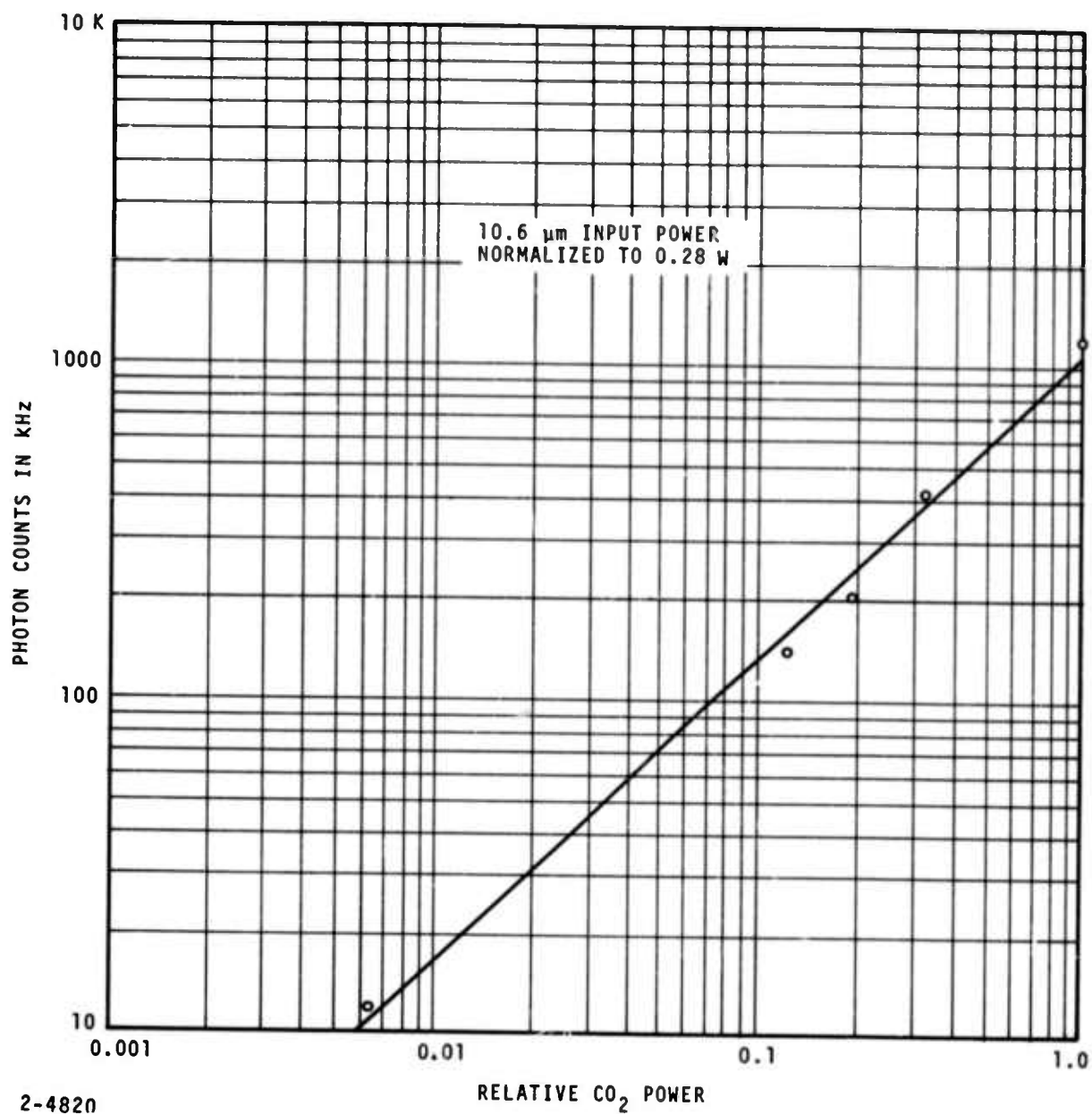
FIGURE B-1. UPCONVERSION LINEARITY PHOTON COUNTS
VERSUS RELATIVE CO$_2$ POWER

the measured system peak power conversion efficiency is 4.05×10^{-9} which is approximately one-third of the theoretical estimated efficiency of 1.46×10^{-8} calculated by the expression, which applies to upconversion of a TEM_{00} IR beam with a TEM_{00} mode pump beam,

$$\eta = \frac{P_s}{P_i} = \frac{104.44 \, d_{eff}^2 \, \ell^2 \, P_p \, t_{op}}{n_i \, n_s \, n_p \, \lambda_s^2 \, (A_p + A_i)} = 2.162 \times 10^{-6} \frac{t_{op} \, \ell^2 \, P_p}{(A_p + A_i)} \qquad (B-5)$$

where

P_s = total upconverted power in watts

P_i = total IR power in watts

P_p = pump power in watts

ℓ = interaction length in cm

n_ℓ = indices of refraction at (ℓ = i, p, s)

A_p = pump beam area in cm^2

A_i = IR beam area in cm^2

t = optical transmission of the experimental model

Parameter values used in the efficiency estimate are:

$d_{eff} = d_{22} \cos \theta_m = 68 \, (\cos 20^o) \times 10^{-9}$ esu = 64×10^{-9} esu

$n_i = 2.68$

$n_p = 2.817$

$n_s = 2.804$

$\ell = 0.6$ cm

$\lambda_s = 0.967 \, \mu m$

$A_p = 1.13 \, cm^2$ (beam diameter = 1.2 cm)

$$A_i = 0.783 \text{ cm}^2 \text{ (beam diameter} = 1 \text{ cm)}$$

$$P_p = 4.8 \text{ W}$$

$$t_{op} = 7.44 \times 10^{-3}$$

The most probable cause for the discrepancy between the measured efficiency and the prediction based on equation B-5 is the phase mismatch due to the beam divergence and internal pump beam scattering. Equation B-5 was derived for the case of perfectly phase-matched interaction of two TEM_{00} mode beams. Other factors affecting efficiency reduction are the beam walk-off, the crystal birefringence, and the crystal absorption.

CW system conversion efficiency under the experimental condition that nearly realizes the plane wave interaction model was measured. The measured conversion efficiency is approximately a factor of 1.75 less than the theoretical prediction calculated by equation B-5. In this measurement, the 10.6-μm beam was spatially filtered by a small pinhole placed at beam center. The filtered 10.6-μm wave front is very close to plane wave front. Beam divergence effect is minimized by aligning the optics so that the interaction of IR waves with the pump waves is limited to the center of the pump beam.

Conversion efficiency of pulse-gated upconverter was also measured to ascertain that there is no abnormality in this mode of operation. The Nd:YAG laser was acousto-optically Q-switched with a pulse repetition

rate of 1 kHz. Pulse width and pulse shape of pump laser outputs were measured with a high-speed Ge photodetector of known responsivity. Half-power pulse width and the peak power is 250 ns and 2.5 kW, respectively. Upconverted peak power and the pulse shape are measured with another Ge photodiode of known responsivity. Pump beam power density at the center of beam was about 5 kW/cm^2. Transmittance of optical components was improved to 0.28 for the gated model. Measured upconversion efficiency of 4.1×10^{-5} is about one-third of the estimated value 1.1×10^{-4} calculated by equation B-5. The accuracy of above conversion efficiency measurement is about 50 percent since the calibration of optical attenuator used for the pump power measurement could not be calibrated better than 50-percent accuracy. The result obtained for pulse pumped upconverter agrees with that of CW upconverter.

Conversion efficiency of image upconversion must be defined differently from equation B-5 since there are many resolution elements in the upconverted image. It can be shown that the conversion efficiency defined as a ratio of upconverted power density to IR object power density for a pair of conjugate points is given by:

$$\eta(\underline{\rho}_s) = \frac{W_s(\underline{\rho}_s)}{W_i(\underline{\rho}_i)} = \frac{52.22 \, d_{eff}^2 \, \iota^2 t \, P_p}{n_i n_s n_p \lambda_s^2 A_p} \, F(\underline{\rho}_s) \tag{B-6}$$

where:

t = total surface transmittance at the crystal surfaces

$F(\underline{\rho}_s)$ = Envelope factor which depends on the optical configuration and pump beam envelope

$\underline{\rho}_s$ = radial distance of image point measured from the optic axis

$\underline{\rho}_i$ = radial distance of the conjugate object point

For a TEM_{oo} mode beam pumped Type I system, the envelope factor is expressed

$$F_I(\rho_s) = e^{-2\rho_s^2/a^2} \tag{B-7}$$

where

a = pump beam radius

For a TEM_{oo} mode beam pumped Type III system, we have

$$F_{III}(\rho_s) = Sinc^2 \left(\frac{\pi \, \ell \, n_p \, \lambda_i \, \rho_s^2}{2 \, n_s \, n_i \, \lambda_p \, \lambda_s \, f_2^2} \right) \tag{B-8}$$

where f_2 = focal length of second Fourier transform lens.

APPENDIX C
THEORETICAL ANALYSIS

1.   INTRODUCTION

Imaging theory of parametric image upconversion was treated previously by the geometric optics approach. An equation relating locations of object, pump, and image was derived and the existence of image aberrations due to the finiteness of the nonlinear material thickness was made clear. In geometric optics treatment of parametric image upconversion, some higher order factors that would affect imaging properties were neglected. It was considered also in the geometric optics theory that upconverted image is formed by constructive interference between the waves radiated from each differential slab of polarization in the material. This concept leads to thickness aberration of the image upconversion. To verify the concept of constructive interference and to understand the higher order effects, such as, anisotropy, phase mismatch, and finite interaction aperture, the problem must be treated in the formalism of physical optics. It is the purpose of this study to treat the problem in the framework of scalar wave theory. The problem considered here is to determine the nature of the image field arising from a dielectric polarization generated at the sum frequency by interaction of the object field and the pump field in the nonlinear material. The imaging properties of the parametric image upconversion

have been treated by Firester[13] in the formalism of Fourier optics[14] that resembles closely the treatment of linearly invariant filter system. The advantage of such an approach is that the process of upconversion of the complex nonplanar objects field to the complex nonplanar image field can be studied by investigating the interaction of planar angular spectrum components in the nonlinear material. The results obtained by Fourier optics treatment describe more quantitatively the imaging properties of upconversion process and can be tied directly to the formalism of optical transfer function description of an imaging system.

General formulation of image upconversion process taking into account of phase mismatch and the crystal anisotropy is presented in paragraph 2. The treatment presented follows Kleinman[15] closely and is more rigorous than Firester[13]. The basic equations that describe the angular spectrum of image field in terms of object and pump angular spectrum are obtained. The concept of constructive interference of radiation from differential slabs is also verified in paragraph 2. Imaging properties, such as angular spectrum of image field, image position, and the point spread function of two image upconversion systems, namely Fourier space configuration system and image space configuration system, are considered in paragraphs 3 and 4. Imaging with a high order mode pump and the effects of birefringence on the image properties are discussed in paragraphs 5 and 6.

2.   GENERAL FORMULATION

a.   BASIC EQUATIONS

Mathematically, the formulation is based upon Maxwell's equation for a lossless anisotropic medium free of charges and currents but containing a prescribed source in the dielectric polarization. All linearly induced polarization is assumed to be included in the dielectric constant tensor. The analysis follows very closely to Kleinman's treatment[15, 16] of second-harmonic generation except that the analysis will be carried out in Fourier spatial frequency space rather than in spatial coordinate space. It can be shown that the Fourier decomposed angular spectrum of the field disturbance can be considered as plane waves propagating in different directions. Parametric interaction of complex (nonplanar) waves in the nonlinear material can be understood by studying the interaction of their angular spectrum components. The Fourier optics formalism puts the problem in the framework of linear transferse-spatial invariant system.

The theory of parametric upconversion involving three plane waves has been treated in considerable detail[17, 18, 19]. Under matching conditions the plane wave signal field $E_i(z)$ and the output plane wave sum frequency field $E_s(z)$ satisfy the relations[18].

$$E_s(z) = \left(\frac{\omega_s}{\omega_i} \right)^{1/2} E_i(0) \sin \left(\frac{\pi z}{\ell} \right) \left(\frac{n_i}{n_s} \right)^{1/2} \qquad (C-1)$$

and

$$E_i(z) = E_i(0) \cos\left(\frac{\pi z}{\ell}\right) \tag{C-2}$$

where the characteristic length ℓ for power conversion

$$\ell^{-1} = \frac{2\omega_i \omega_s \chi}{C^2(K_i K_s)^{1/2}} E_p(0) \tag{C-3}$$

with K the wave number, ω the angular temporal frequency, χ the appropriate component of the second-order polarization tensor, and $E_p(0)$ the pump electric field at input surface of the nonlinear material. In the limit $z \ll \ell$, the sum-frequency field is given by[17],

$$E_s(z) \approx 2\pi\chi \frac{1}{n_s} \frac{\omega_s}{C} E_i(0) E_p(0) z \tag{C-4}$$

As shown by Kleinman[15], the linear growth of $E_s(z)$ is ascribed to constructive interference between a forced wave generated by the polarization and a free wave generated at the surface by the forced wave. It is equally valid, as we shall see later, to ascribe the growth to constructive interference between the waves radiated from each differential slab of polarization in the material. We developed geometric optics theory according to latter view. Equation C-4 is the solution for the matching case satisfying $E_s(0) = 0$. Actually equation C-4 does not give the correct sum-frequency field. The

value of $E_s(0)$ is related to the amplitude of nongrowing waves in the medium and a reflected wave at the surface[15, 18, 20]. These waves are, however, many orders of magnitude weaker than the growing wave.

The rigorous analysis of upconversion process is based upon the inhomogeneous vector wave equation[18, 15, 16].

$$\nabla \times \nabla \times \underline{E}_s(\underline{r}) - \left(\frac{\omega_s}{C}\right)^2 \underline{\underline{\epsilon}} : \underline{E}_s(\underline{r}) = 4\pi \left(\frac{\omega_s}{C}\right)^2 \underline{P}(\underline{r}) \qquad (C-5)$$

where $\underline{\underline{\epsilon}} = \underline{\underline{I}} + 4\pi \underline{\underline{\chi}}^{(1)}$ [$\underline{\underline{\chi}}^{(1)}$ is the linear susceptibility tensor] and $\underline{E}_s$ are respectively dielectric constant tensor and electric field at the frequency $\omega_s = \omega_i + \omega_p$. The plane polarization wave $\underline{P}(\underline{r}, t)$ is related to the signal electric field $\underline{E}_i(\underline{r})$ and pump field $\underline{E}_p(\underline{r})$ by the relation

$$\underline{P}(\underline{r}, t) = \underline{P}(\underline{r}) e^{-i\omega_s t} = \underline{\underline{\chi}} : \underline{E}_i(\underline{r}) \underline{E}_p(\underline{r}) e^{-i(\omega_i + \omega_p)t} \qquad (C-6)$$

For nonplanar signal and/or pump fields, which is the case for imaging, it would be advantageous to solve the inhomogeneous wave equation for the angular spectrum component waves rather than solving equation C-5 directly. The wave equation for Fourier components wave is

$$\nabla \times \nabla \times \underline{\mathcal{E}}_s(\underline{\kappa}_s, z) - \underline{\underline{\epsilon}}_e : \underline{\mathcal{E}}_s(\underline{\kappa}_s, z) = 4\pi \left(\frac{\omega_s}{C}\right)^2 \underline{\mathcal{P}}(\underline{\kappa}_s, z) \qquad (C-7)$$

It is apparent that operation ∇ on angular spectrum only has $\frac{\partial}{\partial z} \dot{z}_0$ operation. In this analysis Cartesian coordinates x, y, z are defined such that z is in the propagation direction normal to the surface of the crystal, and the optical axis (consider only uniaxial crystals) is in the xz plane (Figure C-1). If both signal and pump fields are ordinary wave polarized with the electric vectors perpendicular to the xz plane (along the y direction) the effective component of the polarization wave and the sum-frequency electric field are polarized along the x axis. For this simple case equation C-7 becomes

$$\left(\frac{\partial^2}{\partial z^2} + \epsilon_e \right) \mathcal{E}_{sx}(\underline{K}_s, z) = 4\pi \left(\frac{\omega_s}{C} \right)^2 \mathcal{P}_x(\underline{K}_s, z) \qquad (C-8)$$

where

$$\epsilon_e = (\underline{\underline{\epsilon}}_e)_{11}$$

$$\mathcal{P}_x = \chi \, \mathcal{E}_{iy}(\underline{K}_s, z) \otimes \mathcal{E}_{py}(\underline{K}_s, z)$$

The general solution of equation C-7 consists of an inhomogeneous wave (or forced wave) which is some convenient particular solution of inhomogeneous equation, and suitable free waves which are solutions of the homogeneous equation obtained by setting $\mathcal{P}_s = 0$. The free waves are required so as to satisfy the boundary conditions at the crystal surface.
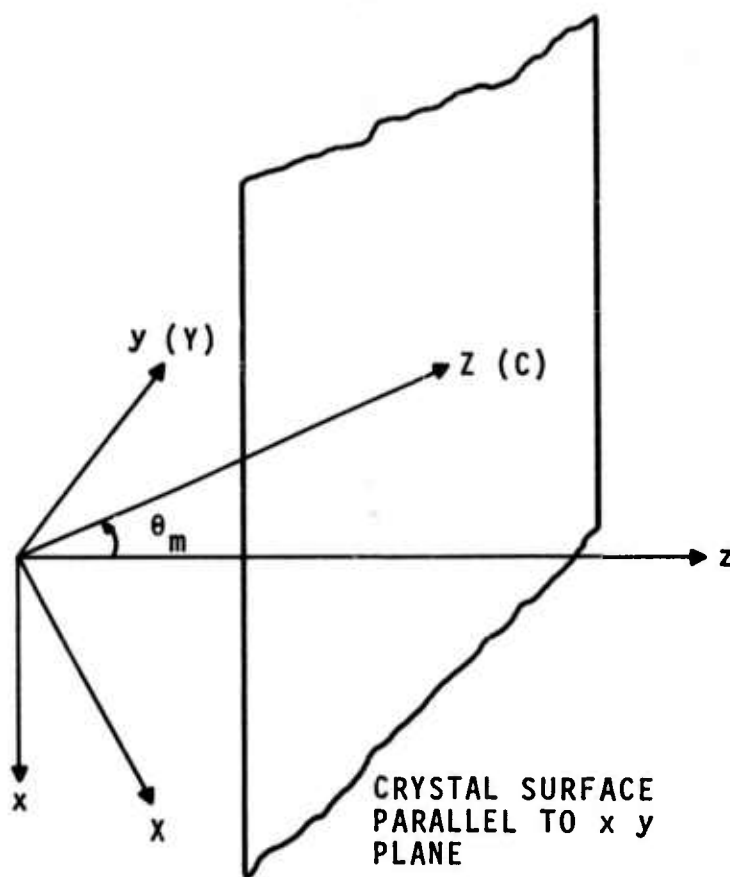
2-4817

FIGURE C-1. RELATION BETWEEN THE COORDINATES (x, y, z) AND
THE CRYSTALLOGRAPHIC AXES (X, Y, Z)

The free waves have the form

$$\mathcal{E}\,\underline{u}\,\exp\,i\left(\frac{\omega_s^2}{C^2}n_s^2 - \kappa_s^2\right)^{1/2} z \qquad \text{(C-9)}$$

where the refractive index n_s is a function of the free wave propagation direction $\underline{s}$ (unit vector) of the wave vector

$$\underline{K} = \frac{\omega_s}{C}\,n_s\,\underline{S} \qquad \text{(C-10)}$$

The relation between the wave vector $\underline{K}$ of free wave and the wave vector $\underline{K}_s$ of the polarization wave $\underline{P}_s(\underline{r})$ will be considered later. The polarization direction $\underline{u}$ satisfies the relation

$$\underline{\underline{\alpha}}_s : \underline{u} = 0 \qquad \text{C-11)}$$

where

$$\underline{\underline{\alpha}}_s = \frac{\omega_s^2}{C^2}\,(n_s\underline{\underline{I}} - \underline{\underline{\epsilon}}) - \underline{\kappa}_s\underline{\kappa}_s \qquad \text{(C-12)}$$

where $\underline{\underline{I}}$ is the unit dyadic and $\underline{\underline{\epsilon}}$ is the dielectric constant tensor at sum frequency ω_s. Equations C-11 and C-12 determine both n_s and the polarization direction $\underline{u}$. We define a quantity n', called effective index, and a unit vector $\underline{\sigma}$ by the relation

$$\underline{K}_s = \frac{\omega_s}{C}\,n'\,\underline{\sigma} \qquad \text{(C-13)}$$

In general $n' \neq n_s(\underline{\sigma})$, but $n' = n_s(\underline{\sigma})$ along the phase-match direction.

C-8

When $n' \neq n_s(\underline{\sigma})$, the polarization wave is said to be mismatched, the mismatch is described quantitatively by $\emptyset$ in the relation[15]

$$n' \underline{\sigma} - n_s \underline{s} = \emptyset \underline{N} \tag{C-14}$$

or

$$\underline{K}_s - \underline{K} = \frac{\omega_s}{C} \emptyset \underline{N} \tag{C-15}$$

where $\underline{N}$ is the direction (unit vector) normal to the incident surface of the crystal. These equations determine both $\emptyset$ and $\underline{s}$ to be associated with a prescribed $\underline{K}_s$. Here n_s and $\underline{s}$ specify a free wave expressed by equation C-9 which must exist in the presence of the forced wave in order to satisfy boundary condition at the crystal surface. The dominant effect of presence of both forced and free waves is the production of growing wave through interference of a free wave and forced wave[15]. When $\emptyset = 0$ the waves are said phase matched and the growing wave is given by equation C-4. More generally under nearly matching conditions following Kleinman[15] it can be shown that the growing wave is given by

$$\underline{\mathcal{E}}_s(\underline{\kappa}_s, z) = z \, G(2 \, i \, \psi) \, \underline{\underline{\gamma}} : \underline{\mathcal{P}}(\underline{\kappa}_s, z) \tag{C-16}$$

where

$$G(a) = \frac{1 - e^{-a}}{a} = \int_0^1 e^{-ax} dx \tag{C-17}$$

and

$$2\psi = \frac{\omega_s}{C} \phi z = z \ |\underline{K}_s - \underline{K}|$$ (C-18)

The dyadic $\underline{\underline{\gamma}}$ is defined by[15]

$$\underline{\underline{\gamma}} = 2\pi i \frac{\omega_s}{Cn_s} [(\underline{N} \cdot \underline{u})(\underline{\sigma} \cdot \underline{u}) - \underline{N} \cdot \underline{\sigma}]^{-1} \underline{u} \, \underline{u}$$ (C-19)

To a good approximation $\underline{\gamma}$ can be written[15]

$$\underline{\underline{\gamma}} = 2\pi i \frac{\omega_s}{Cn_s} \underline{u} \, \underline{u}$$ (C-20)

provided waves travel nearly normal to the surface. For the case of an ordinary pump wave, an ordinary signal wave, and an extraordinary sum-frequency wave, the growing wave in equation C-16 becomes

$$\mathcal{E}_{sx}(\underline{\kappa}_s, z) = 2\pi i \frac{\omega_s}{Cn_s} z \ G(2 \, i\psi) \ \mathcal{P}_x(\underline{\kappa}_s, z)$$ (C-21)

Equations C-16 and C-21 can be written in more familiar form[13] by noting that

$$G(2i\psi) = e^{-i\psi} \frac{\sin \psi}{\psi}$$ (C-22)

b.   EVALUATION OF MISMATCH FACTOR

Before equation C-16 can be applied it is necessary to express
the mismatch factor $\emptyset$ in terms of wave vectors. Equation C-15 gives that

$$\emptyset = \frac{\omega_s}{C} (\underline{K}_s - \underline{K}) \cdot \underline{N} \qquad (C-23)$$

As shown in Figure C-2 the wave vector $\underline{K}$ of free waves is constrained to
lie on the wave vector surface $\frac{\omega_s}{C} n (\underline{s})$ for the sum frequency ω_s; the wave
vector $\underline{K}_s$ of polarization wave is given by $\underline{K}_s = \underline{K}_i + \underline{K}_p$ and is arbitrary.
We shall denote the wave vector of polarization wave in the matching direc-
tion by $\underline{K}_M$. We shall assume, for simplicity, that the surface Normal $\underline{N}$ is
a matching direction and also that $\underline{K}_M$ is in the direction $\underline{N}$. Figure C-2
shows geometrically the mismatch relation expressed by equation C-23. We
have taken the z direction to be along $\underline{N}$, the optic axis in the xz plane, and
the y direction normal to the plane of figure. The tangent plane to the wave
vector surface at $\underline{K}_M$ is shown, and the normal to this plane makes the
angle ζ with the z axis. It should be noted that the angle ζ represents aniso-
tropy of the crystal at the frequency ω_s. The anisotropy angle ζ is given by:

$$- \tan \zeta = n^2(\theta_m) \cos \theta_m \sin \theta_m \left(\frac{1}{n_e^2} - \frac{1}{n_o^2} \right) \qquad (C-24)$$

where θ_m = angle between the optic axis and the phase match directon

   $n(\theta_m)$ = index of refraction along $\underline{K}_M$ at ω_s

   n_e = extraordinary-wave index of refraction at ω_s

   n_o = ordinary-wave index of refraction at ω_s
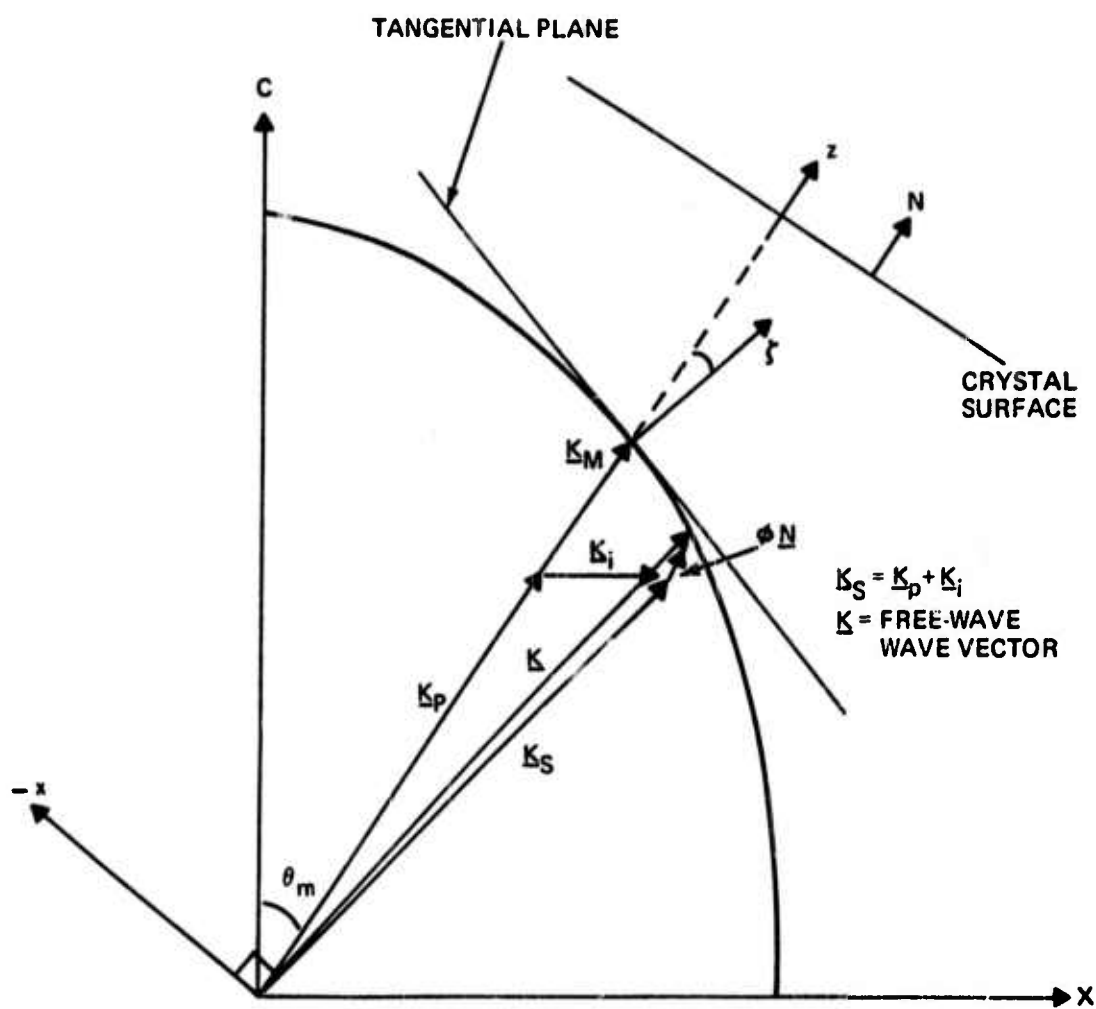
FIGURE C-2. GEOMETRIC REPRESENTATION OF MISMATCH RELATION

3-1181

This angle also governs the double refraction effect, in which both the ordinary and extraordinary waves are at the same frequency. In this analysis it was assumed that the signal field and the pump field are both polarized as ordinary waves and the sum-frequency field is polarized as extraordinary waves. The mismatch factor $\emptyset$ according to equation C-23 is the distance from $\underline{K}_s$ to the wave vector surface measured parallel to $\underline{N}$. This is apparent from the boundary condition that requires continuity of transverse wave vectors of both forced and free waves across the boundary surface.

$$\underline{\kappa} = \underline{\kappa}_s = \underline{\kappa}_p + \underline{\kappa}_i \qquad (C-25)$$

This condition assures also the continuity of an angular spectra with spatial angular frequency $\underline{\kappa}_s$ across the crystal boundary. It is somewhat tedious but can be shown that:

$$\frac{\omega_s}{C} \emptyset = K_{sz} - K_M - \kappa_{sx} \tan \zeta + \frac{K_M}{2} \left[\left(\frac{K_M \kappa_{sx} C^2}{n_e n_o \omega_s^2} \right)^2 + \left(\frac{\kappa_{sy} C}{n_e \omega_s} \right)^2 \right] \qquad (C-26)$$

where

$$\underline{\kappa}_s = \kappa_{sx} \hat{x}_o + \kappa_{sy} \hat{y}_o$$

and

$$K_{sz}^2 = (K_s^2 - \kappa_s^2)$$

Since the crystal is usually nearly isotropic and the quantity in the square bracket is second-order in $(\underline{K}_s - \underline{K})$ and smaller than the linear quantity, it is proper to use simpler form

$$\frac{\omega_s}{C}\, \phi \approx K_{sz} - K_M - \kappa_{sx}\, \zeta + \frac{\kappa_s^2}{2K_M}. \qquad \text{(C-27)}$$

We have used $\tan \zeta = \zeta$ in equation C-27 since $\zeta \ll 1$.

c.   RESULTANT SUM-FREQUENCY FIELD

The sum-frequency angular spectrum component $\underline{\mathscr{E}}_s(\underline{\kappa}_s, z)$ given by equation C-16 is generated by a plane wave polarization $\underline{\mathscr{P}}(\underline{\kappa}_s, \zeta)$, which is a Fourier component of total polarization wave $\underline{P}(\underline{r})$. The resultant sum-frequency field produced by $\underline{P}(\underline{r})$ is Fourier transform of $\underline{\mathscr{E}}_s(\underline{\kappa}_s, z)$

$$\underline{E}_s(\underline{r}) = \int \underline{\mathscr{E}}_s(\underline{\kappa}_s, z)\, e^{i\underline{\kappa}_s \cdot \underline{\rho}} d\underline{\kappa}_s \qquad \text{(C-28)}$$

Substituting equation C-16 into equation C-28 the resultant field can be written

$$\underline{E}_s(\underline{r}) = z \int_0^1 d\eta \int \underline{\underline{\gamma}} : \underline{\mathscr{P}}(\underline{\kappa}, z)\, e^{-2i\psi\eta}\, e^{i\underline{\kappa} \cdot \underline{\rho}} d\underline{\kappa} \qquad \text{(C-29)}$$

where use has been made of integral representation in equation C-17.

For paraxial assumption the quadradic term $\kappa_s^2/2K_M$ can be neglected. It then follows from equation C-29 and inverse Fourier integral representation of $\underline{\mathscr{P}}(\underline{\kappa}, z)$ that

$$\underline{E}_s(\underline{r}) = \frac{z}{(2\pi)^2} \int_0^1 d\eta \int d\underline{\kappa}_s \, e^{i\underline{\kappa}_s \cdot \underline{\rho}} \, e^{-i\eta z(K_{sz} - K_M + \zeta \kappa_{sx})}$$

$$\times \int d\underline{\rho}' \, \underline{\gamma} : \underline{P}(\underline{r}') \, e^{-i\underline{\kappa}_s \cdot \underline{\rho}'} \tag{C-30}$$

The integration over $\underline{\kappa}_s$ gives the factor

$$(2\pi)^2 \, \delta(x - x' - \eta \zeta z) \, \delta(y - y')$$

The integration over $\underline{\rho}'$ gives

$$\underline{E}_s(\underline{r}) = z \int_0^1 d\xi \, e^{-i\eta K_M z} \, \underline{\gamma} : \underline{P}(x - \eta\zeta z, y, z) \tag{C-31}$$

Then the field at the exit surface of the nonlinear crystal ($z = D$) can be written

$$\underline{E}_s(\underline{\rho}, D) = D \int_0^1 d\eta \, e^{-i\eta K_M D} \, \underline{\gamma} : \underline{P}(x - \eta\zeta D, y, D) \tag{C-32}$$

If we let $(1 - \eta) D = z$ and make z as a dummy variable of integration, equation C-32 becomes

$$\underline{E}_s(\underline{\rho}, D) = e^{-iK_M D} \int_0^D dz \, e^{iK_M z} \, \underline{\gamma} : \underline{P}(x - \zeta D + \zeta z, y, D) \tag{C-33}$$

This expression shows that the resultant sum-frequency field is produced by constructive interference of the waves radiated from each differential slab of polarization in the material. It is this concept that was used in the geometric optics theory. Double refraction (or anisotropy effect) of the sum-frequency electric field in included in equation C-33 through the parameter $(x - \zeta D + \zeta z)$. Now refer to Figure C-3 the line at angle ζ, which is normal to the tangential plane to the wave vector surface, represents the direction of energy flow of the sum-frequency field[21]. It is intuitive to expect that the path of integration to obtain resultant field should be along the energy flow direction rather than the z direction. To understand the implication of
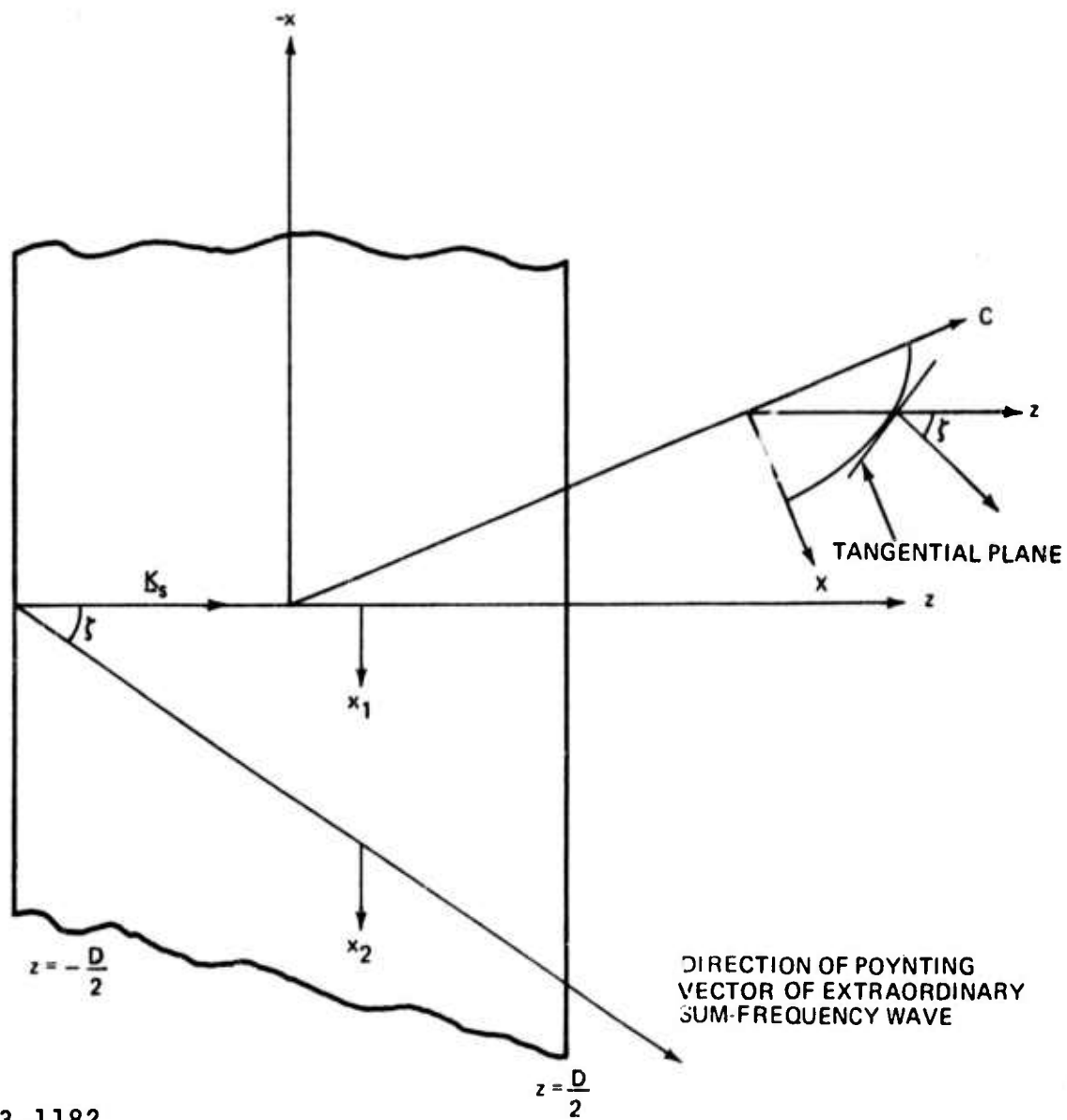
3-1182

FIGURE C-3. ILLUSTRATION OF DOUBLE REFRACTION OF SUM-
FREQUENCY WAVE

the parameter $x - \zeta D + \zeta z$, let us denote points in the polarization wave, the source points, by (x_1, y_1, z_1), and points in the sum-frequency wave, the observer points, by (x_2, y_2, z_2). We regard equation C-33 an an integral over source points giving the sum-frequency field at an observer point. We shall measure the source points from the coordinate origin. We define x_2 for the observer points in such a way that $x_2 = 0$, $y_2 = 0$ lies on the line making angle ζ with the z axis. Then $x_2 - \zeta z_2$ and the path of integration over the source points is specified by $x_1 = x_2 + \zeta z_1$, $y_1 = y_2 = y$, with x_2 hold constant in the integration since it refers to the observation point. Then when we set $z_2 = D$, we obtain the integration parameter $x_1 = x - \zeta D + \zeta z$. This can be interpreted that the sum-frequency field at the points (x, y, D) is obtained by integration along the energy flow line.

The angular spectrum of the sum-frequency field at the exit surface of the crystal is simply

$$\underline{\mathcal{E}}_s(\underline{\kappa}_s, D) = D\, e^{-i\frac{\Delta K D}{2}}\; \underline{\underline{\gamma}} : \underline{\varphi}(\underline{\kappa}_s, D)\; \frac{\sin\left(\frac{\Delta K D}{2}\right)}{\left(\frac{\Delta K D}{2}\right)} \qquad (C\text{-}34)$$

where

$$\Delta K = K_{sz} - K_n - \zeta \kappa_{sx} + \frac{\kappa_s^2}{2K_M} \qquad C\text{-}35)$$

Equation C-34 indicates that the angular spectrum at the exit surface is not a summation over the contributions of the Fourier components of the polarization in the differential slab.

3. FOURIER SPACE CONFIGURATION (TYPE III) SYSTEM

a. POINT SPREAD FUNCTIONS AND OPTICAL TRANSFER FUNCTION OF A PLANE WAVE PUMPED INFINITE APERTURE FOURIER CONFIGURATION SYSTEM

Diffraction due to apertures is neglected in this discussion in order to separate image properties of the upconversion process from the diffraction. Lens apertures (the nonlinear material aperture) and the pump beam diameter are, therefore, assumed to be infinitely large.

A simplified schematic of a Fourier space configuration upconverter system is shown in Figure C-4. Lens L_1 is positioned such that the object and the front surface of the nonlinear material are respectively in the front and back focal planes. The front local plane of lens L_2 coincide with the exit surface of the nonlinear crystal. Upconverted real image then forms in the back focal plane of lens L_2. Lenses L_1 and L_2 therefore, form a Fourier transform pair. The upconversion takes place in the Fourier transformed space of the object waves; thus the name Fourier space configuration system.

For the plane wave pumped upconverter, it can be shown that the angular spectrum of upconverted image fields in air beyond the non-linear crystal ($z \geq + D/2$) is related to the Fourier component of object fields over the front surface of the crystal by

$$\mathcal{E}_s(\underline{\kappa}_s, z) \sim \mathcal{E}_i(\underline{\kappa}_s, -D/2) \, \text{Sinc}\left(\frac{\Delta KD}{2}\right) e^{-i \, \Delta KD/2}$$

$$e^{i\left[K_{sz} D + K_{saz}(z - D/2)\right]}$$

(C-36)

OBJECT   L₁   NONLINEAR CRYSTAL   L₂   UPCONVERTED IMAGE
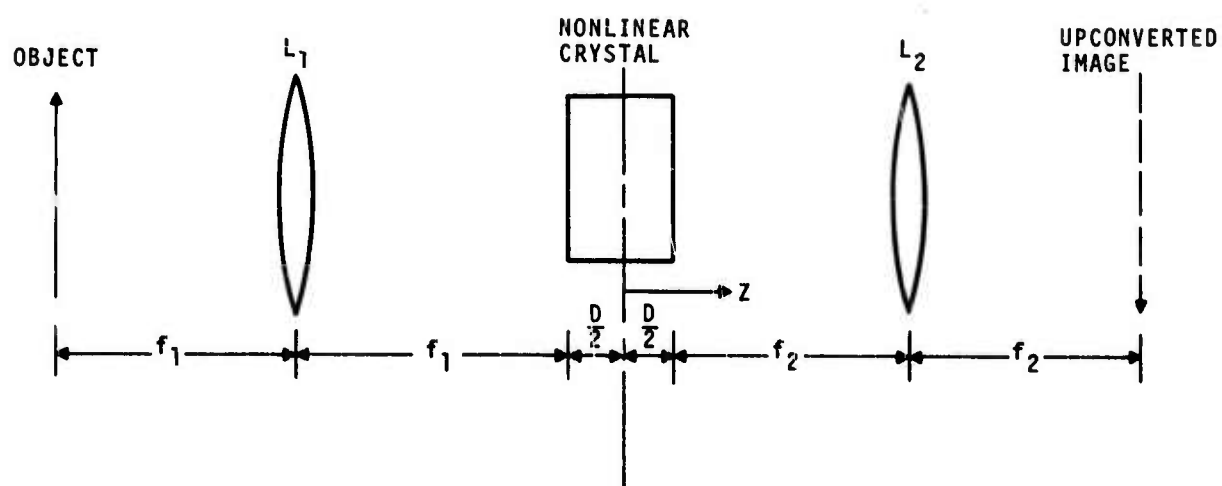
2-4814

FIGURE C-4. IMAGE UPCONVERTER ARRANGED IN FOURIER SPACE CONFIGURATION

where

$$\text{Sinc } x = (\sin x)/x$$

D : material thickness

$$K_{sz} = \left(K_s^2 - \underline{\kappa}_s^2 \right)^{1/2} : \text{ z component of wave vector at } \lambda_s \text{ in the material}$$

K_{saz} : z component of wave vector at λ_s in air

$$\Delta K \left(= K_{sz} - K_M - \zeta \, \kappa_{sx} + \frac{\kappa_s^2}{2K_M} \right) : \text{ phase mismatch factor}$$

K_M : wave vector at λ_s along the phase matched direction

ζ : anisotropy angle

The angular spectrum $\mathcal{E}_i (\underline{\kappa} , - D/2)$ is a Fourier transform of the object field distribution over the plane $z = -D/2$. The object field distribution in the plane $z = -D/2$ is a Fourier transform of the object field distribution over the front focal plane of lens L_1 since the plane $z = -D/2$ coincides with the back focal plane of lens L_1[14].

$$E_i \, (\underline{\rho}, \, -D/2) = \frac{-i}{\lambda_i} \int E_i \, (\underline{\rho}_i, \, -2f_1 - D/2) \, e^{-i \frac{K_{ia}}{f_1} \left(\underline{\rho} \cdot \underline{\rho}_i \right)} \, d\underline{\rho}_i \quad (C\text{-}37)$$

and

$$\mathcal{E}_i \, (\underline{\kappa}, \, - D/2) = \frac{1}{(2\pi)^2} \int E_i \, (\underline{\rho}, \, - D/2) \, e^{-i \, \underline{\kappa} \cdot \underline{\rho}} \, d\underline{\rho} \quad (C\text{-}38)$$

where

f_1 = focal length of lens L_1

$\underline{\rho}_i$ = transverse position in the front focal plane of lens L_1

$\underline{\rho}$ = transverse position in the back focal plane $(z = -D/2)$ of lens L_1

Substituting Equation (2) into Equation (3) and carrying out the integration we obtain

$$\mathcal{E}_i\,(\,\underline{\kappa},\,-D/2) \sim E_i\,(-f_1\,/K_{ia},\,-2f_1 - D/2) \qquad \text{(C-39)}$$

Constant Amplitude factor and fixed phase factors have been omitted in equation C-39 since they do not affect the result in any significant way. Equation C-39 indicates that the angular spectrum of field distribution over the back focal plane of a nondiffracting thin lens has the same functional form as the field distribution over the front focal plane of the lens. This result is no surprise if one realizes that they are related by double Fourier transform.

The field distribution of an upconverted image formed in the back focal plane of lens L_2 has the same functional form as $\mathcal{E}_s\,(\,\underline{\kappa}_s,\,-D/2)$ since the plane $z = +D/2$ and the upconverted image plane are two focal planes of lens L_2.

$$E_s(\underline{\rho}_s, 2f_2 + D/2) \sim \mathcal{E}_s(K_{sa}\,\rho_s/f_2,\ D/2) \tag{C-40}$$

Combining equations C-36, C-39, and C-40, we obtain an expression for the upconverted image field distribution

$$E_s(\underline{\rho}_s,\ 2f_2 + D/2) \sim E_i\left(-\frac{K_{sa}\,f_1}{K_{ia}\,f_2}\,\underline{\rho}i,\ -2f_1 - D/2\right).$$

$$\text{Sinc}\left(\frac{\Delta KD}{2}\right)e^{-i\left(\frac{\Delta KD}{2} - K_{sz}\,D\right)} \tag{C-41}$$

where mismatch factor ΔK and the z component wave vector K_{sz} in equation C-41 are evaluated by replacing $\underline{\kappa}_s$ with $K_{sa}\underline{\rho}_s/f_2$ and are given by

$$\Delta K = K_s - K_M - \zeta K_{sa}\,x_s/f_2 + \frac{K_{sa}^2}{2f_2^2}\,\rho_s^2\left(\frac{1}{K_M} - \frac{1}{K_s}\right) \tag{C-42}$$

and

$$K_{sz}^2 = K_s^2 - (K_{sa}\,\rho/f_2)^2 \tag{C-43}$$

If crystal anisotropy is neglected the mismatch factor ΔK is

$$\Delta K = -\frac{K_p}{2K_M K_i}\left(\frac{K_{sa}}{f_2} - \rho_s\right)^2 \tag{C-44}$$

The function sinc $\left[\dfrac{K_p D}{4K_M K_i}\left(\dfrac{K_{sa}}{f_2}\,\rho_s\right)^2\right]$ indicates that the amplitude of an upconverted image field of a uniformly illuminated object field will not be uniform but will decrease with transverse distance ρ_s. It imposes a limitation on the size of the upconverted image but will not limit the image

resolution. If we define the size of an upconverted image as equal to the transverse distance ρ_s, where the first zero of a sinc x function occurs, the radius of an upconverted image is expressed by

$$a_s = 2 \frac{f_2}{K_{sa}} \sqrt{\frac{\pi \ K_M K_i}{D \ K_p}} \qquad \text{(C-45)}$$

Equation C-41 also shows that the transverse magnification of a Fourier space configuration upconverter system is

$$M_t = - \frac{K_{ia} \ f_2}{K_{sa} \ f_1} = - \frac{\lambda_s \ f_2}{\lambda_i \ f_1} \qquad \text{(C-46)}$$

Equation C-46 can also be obtained by the geometric optics analysis. The limiting size of an object that can be upconverted can be easily found by combining equations C-45 and C-46.

$$a_i = a_s / \left| M_t \right| = 2 \ \frac{f_1}{K_{ia}} \sqrt{\frac{\pi K_M K_i}{DK_p}} \qquad \text{(C-47)}$$

Noting that the object size a_i is related to the acceptance angle θ_{ia} (FOV) of the upconverter by

$$2a_i = f_1 \ \theta_{ia}$$

we obtain

$$\theta_{ia} = 2 \ \left(\frac{2 \lambda_p \lambda_i \ n_i \ n_{sM}}{\lambda_s \ n_p \ D} \right)^{1/2} \qquad \text{(C-48)}$$

For a noncritically phased matched proustite unconversion from 10.6 μm to 0.967 μm, we have $\theta_{ia} = 0.157 \left(\dfrac{1}{D} \right)^{1/2}$ rad.

To illustrate the points presented in the previous discussion let us consider a case where the object field distribution is a sine function as shown in Figure C-5A. The field distribution of upconverted image formed in the back focal plane of lens L_2 is shown in Figure C-5B. The period of the sine function image field is magnified by a factor M_t and its amplitude envelope follows the sinc function. The image is inverted as shown in Figure C-5B so that an object point $-y_{i1}$ is imaged at $y_{s1} = -M_t \, y_{i1}$. The resolving power is unlimited since the image field period is linearly proportional to the object field period. The object size that can be upconverted is, however, limited. The size limitation is caused by the phase match requirement rather than the crystal aperture limitation.

The point spread function, which is a response to a point object, is easily obtained from equation C-41. The field distribution of a point object at (x_{io}, y_{io}) is expressed

$$E_i \, (\underline{\rho}_i) \sim \delta \, (x_i - x_{io}) \cdot \delta (v_i - y_{io})$$

Then from equation C-41, the point spread function becomes

$$H_s \, (\underline{\rho}_s) \sim \delta \, (x_s/M_t - x_{io}) \, \delta (y_s/M_t - y_{io}) \left[\text{Sinc}\left(\frac{\Delta KD}{2}\right) \cdot e^{-i \, (\Delta K/2 - K_{sz}) \, D} \right]_{\underline{\kappa} = K_{sa} \, M_t \, \rho_{io} /f_2} \quad \text{(C-49)}$$

C-24
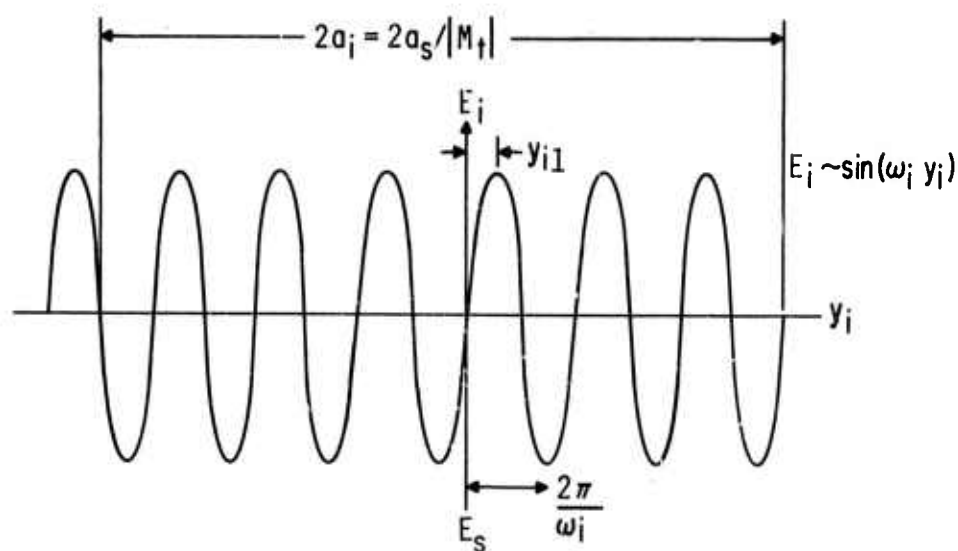
A. OBJECT FIELD DISTRIBUTION
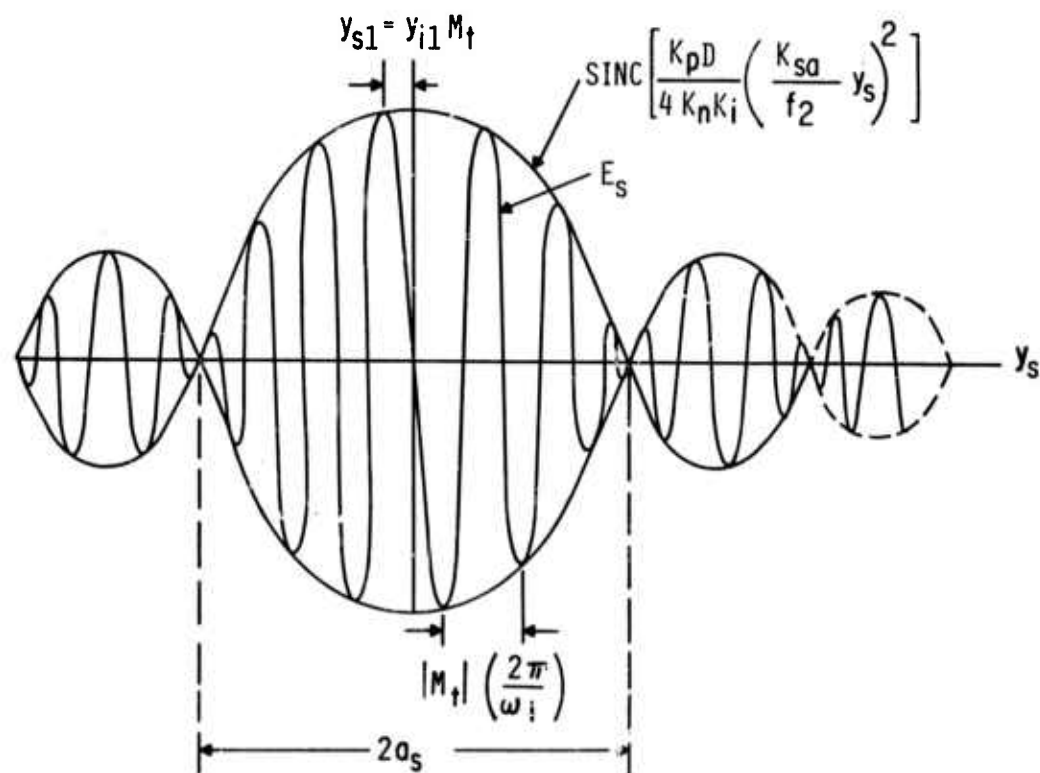
B. UPCONVERTED IMAGE FIELD DISTRIBUTION

V73-672
2-4815

FIGURE C-5. FIELD DISTRIBUTION OF OBJECT UPCONVERTED IMAGE
FOR THE FOURIER SPACE CONFIGURATION

where $\left[\quad \right]_{\underline{\kappa}} = K_{sa}\underline{\rho}_s / f_2$ indicates that the quantity inside the bracket is evaluated at $\underline{\kappa} = K_{sa}\underline{\rho}_s / f_2$ as shown in equations C-42 and C-43.

The coherent transfer function, which is the Fourier transform of the point spread function, becomes

$$h_s(\underline{\kappa}_s) \sim M_t^2 \, e^{-i M_t \underline{\kappa}_s \cdot \underline{\rho}_{io}} \left[\text{Sinc}\left(\frac{\Delta KD}{2}\right) \cdot e^{-i\left(\frac{\Delta K}{2} - K_{sz}\right)D} \right]_{\underline{\kappa} = K_{sa} M_t \underline{\rho}_{io} / f_2}$$

(C-50)

Amplitude of $h_s(\underline{\kappa}_s)$ depends on the object location and thus object size limitation is implied even for the infinite aperture Fourier configuration upconverter. The optical transfer function, which is defined[14] as,

$$\mathcal{H}_s(\underline{\kappa}) = \frac{\iint h_s(\underline{\kappa}') \cdot h_s^*(\underline{\kappa}' + \underline{\kappa}) \, d\underline{}'}{\iint h_s(\underline{\kappa}')^2 \, d\underline{\kappa}'}$$

(C-51)

becomes

$$\mathcal{H}_s(\underline{\kappa}) = e^{i M_t \underline{\kappa} \cdot \underline{\rho}_{io}}$$

(C-52)

Equation C-52 again indicates the property of unlimited resolving power since the amplitude of optical transfer function (Modulation transfer function) is independent of angular frequency $\underline{\kappa}$.

b. POINT SPREAD FUNCTION OF A GAUSSIAN BEAM PUMPED FOURIER SPACE CONFIGURATION SYSTEM

The effect of pump beam amplitude distribution on the imaging characteristics of the Fourier space configuration image upconverter is considered. Diffraction due to the lens apertures and the crystal birefringence are neglected. It is also assumed that the physical size of the nonlinear material is large compared to the pump beam size. The optical arrangement is shown in Figure C-4.

The pump beam is assumed to be in the TEM_{00} mode. The Gaussian window at the entrance surface of the nonlinear crystal is expressed by*

$$E_p(\underline{\rho}, -D/2) \sim e^{-\underline{\rho}^2/a^2} \tag{C-53}$$

The angular spectrum of pump field distribution is

$$\mathcal{E}_p(\underline{\kappa}_p, -D/2) \sim e^{-a^2 \underline{\kappa}_p^2/4} \tag{C-54}$$

The point object in the front focal plane of the object lens is expressed by

$$E_i(\underline{\rho}_i, -2f_1-D/2) \sim \delta(\underline{\rho}_i - \underline{\rho}_{io}) \tag{C-55}$$

---

*Constant amplitude and phase factors are again omitted in the following analysis.

The angular spectrum in the IR object fields in the entrance plane of the crystal is, using equation C-39

$$\mathcal{E}_i(\,\underline{\kappa}_i,\,-D/2) \sim E_i(-\,f_1\,\underline{\kappa}_i/K_{ia},\,-2f_1 - D/2) \sim \delta(\,\underline{\kappa}_i + K_{ia}\underline{\rho}_{io}/f_1) \quad \text{(C-56)}$$

The sum-frequency polarization P_s is obtained by taking a convolution of $\mathcal{E}_i(\,\underline{\kappa}_i,\,-D/2)$ and $\mathcal{E}_p(\,\underline{\kappa}_p,\,-D/2)$.

$$P_s(\,\underline{\kappa}_s,\,-D/2) \sim \int \mathcal{E}_i(\,\underline{\kappa}_i,\,-D/2)\,\mathcal{E}_p(\,\underline{\kappa}_s - \underline{\kappa}_p,\,-D/2)\,d\underline{\kappa}_i$$

$$\sim e^{-a^2(\,\underline{\kappa}_s + K_{ia}\underline{\rho}_{io}/f_1)^2/4} \quad \text{(C-57)}$$

The angular spectrum of upconverted image fields at the exit surface of the crystal is

$$\mathcal{E}_s(\,\underline{\kappa}_s,\,+D/2) \sim e^{-a^2(\,\underline{\kappa}_s + K_{ia}\underline{\rho}_{io}/f_1)^2/4}\ \text{Sinc}\left(\frac{\Delta KD}{2}\right)e^{-iD\left(K_{sz} + \frac{\Delta K}{2}\right)} \quad \text{(C-58)}$$

where ΔK and K_{sz} are mismatch factors and the z component of wave vector in the material for the angular spectrum with the angular frequency $\underline{\kappa}_s$.

Field distribution of the upconverted image in the back focal plane of the imaging lens is, by equation C-40

$$E_s(\underline{\rho}_s,\,2f_2 + D/2) \sim \mathcal{E}_s(K_{sa}\underline{\rho}_s/f_2,\,+D/2)$$

C-28

$$
\sim e^{-a^2 \left(\frac{K_{sa}}{f_2} \underline{\rho}_s + \frac{K_{ia}}{f_1} \underline{\rho}_{io} \right)^2 \Big/ 4} \left[\text{Sinc} \left(\frac{\Delta \underline{K} D}{2} \right) e^{-i D (K_{sz} + \Delta K/2)} \right]_{\underline{\kappa}_s = \frac{K_{sa}}{f_2} \underline{\rho}_s} \tag{C-59}
$$

The symbol $\left[\right]_{\underline{\kappa}_s = \frac{K_{sa}}{f_2} \underline{\rho}_s}$ indicates again that ΔK and K_{sz} are

evaluated by replacing $\underline{\kappa}_s$ with $K_{sa} \underline{\rho}_s / f_2$ as shown in equations C-42 and C-43.

Equation C-59 is the point spread function of Gaussian beam pumped Fourier space configuration image upconverter. The upconverted image is no longer a point. The sinc function again limits the FOV of the system and describes the amplitude envelope of the image plane in the similar way as the plane wave pumped case. The Gaussian amplitude factor

$$
e^{-\left(\frac{a K_{ia}}{2 f_1} \right)^2 \left(\frac{f_1 K_{sa}}{f_2 K_{ia}} \underline{\rho}_s + \underline{\rho}_{io} \right)^2}
$$

indicates that transverse magnification factor M_t and the image spot size are given by

$$
M_t = \underline{\rho}_s \Big/ \underline{\rho}_i = - f_2 K_{ia} \Big/ f_1 K_{sa} \tag{C-60}
$$

$$
W_s = 2 f_2 \Big/ a K_{sa} \tag{C-61}
$$

Equation C-60 is identical to equation C-46. It implies that the Gaussian amplitude distribution does not introduce distortion. Combining equations

C-60 and C-61 and dividing the object spot size by the focal length of the object lens we obtain expressions for the resolvable IR object spot size and angle;

$$W_i = \lambda_i f_1 / \pi a \qquad (C\text{-}62)$$

$$\gamma_i = \lambda_i / \pi a \qquad (C\text{-}63)$$

Since Rayleigh resolution criteria cannot be applied to the present case, the 1/e amplitude is arbitrarily chosen as the resolution limit.

From above discussion one may conclude:

- FOV and the intensity envelope of image plane may not be affected by the pump beam intensity distribution.

- The optical transfer function of the Fourier space configuration system depends heavily on the pump beam intensity distribution. A multimode pump beam (diverging pump beam), therefore, degrades resolution of the Fourier space configuration upconverter.

4.   IMAGE UPCONVERSION IN IMAGE SPACE

Image upconversion with Type II optical system (Figure C-6) is considered first before analyzing Type I system. As shown in Figure C-6, the Type II system does not use an IR objective lens. For a distant IR object,
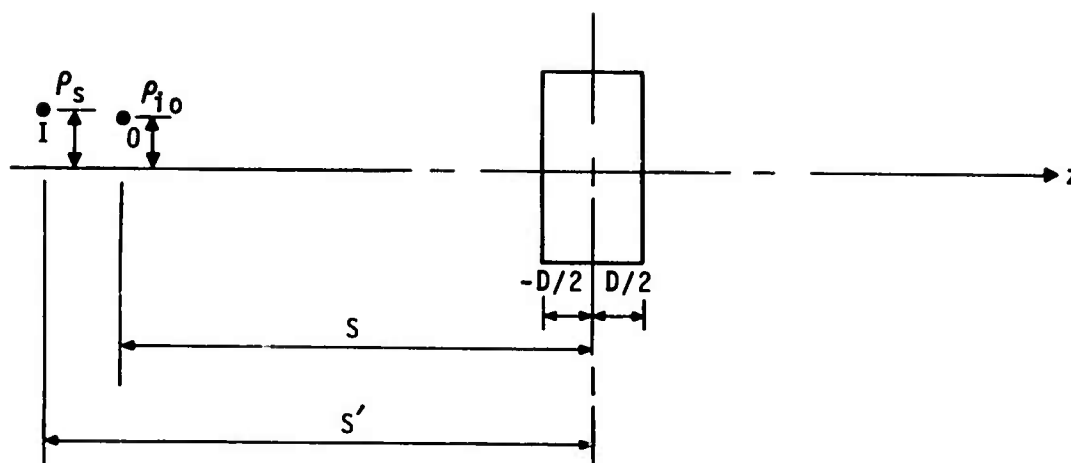
3-1154

FIGURE C-6.   TYPE II OPTICAL SYSTEM

this optical system is very similar to the Type III system. Diffraction
due to the crystal and other apertures and material birefringence are ignored
in the following discussion.

The pump beam intensity distribution at the crystal surface is
assumed to be Gaussian

$$E_p(\underline{\rho}, -D/2) = E_p \, e^{-\rho^2/w_p^2}$$

(C-64)

Its angular spectrum is expressed by

$$\mathcal{E}_p(\underline{\kappa}_p, -D/2) = \frac{E_p \, w_p^2}{4\pi} \, e^{-w_p^2 \kappa_p^2/4}$$

(C-65)

If the angular spectrum of IR object field on the front surface of crystal is
denoted by $\mathcal{E}_i(\underline{\kappa}_i, -D/2)$, the angular spectrum of the sum-frequency field
in the space $z > D/2$ is given, by equations C-21 and C-22,

$$\mathcal{E}_s(\underline{\kappa}_s, z) = \frac{i\,\omega_s\,E_p\,w_p^2\,t_s t_p t_i \chi D}{2\,C n_s} \, e^{i D(K_{sz} - \Delta K/2)} \, \text{Sinc}\left(\frac{\Delta KD}{2}\right) \cdot$$

(C-66)

$$\exp\left[i\,K_{saz}(z - D/2)\right] \int d\underline{\kappa}' \, \mathcal{E}_i(\underline{\kappa}' - D/2) \exp\left[-w_p^2(\underline{\kappa}_s - \underline{\kappa}')^2/4\right]$$

where:

t_s, t_p, t_i = transmittance at the crystal surface for λ_s, λ_p, and λ_i,
respectively

Sinc $X = (\text{Sin } X)/X$

D = material thickness

K_{sz} = z component of wave vector at λ_s in the material

K_{saz} = z component of wave vector at λ_s in air

$$\Delta K = \left(K_{sz} - K_m - \zeta \kappa_{sx} + \frac{\kappa_s^2}{2K_M} \right) : \text{phase mismatch factor}$$

K_M = wave vector at λ_s in the material along the phase-match direction

ζ = anisotropy angle

χ = nonlinear susceptibility

If a point IR object located at a point $(\underline{\rho}_{io}, -s)$ is expressed by

$$E_i(\underline{\rho}_i, -s) = E_i \, \delta(\underline{\rho}_i - \underline{\rho}_{io}) \tag{C-67}$$

its angular spectrum at $z = -D/2$ (that is, on the crystal front surface) is expressed by

$$\mathcal{E}_i(\underline{\kappa}_i, -D/2) = \frac{E_i}{(2\pi)^2} \exp i \left[\underline{K}_{ia}(s-D/2) - (\underline{K}_i \cdot \underline{\rho}_{io} + \alpha \underline{\kappa}_i^2) \right] \tag{C-68}$$

where

$\underline{K}_{ia}$ = wave vector at λ_i in air

$\alpha = (s - D/2)/2 \, K_{ia}$

Substituting equation C-68 into equation C-66 and carrying out integration, we obtain for $z > D/2$

$$\mathcal{E}_s (\underline{\kappa}_s, \ z) = i \frac{\omega_s E_i E_p w_p^2 t_p t_i t_s \chi D}{2\pi Cn_s (w_p^2 + i4\alpha)} \text{Sinc}\left(\frac{\Delta KD}{2}\right) \exp\left[i \overline{\emptyset}(\underline{\kappa}_s, \ z)\right] \cdot$$

$$\exp\left[\frac{-(\underline{\rho}_{io} - 2\alpha\underline{\kappa}_s)^2}{w_p^2 + i4\alpha} - i(\underline{\rho}_{io} + \alpha\underline{\kappa}_s)\cdot\underline{\kappa}_s\right]$$

(C-69)

where the phase factor is expressed by,

$$\overline{\emptyset}(\underline{\kappa}_s, \ z) = \left[K_{sa}(z - D/2) + K_{ia}(s - D/2) + D(K_s + K_M)/2\right] + \frac{\zeta D}{2}\kappa_{sx}$$

$$- \frac{\zeta_s^2}{2}\left[\frac{z - D/2}{K_{sa}} + \frac{s - D/2}{K_{ia}} + \frac{D}{2}\left(\frac{1}{K_M} + \frac{1}{K_s}\right)\right]$$

(C-70)

The quantity within the first bracket of equation C-70 is independent of $\underline{\kappa}_s$ and represents a constant phase shift for all angular spectra. The factor $\left(\frac{\zeta D}{2}\kappa_{sx}\right)$ arises from the crystal birefringence. Its effect on the imaging properties will be discussed in detail later, but it will be ignored for the present discussion. The stationary phase condition that is required for the reproduction of clear image, the phase factor, requires that $\overline{\emptyset}$ should be independent of spatial angular frequency. This condition is used to determine

the relationship between two conjugate planes. Equating the coefficient of κ_s^2 to zero, we can solve for the image plane distance

$$z = -s' = -\frac{K_{sa}}{K_{ia}}\, s - \frac{DK_{sa}}{2}\left(\frac{1}{K_M} + \frac{1}{K_s} - \frac{1}{K_{ia}} - \frac{1}{K_{sa}}\right) \qquad (C\text{-}71)$$

The angular spectrum of virtual upconverted image field is now given ignoring a constant phase factor by

$$\mathscr{E}_s(\underline{\kappa}_s,\, -s') = i\,\frac{\omega_s E_i E_p w_p^2 t_p t_i t_s\ \chi D}{2\pi C n_s (w_p^2 + i\,4\,\alpha)}\ \mathrm{Sinc}\left(\frac{\Delta KD}{2}\right)\exp\left[-\frac{\left(\underline{\rho}_{io} - 2\alpha\underline{\kappa}_s\right)^2}{w_p^2 + i\,4\,\alpha}\right]\cdot$$

$$(C\text{-}72)$$

$$\exp\left[-i\left(\underline{\rho}_{io} + \alpha\,\underline{\kappa}_s\right)\cdot\underline{\kappa}_s\right]$$

The exponential decaying factor in equation C-72 is resulted from the Gaussian window due to the pump beam intensity distribution. The exponential decaying function becomes unity if the pump beam is infinitely large ($w_p = \infty$) that is, plane wave pump. The exponential phase function arises from the off-axis object location.

The point spread function of the virtual upconverted image is obtained, for negligible birefringence, by using a relation

$$\Delta K \approx \frac{K_p D}{2K_M K_i}\,\kappa_s^2$$

and taking a Fourier transform of equation C-72

$$E_s(\underline{\rho}_s, -s') = \mathcal{E}_s \exp\left[\frac{-\rho_{io}^2}{w_p^2 + i4\alpha}\right] \int d\underline{\kappa} \; \text{Sinc}\left(\frac{K_p D\kappa^2}{4 K_M K_i}\right) \cdot$$

(C-73)

$$\exp\left[\frac{4\alpha \, \underline{\rho}_{io} \cdot \underline{\kappa} - 4\alpha^2 \kappa^2}{w_p^2 + i4\alpha} + i(\underline{\rho}_s - \underline{\rho}_{io}) \cdot \underline{\kappa}\right]$$

where

$$\mathcal{E}_s = i \frac{\omega_s E_p E_i w_p^2 t_p t_i t_s \, \chi D}{2\pi C n_s (w_p^2 + i4\alpha)}$$

The point spread function of Type I system can easily be obtained from equation C-73 by equating α to zero. This can be understood if one realizes the geometry of the Type I system. In the Type I system, the objective telescope is used to obtain a real IR image of the object in the plain containing the pump window. The factor α is equal to zero since $s = D/2$ for Type I arrangement.

The point spread function of Type I system is, therefore, after the integration,

$$E_s(\underline{\rho}_s, -s') = \frac{i2\omega_s E_i E_p t_p t_i t_s \, \chi K_s K_i}{C n_s K_p} \exp(-\rho_{io}^2/w_p^2) \cdot$$

C-74)

$$\left\{\frac{\pi}{2} - \text{Si}\left[\frac{K_M K_i}{DK_p}(\rho_s - \rho_{io})^2\right]\right\}$$

The exponential decay factor is a Gaussian and describes the envelope of upconverted image field amplitude distribution. The sine-integral function describes the image-object relations. It is obvious from equation C-74 that the upconversion transverse magnification is unity for Type I system. Taking the first root of sine-integral function as the limiting resolution, we obtain an expression for the linear resolution for Type I system.

$$ r = \left(2 \frac{K_p D}{K_M K_i} \right)^{1/2} = \left(\frac{\lambda_s \lambda_i n_p D}{\pi n_s n_i \lambda_p} \right)^{1/2} \tag{C-75} $$

5. PARAMETRIC IMAGE UPCONVERSION WITH A MULTIMODE LASER PUMP

Parametric image upconversion pumped by plane waves and Gaussian beams have been considered in proceeding sections. It was shown that diffraction-limited resolution can be obtained under certain conditions. To make full use of the available pump laser power, it would be necessary to operate a pump laser in multimode pattern. The imaging properties of a Type II system using a multimode pump laser are considered first in this section.

The spatial frequency response (angular spectrum) of the up-converted image field is considered for two cases. In the first upconverter system, the nonlinear material is pumped by the near field of a TEM_{01} mode laser beam. The crystal in the second system is placed in the near field of a toroidal mode beam. The shape of the spatial frequency response resembles, as expected, that of pump field distribution. The result suggests possible spatial filtering technique for the upconversion system. Quantitative evaluation of the field distribution of upconverted image was the attempted at this time since it requires an extensive electronic computer effort. Imaging properties of the Type I and III systems pumped with a TEM_{01} mode and a troidal mode pump beam are then considered qualitatively.

Consider first the case of a TEM_{01} mode pump laser beam. Assume that the material is placed in the near field (the waist) of the beam. The field distribution of the pump beam can be considered as an optical window for IR object waves. The near-field distribution of a TEM_{01} mode beam is expressed, in a cylindrical coordinate system as,

$$E_{01}(\rho) = \left(1 - 2\,\frac{\rho^2}{a^2}\right)\,\exp\left(\frac{-\rho^2}{a^2}\right) \tag{C-76}$$

where

ρ = radial coordinate

a = beam radius of fundamental mode

Unity amplitude is assumed in equation C-76 for simplicity. The angular spectrum of a TEM_{01} field distribution is the Hankel transform of field distribution given by equation C-76,

$$\mathcal{G}_{01}(\kappa) \sim \int_0^\infty \left(1 - 2\,\frac{\rho^2}{a^2}\right)\,\exp\left(\frac{-\rho^2}{a^2}\right)\,J_0(\kappa\rho)\,\rho\,d\rho \tag{C-77}$$

It can be shown that $\mathcal{G}_{01}(\kappa)$, neglecting a constant multiplicative factor, becomes

$$\mathcal{G}_{01} \sim \frac{a^2}{2}\left(\frac{a^2\kappa^2}{2} - 1\right)\,\exp\left(\frac{-a^2\kappa^2}{4}\right) \tag{C-78}$$

Neglecting double refraction effects and following the procedure developed previously, it can be shown that the equation relating the image position and the object position is identical to that of Gaussian beam pumped case. The angular spectrum of upconverted field distribution over the image plane for an on-axis point object, again neglecting constant multiplicative factors, is given by:

$$\mathcal{E}_s(\kappa_s, s') \sim \frac{\sin(\Delta\kappa D/2)}{(\Delta\kappa D/2)} \int \frac{a^2}{2} \left(\frac{a^2 \kappa^2}{2} - 1 \right) \exp\left[-\left(\frac{a^2}{4} + i\frac{\alpha}{2} \right) \kappa^2 \right] \cdot \quad \text{(C-79)}$$

$$\exp\left[-i\alpha \, \underline{\kappa}_s \cdot \underline{\kappa} \right] d\underline{\kappa}$$

where

$$\alpha = \lambda_i (s - D/2)/2\pi$$

The $(\sin x/x)$ function arises again from phase mismatch for a given angular spectrum. The attenuation factor expressed by the integration in equation C-79 is due to the transverse mode structure of the pump laser beam. The attenuation factor,

$$I_{01} = \frac{a^2}{2} \int \left(\frac{a^2 \kappa^2}{2} - 1 \right) \exp\left[-\left(\frac{a^2}{4} + i\frac{\alpha}{2} \right) \kappa^2 \right] \exp\left[-i\alpha \, \underline{\kappa}_s \cdot \underline{\kappa} \right] d\underline{\kappa}$$

can be rewritten as Hankel transform,

$$I_{01} = \frac{a^2}{2} \int \left(\frac{a^2 \kappa^2}{2} - 1 \right) \exp\left[-\left(\frac{a^2}{4} + i \frac{\alpha}{2} \right) \kappa^2 \right] J_0 (\alpha \kappa_s \kappa) \kappa d\kappa$$

Evaluating the integration, we obtain

$$I_{01} = a^2 \frac{\exp\left(-\frac{\alpha^2 \kappa_s^2}{a^2 + i2\alpha} \right)}{(a^2 + i2\alpha)^3} \left(a^4 + 4\alpha^2 - 2\alpha^2 a^2 \kappa_s^2 \right) \qquad \text{(C-80)}$$

If the condition $a^2 \gg 2\alpha$ is satisfied, equation 80 becomes:

$$I_{01} = \left(1 - 2 \frac{\alpha^2}{a^2} \kappa_s^2 \right) \exp\left(-\alpha^2 \kappa_s^2 / a^2 \right) \qquad \text{(C-81)}$$

Equations C-80 and C-81 indicate that the image spectrum at high spatial fre-
quencies of the TEM_{01} beam pumped image upconverter system is attenuated
more than that of Gaussian beam pumped system.

We consider, next, an upconverter system pumped by a toroidal
mode laser beam. The toroidal mode, the simplest multimode distribution,
considered here is produced by subtracting equal amplitude TEM_{01} mode field
from TEM_{00} mode field. The near-field distribution of this mode is expressed
by:

$$E_p (\rho) = E_{00} (\rho) - E_{01} (\rho) = 2 \frac{\rho^2}{a^2} \exp\left(\frac{-\rho^2}{a^2} \right) \qquad \text{(C-82)}$$

The angular spectrum of the toroidal field distribution is:

$$\mathcal{E}_p{}^{(\kappa)} \sim a^2 \left(1 - \frac{a^2 \kappa^2}{4}\right) \exp\left(\frac{-a^2 \kappa^2}{4}\right) \qquad \text{(C-83)}$$

It can be shown that the mode attenuation factor for the angular spectrum of the upconverted image field produced by this system is

$$I_d = \frac{2a^2}{(a^2 + 12\alpha)^3} \left[a^2 \alpha^2 \kappa_s^2 + 12\alpha (a^2 + 12\alpha)\right] \exp\left[\frac{-\alpha^2 \kappa_s^2}{(a^2 + 12\alpha)}\right] \qquad \text{(C-84)}$$

Again for the condition $a^2 \gg 2\alpha$, the attenuation factor I_d approaches

$$I_d \sim \left(\frac{\alpha^2}{a^2} \kappa_s^2 + i \frac{4\alpha}{a^2}\right) \exp\left(\frac{-\alpha^2 \kappa_s^2}{a^2}\right) \qquad \text{(C-85)}$$

For $\kappa_s^2 \gg |4/\alpha|$,

$$I_d \sim \frac{\alpha^2}{a^2} \kappa_s^2 \exp\left(\frac{-\alpha^2 \kappa_s^2}{a^2}\right) \qquad \text{(C-86)}$$

Equations C-85 and C-86 indicate that a relative enhancement at high spatial frequency takes place with the toroidal mode pumping. The dc frequency spatial component is decreased and the peak frequency response shifted to higher frequencies.

The above results strongly suggest that spatial filtering can be performed by properly shaping the pump beam. Many techniques developed for

optical data processing and holography can be applied directly to the parametric image upconverter if the pump beam shape is predictable and stable.

The above computational technique can be applied to any TEM_{0n} (n = 0, 1, 2, ...) mode pump beam. It is, however, expected that the mode attenuation factor for circularly asymmetrical modes will not be expressible in a closed form.

For a TEM_{01} mode beam pumped Type I system, the attenuation factor, expressed by equation C-80 of angular spectrum of the upconverted image of an on-axis point object becomes unity since α is identically zero. This implies that the factor sinc ($\Delta K D/2$) will be the dominant factor affecting the resolution of the upconverted image. The resolving power of Type I system is therefore independent of the pump beam mode structure. For a toroidal mode pumped Type I system, the attenuation factor equation C-84 becomes identically equal to zero for an on-axis point object. It implies that on-axis objects would not be upconverted. This is no surprise if one realizes that the on-axis pump power is zero and object waves interact with local pump beam in the Type I system. It is obvious from above observation that the envelope of upconverted image field of Type I system would have the same functional form as that of pump beam.

It is clear from equations C-80 and C-86 that the angular spectrum of upconverted field for Type III system depends heavily on the mode structure of pump beam, since $\alpha > a^2$ for Type III system. The resolution and the

point spread function of Type III system are, therefore, influenced strongly by the pump beam mode structure. It can be shown easily that the point spread function of Type III system pumped with a uniform truncated plane wave (a pill-box pump) follows a $J_1(X)/X$ function. It has also been shown in paragraph 3, that the point spread function of TEM_{oo} mode beam pumped Type III system is a Gaussian function. These examples suggest that the image resolution of Type III system will be degraded by the pump beam divergence.

6. EFFECTS OF CRYSTAL BIREFRINGENCE

In this paragraph we will consider effects of the crystal birefringence upon imaging properties of the upconverter. Negligible aperture diffraction and plane wave pump are assumed in order to isolate the birefringent effect from others.

a. IMAGE SPACE CONFIGURATIONS

Omitting constant amplitude and phase factors, the angular spectrum of upconverted field emanating out of the crystal back surface is

$$\mathcal{E}_s(\kappa, z) \sim \mathcal{E}_i(\kappa, -s) \, \text{Sinc}\left[\frac{D}{2}\left(\frac{\kappa^2 K_p}{2 K_M K_i} + \zeta \kappa_x\right)\right] \cdot \qquad \text{(C-87)}$$

$$e^{i\left[\frac{\zeta D}{2}\kappa_x - \Phi\left(\kappa^2, z\right)\right]}$$

where

$$\Phi(\kappa^2, z) = \frac{\kappa^2}{2}\left(\frac{z - D/Z}{K_{sa}} + \frac{S - D/2}{K_{ia}} + \frac{D}{2K_M} + \frac{D}{2K_s}\right) \tag{C-88}$$

The electric field distribution in the upconverted image field becomes

$$E_s(\underline{\rho}_s, z) \sim \int d\underline{\kappa}\ \mathcal{E}_i(\underline{\kappa}, -s)\ \text{Sinc}\left(\frac{\Delta KD}{2}\right)\ \cdot \tag{C-89}$$

$$e^{-i\left[\Phi(\kappa^2, z) - \kappa_x(x_s - \zeta D/2) + \kappa_y y_s\right]}$$

Equation C-89 indicates that the optimum focusing condition is

$$\Phi(\kappa^2, z) \equiv 0 \quad \text{for all } \kappa$$

The solution, which defines the upconverted image plane,

$$z = -S' = -\frac{K_{sa}}{K_{ia}}\ S - \frac{DK_{sa}}{2}\left[\frac{1}{K_M} + \frac{1}{K_s} - \frac{1}{K_{ia}} - \frac{1}{K_{sa}}\right] \tag{C-90}$$

is identical to the case of negligible birefringence system and defines the image plane.

The line spread function of a line object parallel to the x axis will be considered first. The object field distribution and its angular spectrum are

$$E_i(\underline{\rho}_i, -s) \sim \delta(y - y_{io})$$

$$\tag{C-91}$$

$$\mathcal{E}_i(\underline{\kappa}, -s) \sim e^{-i\kappa_y y_{io}}\ \delta(\kappa_x)$$

The line spread function is then

$$E_s(x_s, y_s, -S') \sim \int \text{Sinc}\left(\frac{DK_p}{4K_M K_i} \, \kappa_y^2\right) e^{+i\kappa_y(y_s - y_{io})} \, d\kappa_y$$

Evaluating the integration, we obtain

$$E_s(x_s, y_s - y_{io}, -S') \sim \frac{4\pi K_M K_i}{K_p D} (y_s - y_{io}) \left[S\left(\sqrt{\frac{2K_M K_i}{\pi K_p D}} (y_s - y_{io})\right)\right.$$

$$\left. -C\left(\sqrt{\frac{2K_M K_i}{\pi K_p D}} (y_s - y_{io})\right)\right] + 4\sqrt{\frac{\pi K_M K_i}{K_p D}} \, \text{Sin}\left[\frac{K_M K_i}{K_p D} (y_s - y_{io})^2 + \frac{\pi}{4}\right]$$

$$(C-92)$$

where Fresnel functions $S(X)$ and $C(y)$ are defined

$$S(X) = \int_0^X \sin\left(\frac{\pi}{2} t^2\right) \, dt$$

$$C(X) = \int_0^X \cos\left(\frac{\pi}{2} t^2\right) \, dt$$

The expression C-92 applies equally to the system with negligible birefringence. This result indicates that the image quality is not degraded along the y direction which is normal to the plane containing optic axis C and the z axis (Figure C-1). The line spread function is only a function of normal distance $(y_s - y_{io})$.

The line spread function of a line object parallel to the y axis is considered next. The object field distribution and its angular spectrum are

$$E_i(\underline{\rho}_i, -S) \sim \delta(x_i - x_{io})$$

$$\smallsmile_{\perp}(\underline{\kappa}, -S) \; e^{-i\,\kappa_x x_{io}}\,\delta(\kappa_y)$$

The line spread function is

$$E_s\left(x_s - x_{io} - \frac{\zeta D}{2}, \; y_s, \; -S'\right) \sim \int d\kappa_x \; \text{Sinc}\left[\frac{D}{2}\left(\frac{\kappa_x{}^2 K_p}{2 K_M K_i} + \zeta \kappa_x\right)\right] \cdot$$

$$e^{i\,\kappa_x \left(x_s - x_{io} - \frac{\zeta D}{2}\right)} \tag{C-93}$$

Rewriting above equation,

$$E_s(x_s' - x_{io}, \; y_s, \; -S') \sim e^{-i\,\frac{\zeta K_M K_i}{2 K_p}\,x'} \int d\kappa \; \text{Sinc}\left\{\frac{K_p D}{4 K_M K_i}\left[\kappa^2\right.\right.$$

$$\left.\left. -\left(\frac{\zeta K_M K_i}{K_p}\right)^2\right]\right\} \cdot e^{i\,\kappa\,(x_s' - x_{io})} \tag{C-94}$$

where

$$x_s' = x_s - \frac{\zeta D}{2}$$

Equation C-94 indicates that crystal birefringence affects the upconverted image in following ways:

- Introducing change in the field distribution from that of non-birefringent case

- The field distribution is a function of $(x_s - x_{io} - \zeta D/2)$ rather than $x_s - x_{io}$. This implies that the x coordinate of upconverted image is translated toward positive x direction by an amount $\zeta D/2$, (Figure C-7). This linear translation becomes obvious if one realizes that energy flow inside the material is along the anisotropy direction rather than along the z direction.

Line spread functions along two orthogonal directions expressed by equation C-92 and equation C-94 are evaluated for a 1.06-μm pumped 1 cm long proustite crystal upconverting 10.6-μm objects into 0.967-μm images. The results are plotted in Figure C-8. The amplitude of the spread functions is normalized to the peak amplitude of the line spread function parallel to the x axis.

Resolvable image line width along the y direction can be determined by Rayleigh criterion since the sidelobes of the spread function parallel to the x axis are considerably lower compared to the mainlobe.

The spread function parallel to the y axis contains several nearly equal amplitude lobes as seen in Figure C-8. The amplitude of these lobes is considerably lower than that of the mainlobe of the x direction line spread function. The width of these lobes is also narrower than that of the x direction line spread function. Rayleigh resolution criterion cannot be used to determine resolution along the x direction, because the adjacent lobes are nearly equal in amplitude.
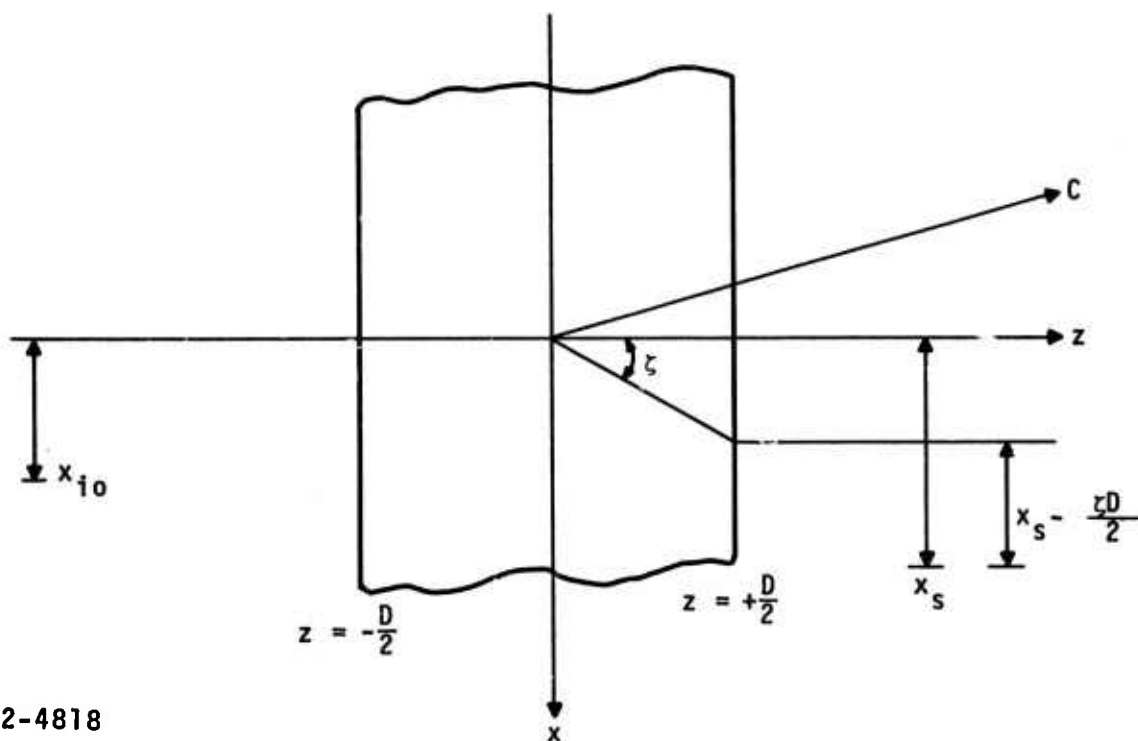
2-4818

FIGURE C-7. GEOMETRIC RELATIONSHIP BETWEEN X CO-
ORDINATE OF IR OBJECT FIELD AND X CO-
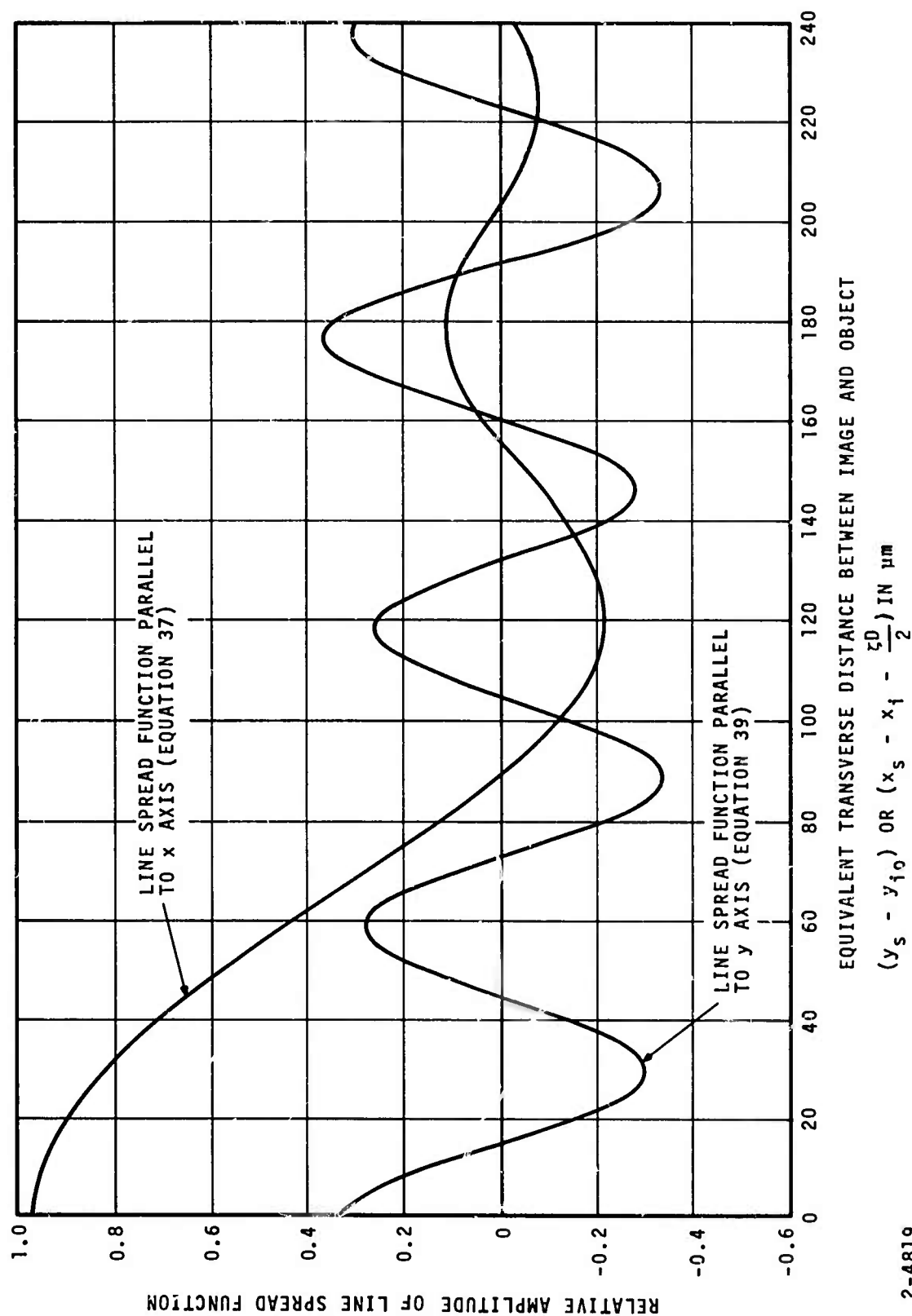ORDINATE OF UPCONVERTED IMAGE FIELD

FIGURE C-8. RELATIVE AMPLITUDE OF LINE SPREAD FUNCTIONS
FOR 1 cm LONG PROUSTITE

2-4819

Resolution degradation along the x axis predicted from Figure C-8 has not been observed in the experiments described in Appendix A. One of possible causes for not observing resolution degradation is due to the masking of birefringent effect by relatively larger diffraction line width of the object lens.

More careful measurements of line spread function parallel to the y axis are necessary in order to observe the effect of crystal birefringence.

b.   FOURIER SPACE CONFIGURATION

It has been shown in paragraph A that the field distribution of upconverted image formed in the back focal plane of lens L_2 (Figure C-4) is related to the object field distribution over the front focal plane of lens L_1 by repeating equations C-41, C-42, and C-43

$$E_s \, (\underline{\rho}_s) \sim E_i \left(\frac{-K_{sa} \, f_1}{K_{ia} \, f_2} \; \underline{\rho}_s \right) \quad \mathrm{Sinc} \; \left(\frac{\Delta \, KD}{2} \right) \; e^{-i \left(\frac{\Delta KD}{2} - K_{sz} D \right)} \quad \text{(C-95)}$$

where ΔK and K_{sz} are given by equations C-42 and C-43

$$\Delta K = - \frac{K_p}{2 K_M K_i} \left(\frac{K_{sa}}{f_2} \; \underline{\rho}_s \right)^2 - \zeta \, \frac{K_{sa}}{f_2} \, x_s \quad \text{(C-96)}$$

$$K_{sz} = K_s^2 - \left(\frac{K_{sa}}{f_2} \; \rho_s \right)^2 \quad \text{(C-97)}$$

From previous equations we can conclude:

- Magnification along two orthogonal transverse directions is not affected by the crystal birefringence. This implies no distortion.

- Different amplitude envelope along two orthogonal transverse axes. This implies different acceptance angle for two directions. Acceptance angle in the yz plane is given by equation C-48. In the xz plane it becomes:

$$\theta_{iax} = 2 \frac{\lambda_p n_s}{\lambda_s n_p} \left[\left(\zeta^2 + \frac{2n_p \lambda_s \lambda_i}{\lambda_p n_x n_i} \right)^{1/2} - \zeta \right] \tag{C-98}$$

- No degradation in resolving power, since the factor $\text{Sinc}\left(\frac{\Delta KD}{2}\right)$ in equation C-41 only affects the envelope of image.

APPENDIX D

MATERIAL DAMAGE AND LIGHT ABSORPTION
OF PROUSTITE AT 1.06 μm

1.   MATERIAL DAMAGE

The question of material damage is central to the design and operation of a parametric upconversion system; the reason being the large pump radiation power densities to which the nonlinear materials are subjected for attaining high conversion efficiency.

Damage thresholds of the proustite crystal under different conditions have been reported by many authors. Fountain et al[22] reported on damage thresholds of proustite at 1.06 μm subjected both the CW irradiation and a Q-switched laser pulse. They ascribed damage in proustite to local heating caused by absorption. Hanna et al[23] also published their results of Q-switched laser damage of proustite crystals at 1.06 μm, 10.6 μm, and 694 nm. The damage thresholds of Q-switched laser irradiation at 1.06 μm reported by Fountain and Hanna are comparable. Hanna, however, excluded surface melting due to absorption as a probable damage mechanism. Lucy[24] has also reported damage threshold of proustite with a pulsed Ruby laser. He observed significant damage at peak power densities of 10 kW/cm^2 with 1-ms pulse. This level is three orders of magnitude below those reported by Hanna with a Q-switched Ruby laser. Accumulation of damage is apparent from these data.

The three cited references have not reached a clear correlation between damage thresholds and bulk-absorption coefficients. They disagreed on a probable damage mechanism.

At AIL the upconversion system has been operated by pumping the proustite crystal with CW Nd:YAG laser radiation. An accumulation of white powder on the exit surface of proustite crystal has been noticed. This may be attributed to radiation enhanced surface oxidation[23,25]. The area and shape of powder accumulation matches the 1.06-μm beam cross section. The powder accumulation is noticeable after a few tens of minutes of continuous irradiation at approximately 1 W/cm^2. Warner[26] indicated the same phenomenon with a continuous 694-nm irradiation of proustite. He reported that the surface oxidation becomes visible after several minutes of 694-nm irradiation at approximately 1 W/cm^2.

In an attempt to obtain more information on the surface oxidation of proustite, an experiment was performed by placing a proustite in an evacuated vessel. The vessel was evacuated to approximately one Torr pressure and the crystal was irradiated with a chopped 1.06-μm beam of 80-percent duty factor. The average power density of 1.06-μm beam was approximately 3 W/cm^2 with a temporal peak power density of 37.5 W/cm^2. Surface oxidation was not observed even after 1/2 hour of irradiation. This level of exposure is considerably higher than the level proustite would tolerate in the atmosphere. The result indicates that Q-switched laser damage threshold of proustite might be improved if the proustite is operated in a vacuum or in an inert gas atmosphere.

2. LIGHT ABSORPTION OF PROUSTITE AT 1.06 μm

The correlation between damage thresholds and bulk light absorption is not clearly understood. There are, however, data that indicate that the damage thresholds and surface oxidation levels of proustite are lower at 694 nm than at 1.06 μm. Lower damage threshold at 694 nm may be attributed to higher light absorption. Therefore, it has been found to be worthwhile to obtain the light absorption coefficient of proustite at 1.06 μm, since bulk absorption of proustite at 1.06 μm has never been reported in literature.

A calorimetric measurement was done of the absorption coefficients of a proustite crystal prepared for upconversion of 10.6-μm infrared radiation to 967 nm.* The crystal is oriented such that the optic axis (C-axis) makes a 20-degree angle with the normal of the (polished) front surface. The crystallographic X-axis is parallel to the front surface. A linearly polarized chopped 1.06-μm beam from a CW TEM_{oo} mode Nd:YAG laser was incident normally on the crystal front surface. The average power densities at the center of 1.06-μm beam were approximately 5 W/cm^2. The duty factor of light chopper is 8.5 percent and the repetition period is short enough to neglect the thermal time constant of the material.

---

* Measurements were performed with an absorption meter at Holobeam Inc. Paramus, N. J.

The average power level incident on the crystal, the average power transmitted through the material, and the average power absorbed by the crystal were measured. The proustite was mounted on a Peltier cooler. Electric current through the Peltier cooler was adjusted until an equilibrium was reached between the heat generated by the crystal light absorption and the cooling rate of the Peltier cooler. The amount of light power absorbed by a material is, thus, measured by observing the cooling current of the calibrated Peltier cooler.

Absorptions of the ordinary wave, which is polarized normal to the crystal C-axis, and of the extraordinary wave, which is polarized parallel to the C-axis, were measured. Reflection losses at the surfaces were calculated from the Fresnel reflection formula since the index of refraction of proustite is accurately known. Table D-1 lists the measured power levels and the percentage power level referred to the input power.

TABLE D-1. TRANSMISSION AND ABSORPTION OF A 0.95-cm LONG PROUSTITE* AT 1.06 μm

	Incident Average Power		Transmitted Power		Absorbed Power		Calculated Reflection Loss
	mW	percent	mW	percent	mW	percent	percent
Ordinary Wave	153.5	100	77.4	50.5	11.1	7.24	40.2
Extraordinary Wave	160	100	82.6	51.6	9.6	6.0	38.2

* Proustite is prepared for Type II upconversion of 10.6 μm with the 1.06-μm pump.

As evident from Table D-1, 2 percent of incident power for the ordinary wave case and 4 percent for the extraordinary wave case are unaccounted for. While it is possible that this missing power is due to the measurement error, it was felt that the scattering inside the crystal is responsible for the bulk of these losses. The accuracy of the power absorption measurement is, according to J. Muray of Holobeam, within ±5 percent of actual.

The absorption coefficient of the material was computed by the following equation:

$$P_{ab} = P_o (1 - e^{-\alpha \ell}) \qquad (21)$$

where

P_{ab} = absorbed power

P_o = power input to the material, excluding the front surface reflection loss

α = absorption coefficient

ℓ = material length in cm.

The absorption coefficient for the ordinary wave was found to be 0.104 cm^{-1} and that for the extraordinary wave is 0.082 cm^{-1}. The measured absorption coefficients at 1.06 μm are one order of magnitude less than that reported at 694 nm[3].

During the absorption measurement, a slight reversible temperature dependent absorption was noted. Quantitative measurements of

the temperature dependence were not performed because of limitations in the instrument.

Light absorption of proustite at 1.06 μm is slightly less than the 0.45 cm^{-1} for pyrargyrite[27] and is considerably better than that of $ZnGeP_2$[28], selinium, and $CdGeAs_2$[29].
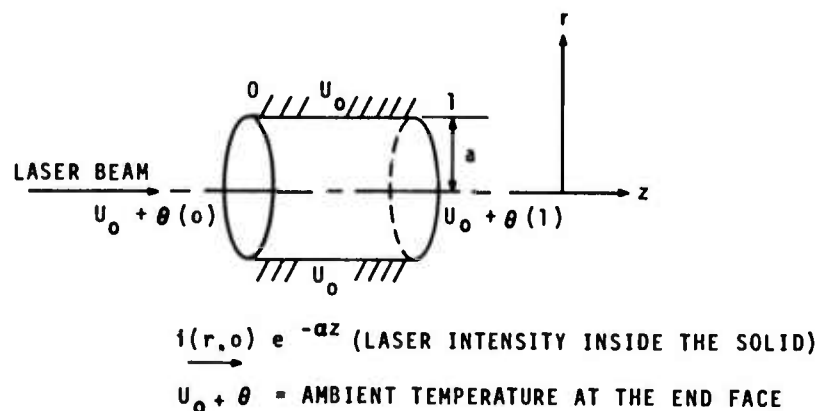
The temperature dependence of the light absorption and the thermal properties of the proustite should be measured to provide a better understanding of damage mechanism. It is also recommended that a more extensive and more thorough investigation of the laser damage of proustite be done under controlled conditions.

APPENDIX E

ANALYSIS OF HEAT CONDUCTION IN LIGHT ABSORBING SOLIDS

The problem of heat conduction in a light absorbing uniform isotropic solid is considered. A nonlinear material such as proustite used for nonlinear optics application is generally in a single crystal form. Thermal transportation in the single crystal is not isotropic, but the tensor properties of thermal conductivity will be neglected in this analysis to simplify the problem. It is also assumed that light absorption and propagation are isotropic in the analysis.

Figure E-1 shows schematically the problem considered. The material is cylindrical with its side firmly in contact with a heat sink. The laser beam travels along the cylindrical axis.

$i(r,o)\, e^{-\alpha z}$ (LASER INTENSITY INSIDE THE SOLID)

$U_0 + \theta$ = AMBIENT TEMPERATURE AT THE END FACE

3-1155

FIGURE E-1. HEAT CONDUCTION GEOMETRY

The differential equation describes heat conduction as:

$$k\nabla^2 u(\underline{r}, z, t) + s(\underline{r}, z, t) = c\rho \frac{\partial u(\underline{r}, z, t)}{\partial t} \qquad (E\text{-}1)$$

where:

k = thermal conductivity

$u(\underline{r}, z, t)$ = temperature at the point $(\underline{r}, z)$ and at time t

$s(\underline{r}, z, t)$ = heat source within the medium

c = specific heat

ρ = density

$\underline{r}$ = transverse coordinate

z = axial coordinate

The boundary conditions are expressed by

$$u(a, z, t) = U_o \qquad (E\text{-}2)$$

$$\left.\frac{\partial u}{\partial z}\right|_{z=o} = \frac{h}{k}\left[u(\underline{r}, o, t) - \theta(\underline{r}, o, t) - U_o\right] \qquad (E\text{-}3)$$

$$-\left.\frac{\partial u}{\partial z}\right|_{z=\ell} = \frac{h}{k}\left[u(\underline{r}, \ell, t) - \theta(\underline{r}, \ell, t) - U_o\right] \qquad (E\text{-}3)$$

where:

ℓ = axial length of the solid

a = radius of the cylindrical solid

U_o = temperature of heat sink

h = coefficient of heat exchange

$\theta + U_o$ = temperature of medium just outside of the end faces

The boundary condition expressed by equation E-2 indicates heat sinking at the side wall. Equations E-3 and E-4 indicate heat exchange at the end faces with the surrounding medium.

The source term in equation E-1 is given, for an axially propagating light,

$$s\ (\underline{r}, z, t) = i_o\ (\underline{r}, o, t)\ \alpha\ e^{-\alpha z} \qquad (E-5)$$

where:

$i_o\ (r, o, t)$ = light intensity at the input end-face

α = light absorption coefficient

A solution to equation E-1 subjected to the boundary condition equations E-2, E-3, and E-4 can be separated into two terms:

$$u\ (\underline{r}, z, t) = v\ (\underline{r}, z, t) + U_o \qquad (E-6)$$

The equation and the boundary conditions for v then become:

$$k \nabla^2 v + s = c \rho \frac{\partial v}{\partial t} \qquad \text{(E-7)}$$

$$v(a, z, t) = o \qquad \text{(E-8)}$$

$$\frac{\partial v}{\partial z}\bigg|_{z=o} = \frac{h}{k} \left[v(\underline{r}, o, t) - \theta(\underline{r}, o, t) \right] \qquad \text{(E-9)}$$

$$-\frac{\partial v}{\partial z}\bigg|_{z=\ell} = \frac{h}{k} \left[v(\underline{r}, \ell, t) - \theta(\underline{r}, \ell, t) \right] \qquad \text{(E-10)}$$

If one expresses v and s in temporal Fourier integrals:

$$v(\underline{r}, z, t) = \int V(\underline{r}, z, f) e^{-i2\pi f t} \; df \qquad \text{(E-11)}$$

$$s(\underline{r}, z, t) = \int S(\underline{r}, z, f) e^{-i2\pi f t} \; df \qquad \text{(E-12)}$$

The differential equation for Fourier component V becomes:

$$k \nabla^2 V + S = -i2\pi f c \rho V \qquad \text{(E-13)}$$

The boundary condition for V becomes:

$$V(a, z) = O \qquad \text{(E-14)}$$

$$\frac{\partial V}{\partial z}\bigg|_{z=o} = \frac{h}{k} \left[V(\underline{r}, o) - T(\underline{r}, o) \right] \qquad \text{(E-15)}$$

$$\frac{\partial V}{\partial z}\bigg|_{z=0} = -\frac{h}{k}\left[V(\underline{r}, t) - T(\underline{r}, t)\right] \qquad (E-16)$$

where:

$$T(\underline{r}, z, f) = \int \Theta(\underline{r}, z, t)\, e^{i2\pi ft}\, dt \qquad (E-17)$$

The frequency dependence of V, S, and T in equations E-13 through E-16 is not expressed explicitly to shorten the notation. The Fourier source component is expressed by

$$S(\underline{r}, z, f) = \alpha\, e^{-\alpha z}\, I_0(\underline{r}, o, f) \qquad (E-18)$$

where:

$$I_0(\underline{r}, o, f) = \int i_0(\underline{r}, o, t)\, e^{-i2\pi ft}\, dt \qquad (E-19)$$

We assume a solution

$$V(r, z) = \sum_{n=1}^{\infty} R_n(r)\, Z_n(z) \qquad (E-20)$$

where $R_n(r)$ is an eigenfunction of homogeneous differential equation

$$\frac{1}{r}\frac{d}{dr}\left(r\frac{dR_n}{dr}\right) + \lambda_n^2 R_n = 0 \qquad (E-21)$$

Eigenvalues λ_n are determined by the boundary condition

$$R_n (a) = O$$

The solution R_n is then

$$R_n (r) = J_0 (\gamma_n r/a) \tag{E-22}$$

where γ_n is the nth root of the zeroth order Bessel function $J_0 (x)$. The source function S can be expanded in terms of eigenfunctions R_n

$$S (r, z, f) = \alpha e^{-\alpha z} \sum_{n=1}^{\infty} H_n (f) R_n (r) \tag{E-23}$$

where

$$H_n (f) = \frac{\int_0^a I_0 (r, o, f) R_n (r) \, rdr}{\int_0^a R_n^2 (r) \, rdr}$$

The differential equation for $Z_n (z)$ is obtained by substituting equations E-20 and E-23 into equation E-13,

$$\frac{d^2 Z_n}{dz} + \left(i2\pi f c \rho/k - \lambda_n^2 \right) Z_n = -H_n \alpha e^{-\alpha z} \tag{E-24}$$

The boundary conditions for Z_n (z) are

$$\left. \frac{d Z_n}{dz} \right|_{z=0} = \frac{h}{k} \left[Z_n \text{ (o)} - T_n \text{ (o)} \right] \qquad \text{(E-25)}$$

$$- \left. \frac{d Z_n}{dz} \right|_{z=\ell} = \frac{h}{k} \left[Z_n \text{ (}\ell\text{)} - T_n \text{ (}\ell\text{)} \right] \qquad \text{(E-26)}$$

where

$$T \text{ (r, z)}|_{z=o,\ell} = \sum T_n \text{ (z)}|_{z=o,\ell} R_n \text{ (r)} \qquad \text{(E-27)}$$

$$T_n \text{ (z)}|_{z=o,\ell} = \left. \frac{\int_o^a T \text{ (r, z)} R_n \text{ (r) rdr}}{\int_o^a R_n^2 \text{ (r) rdr}} \right|_{z=o,\ell}$$

The solution Z_n (z) of differential equation E-24 can be written as

$$Z_n \text{ (z)} = \Psi_n \text{ (z)} \cdot e^{-\alpha z} \qquad \text{(E-28)}$$

Substituting equation E-28 into equation E-24, we obtain the differential equation for Ψ_n (z)

$$\frac{d^2 \Psi_n}{dz^2} - \alpha \frac{d \Psi_n}{dz} + (\alpha^2 - \gamma_n^2/a^2 + ip) \Psi_n = -H_n \alpha \qquad \text{(E-29)}$$

E-7

where

$$p = 2\pi fc\rho/k$$

The boundary conditions for $\Psi_n(z)$ now becomes

$$\frac{d\Psi_n}{dz}\bigg|_{z=o} = \left(\frac{h}{k} + \alpha\right) \Psi_n(o) - \frac{h}{k} T_n(o) \qquad (E-30)$$

$$\frac{d\Psi_n}{dz}\bigg|_{z=\ell} = \left(\alpha - e^{\alpha\ell}\frac{h}{k}\right) \Psi_n(\ell) + \frac{h}{k} e^{\alpha\ell} T_n(\ell) \qquad (E-31)$$

The solution of equation E-29 is

$$\Psi_n(z) = \frac{-H_n\alpha}{\alpha^2 - \gamma_n^2/a^2 + ip} + A_n e^{q_{n1}z} + B_n e^{q_{n2}z} \qquad (E-32)$$

where

$$q_{n1} = \frac{\alpha}{2} + \frac{1}{2}(4\gamma_n^2/a^2 - 3\alpha^2 - i4p)^{1/2} \qquad (E-33)$$

$$q_{n2} = \frac{\alpha}{2} - \frac{1}{2}(4\gamma_n^2/a^2 - 3\alpha^2 - i4p)^{1/2} \qquad (E-34)$$

Linear simultaneous equations for A_n and B_n, which obtained by substituting equation E-32 into equations E-30 and E-31, are

$$A_n \left(q_{n1} - \alpha - \frac{h}{k} \right) + B_n \left(q_{n2} - \alpha - \frac{h}{k} \right) = \frac{-H_n \alpha \left(\alpha + \frac{h}{k} \right)}{\alpha^2 - \gamma_n^2 / a^2 + ip} - \frac{h}{k} T_n (o) \qquad \text{(E-35)}$$

$$A_n \left(q_{n1} e^{q_{n1} \ell} - \alpha + \frac{h}{k} e^{\alpha \ell} \right) + B_n \left(q_{n2} e^{q_{n2} \ell} - \alpha + \frac{h}{k} e^{\alpha \ell} \right) = \qquad \text{(E-36)}$$

$$\frac{-H_n \alpha \left(\alpha - e^{\alpha \ell} \frac{h}{k} \right)}{\alpha^2 - \gamma_n^2 / a^2 + ip} + \frac{h}{k} e^{\alpha \ell} T_n (\ell)$$

It must be remembered that the function $\Psi_n (z)$ is a function of the temporal frequency f, since the quantities p, H_n, T_n (o) and $H_n (\ell)$ are all functions of frequency.

Solving equation E-35 and E-36 for A_n and B_n, we obtain

$$A_n = \frac{-\left(q_{n2} e^{q_{n2} \ell} - \alpha + \frac{h}{k} e^{\alpha \ell} \right) \left[\frac{H_n \alpha \left(\alpha - \frac{h}{k} \right)}{\alpha^2 - \gamma_n^2/a^2 + ip} - \frac{h}{k} T_n (o) \right] - \left(q_{n2} - \alpha - \frac{h}{k} \right) \left[\frac{H_n \alpha \left(\alpha - e^{\alpha \ell} \frac{h}{k} \right)}{\alpha^2 - \gamma_n^2/a^2 + ip} - \frac{h}{k} e^{\alpha \ell} T_n (\ell) \right]}{\Delta} \qquad \text{(E-37)}$$

$$B_n = \frac{-\left(q_{n1} - \alpha - \frac{h}{k}\right)\left[\frac{H_n \alpha \left(\alpha - e^{\alpha \ell} \frac{h}{k}\right)}{\alpha^2 - \gamma_n^2/a^2 + ip} + \frac{h}{k}e^{\alpha \ell}T_n(\ell)\right] + \left(q_{n1}e^{q_{n1}\ell} - \alpha + \frac{h}{k}e^{\alpha \ell}\right)\left[\frac{H_n \alpha \left(\alpha - \frac{h}{k}\right)}{\alpha^2 - \gamma_n^2/a^2 + ip} + \frac{h}{k}T_n(o)\right]}{\Delta} \quad \text{(E-38)}$$

where

$$\Delta = \left(q_{n1} - \alpha - \frac{h}{k}\right)\left(q_{n2}e^{q_{n2}\ell} - \alpha + \frac{h}{k}e^{\alpha \ell}\right) - \left(q_{n2} - \alpha - \frac{h}{k}\right)\left(q_{n1}e^{q_{n1}\ell} - \alpha + \frac{h}{k}e^{\alpha \ell}\right) \quad \text{(E-39)}$$

This completes formal solution of heat condition in light absorbing solid cylinder.

REFERENCES

1. J. Midwinter and J. Warner, "Journal of Applied Physics," Vol 38, p 519, 1967.

2. R. F. Lucy, "Applied Optics," Vol 11, p 1329, 1972.

3. D. C. Hanna, "Optics Communication," Vol 4, p 300, 1971.

4. K. F. Hulme, "Applied Physics Letters," Vol 10, p 133, 1967.

5. G. Boyd, "Applied Physics Letters," Vol 5, p 234, 1964.

6. R. Miller and E. Savage, "Applied Physics Letters," Vol 9, p 169, 1966.

7. J. Bjorkholm, "Journal of Quantum Electronics," Proc IEEE, Vol QE-4, p 970, 1968.

8. J. Bjorkholm, "Journal of Quantum Electronics," Proc IEEE, Vol QE-5, p 260, 1969.

9. R. Byer, "Physical Review," Vol 168, p 1064, 1968.

10. J. Jerphagnon and S. Kurtz, "Physical Review B," Vol 1, p 1739, 1970.

11. G. E. Francois, "Physical Review," Vol 143, p 597, 1966.

12. Boggett, "Applied Physics Letters," Vol 28A, p 33, 1968.

13. A. H. Firester, "Image Upconversion, Part III," Journal Applied Physics, Vol 41, p 703, 1970.

14. J. Goodman, "Introduction to Fourier Optics," McGraw-Hill, 1968.

15. D. Kleinman, "Theory of Second Harmonic Generation of Light," Phys Rev, Vol 128, p 1761, 1962.

16. G. Boyd, A. Ashkin, J. Dziedzic, and D. Kleinman, "Second Harmonic Generation of Light with Double Refraction," Phys Rev, Vol 137, p A1305.

17. E. Midwinter and J. Warner, "Upconversion of Near Infrared to Visible Radiation in $LiNbO_3$," Journal Applied Physics, Vol 38, p 519, 1967.

18. J. Armstrong, N. Bloembergen, J. Ducuing, and P. Pershen, "Interaction Between Light Waves in a Nonlinear Dielectric," Phys Rev, Vol 127, p 1918, 1962.

19. A. Yariv, "Quantum Electronics," Wiley & Sons, 1967.

20. N. Bloembergen and P. Pershan, "Light Waves at the Boundary of Nonlinear Media," Phys Rev, Vol 218, p 606, 1962.

21. Born and Wolf, "Principles of Optics," Second Ed. Press.

22. W. Fountain, L. Osterink, and G. Massey, "Optically Induced Physical Damage to $LiNbO_3$, Proustite and $LiIO_3$," Proc Conf, Damage in Laser Materials, Boulder, Colorado, May 1971.

23. D. Hanna, B. Davies, H. Rutt, R. Smith, and C. Stanley, "Q-Switched Laser Damage of Infrared Nonlinear Materials," IEEE Jour of QE, QE-8, p 317, 1972.

24. R. Lucy, "Laser Parametric Image Upconversion," Tech Rep AFAL-TR-72-23, Itek Corporation, January 1972.

25. P. H. Pough, "A Field Guide to Rocks and Minerals," London, Constable, 1970.

26. J. Warner, Private Communication.

27. J. Feichtner, R. Johannes, and G. Roland, "Growth and Optical Properties of Single Crystal Pyrargyrite (Ag_3SbS_3)," Appl Optics, Vol 9, p 1716, 1970.

28. G. Boyd, W. Gandrud, and E. Buehler, "Phase-Matched Upconversion of 10.6 μm Radiation in $ZnGeP_2$," Appl Phys Letters, Vol 18, p 446, 15 May 1971.

29. R. Byer, H. Kildal, and R. S. Feigelson, "$CdGeAs_2$: A New Nonlinear Crystal Phasematchable at 10.6 μm," Appl Phys Letters, Vol 19, p 237, 1 October 1971.